Induction of Interfacial Gradients to Generate Drop Motion and Internal Flows

喜多, 由拓

Induction of Interfacial Gradients to Generate Drop Motion and Internal Flows

Yutaku Kita

Thesis submitted for the degree of

Doctor of Engineering

at

Kyushu University

九州大学

KYUSHU UNIVERSITY

Acknowledgement

I would like to express my gratitude to all who have supported me and my study from across the globe. Firstly, I am deeply grateful to my supervisor, Prof Yasuyuki Takata, for his guidance, patience and for providing me with more opportunities than I could have ever whished for. It has been a pleasant time when he takes me for walking around campus, which indeed has helped me refresh and made the day more meaningful.

I would also like to appreciate the Dissertation Committee Members, Prof Khellil Sefiane, Prof Koji Takahashi and Prof Masamichi Kohno for agreeing to participate in the review process and making many suggestions and comments.

I would like to send my sincere thanks to Prof Khellil Sefiane from the University of Edinburgh for enlightening and fruitful collaborations both in Japan and in the UK. The invaluable opportunity provided by him to work at the Institute of Multiscale Thermofluids of UoE gave me rich academic experiences and the enjoyable time with friends I met in Scotland. During my stay in Edinburgh, Dr Prashant Valluri and Dr Coinneach Mackenzie-Dover had helped me a lot with my experiments and living. I also deeply appreciate their kindness.

Equally, my special gratitude goes to Prof Jungho Kim from the University of Maryland, College Park for his generous welcome to the Phase Change Heat Transfer Laboratory of UMD. My first long-term stay abroad has changed me drastically in terms of an attitude to research, engineering and to failure, and of cultural perspectives. The parabolic flight—*Vomit Comet*—for the experiment with him and his student, Caleb, under microgravity has been an unforgettable experience. I could not thank enough for what he had provided me during my stay in the United States.

I would like to thank Prof Masamichi Kohno and Dr Naoya Sakoda for their

helpful advice in the lab meeting. I also sincerely appreciate Dr Sumitomo Hidaka and Ms Mitsuko Shuto for their kind support.

It can never go without expressing my true thanks to Dr Alexandros Askounis who have been always supportive, patient and respectful. My PhD project would not have been successful without his encouragement. I really thank you.

I'm also grateful to Dr Daniel Orejon who first demonstrated how to operate the experimental equipment, with patience, despite my poor English at that time. I truly appreciate for his continuous help since I join the lab as a master student. Special gratitude must also go to Dr Harish Sivasankaran, Dr Biao Shen and Dr Taichi Kuroki for their contribution to the lab activities.

Among my colleagues in the Thermofluid Physics Laboratory at Kyushu University, I should mention Dr Yuki Fukatani, Dr Masayuki Yamada, Mr Yuya Okauchi, Ms Zhenying Wang and Mr Huacheng Zhang who were closely working together. It has been my greatest pleasure being part of this group of exceptional individuals and of Kyushu University.

I acknowledge the Japan Society for the Promotion of Science, Japan Public-Private Partnership Student Study Abroad Program (TOBITATE! Young Ambassador Program) by MEXT, and the International Institute for Carbon-Neutral Energy Research (WPI-I^{2}CNER) for their financial support through my doctoral course and research.

To conclude, I send my deepest gratitude to my parents, Kakutoshi and Rika, and my little sister, Nanase for their unconditional support and for believing in my decision toward my academic journey.

Due to the limited space, I apologise for not being able to mention all the people who have actually supported me. I wish to express my sincere gratitude by dedicating this work to abovementioned advisors, colleagues, all my friends and family.

22nd August, 2018—Yutaku Kita

Abstract

This thesis is devoted to experimentally elucidating the dynamics of liquid drops on gradients at the interfaces *i.e*. temperature and wettability gradients. A drop driven away from the equilibrium state will be "active" and will act in order to attain the energetically favourable state, inducing flows or drop motion. Actions that drops make in such situation are not merely of fundamental scientific interest but also exploring ways to activate or control a system containing drops has progressively become of importance in industrial and biomedical applications. The present study deals with drops of pure water, which is ubiquitous but unique, and investigates their thermocapillary-driven instabilities induced by localised heating and mobility on wettability gradients imposed via superhydrophobic microstructure patterning.

The First problem addressed in the thesis is the existence of thermocapillary "Marangoni" flows in pure water which has been a long-standing controversial issue due to an ambiguity between theoretical predictions and little experimental evidence. The thesis reports the very first observation/visualisation of Marangoni-driven counter-rotating vortices in a pure water drop using infrared thermography coupled with optical particle imaging. The flows are induced by imposing a thermal gradient along the drop surface by locally heating the substrate directly underneath the centre with a laser. The origin of the flows is identified by comparing the dimensionless Marangoni and Rayleigh numbers, which shows the dominance of thermocapillary convection over buoyancy. This is further corroborated by a second set of experiments with an inverted system where the same flow patterns are observed regardless of the gravity orientation.

Secondly, as a systematic analysis, the effect of heating power and location on Marangoni flows as well as evaporation of water drops is studied. Heating

location is found to have a major impact on the flow patterns as recirculating vortices travel azimuthally within the drop when heating the centre whereas the flow direction remains fixed during edge heating. Further analysis of thermographic data allows to calculate the flow velocity which appears to increase for higher heating power as well as for the edge-heating case. Moreover, evaporation kinetics such as the rate of vaporisation and triple-line motion is found to be subject to the effect of local heating.

In addition to internal flows induced by thermal gradients, the last part of the thesis focuses on mobility of millimetre-sized water drops propelled by wettability contrasts/gradients. To this end, micropillar fabrication on hydrophobic surfaces is used in the present work to engineer wettability gradients by virtue of their wettability controllability and resultant superhydrophobic characteristic. A millimetre-sized water drop, placed at the boundary between two surfaces with different pillar densities, spontaneously moves toward the surface with more densely populated asperities, which is relatively more hydrophilic. Drop motion is found to accelerate proportionally with the difference in pillar densities on each surface, provided that the rear-side surface has sufficiently small pinning effect or contact angle hysteresis. Furthermore, an analysis of surface free energy is implemented to rationalise the drop motion. Coupling the energy analysis with the experimental observations reveals that motion is initiated by the excess surface energy due to drop deformation and is directed in favour of energy minimisation. Lastly, a thermodynamic mechanism to predict the direction of the drop which at the same time suggests the criterion for the motion to ensue is proposed.

Contents

Nomenclature

Physical properties

D_{AB}	Diffusion coefficient	$m^2\ s^{-1}$
g	Acceleration due to gravity	$m\ s^{-2}$
M	Molecular weight	$kg\ mol^{-1}$
α	Thermal diffusivity	$m^2\ s^{-1}$
β	Coefficient of thermal expansion	K^{-1}
μ	Dynamic viscosity	Pa·s
ν	Kinematic viscosity	$m^2\ s^{-1}$
ρ	Density	$kg\ m^{-3}$
σ	Interfacial/surface tension	$N\ m^{-1}$

Other variables

a_i	Polynomial coefficient in Eq. (1.5)	
A	Area	m^2
c	Vapour concentration	$kg\ m^{-3}$
f_{Ma}	Characteristic Marangoni frequency	Hz
f_p	Pinning force per unit length	$N\ m^{-1}$
G	Surface free energy	J
H	Characteristic vertical length/height	m
m	Mass	kg
P	Pressure	Pa
r	Roughness factor	-
R	Characteristic radial length/radius	m
t	Time	s
T	Temperature	°C
ΔT	Temperature difference	K

v	Drop velocity	m s^{-1}
v_{Ma}	Characteristic Marangoni velocity	m s^{-1}
V	Volume	m^3
x, y	Cartesian coordinates	m
δ	Normalised maximum three-phase contact line	-
η	Decay constant	s^{-1}
θ	Contact angle	degree or radian
λ_{AB}	Characteristic Lennard-Jones length	Å
λ_c	Capillary length	m
τ_{Ma}	Marangoni time scale	s
ϕ	Surface area fraction	-
$\Delta\phi$	Differential surface area fraction	-
Ω_D	Diffusion collision integral	-

Subscripts & Superscripts

∞	Surroundings
A, *B*	Gas A and gas B (Chapter 2), or surface A, surface B (Chapter 3)
adv	Advancing
app	Apparent
base	Drop base
c	Critical
CAH	Contact angle hysteresis
cap	Drop cap
E	Equilibrium
ini	Initial state
LV	Liquid-vapour interface
max	Maximum
meta	Metastable state
min	Minimum

rec	Receding
s	Saturated condition
SL	Solid-liquid interface
SV	Solid-vapour interface

Dimensionless numbers

Bo	(Static) Bond number	$Bo = \frac{\Delta \rho g R^2}{\sigma_{LV}}$
Bd	Dynamic Bond number	$Bd = \frac{Ra}{Ma}$
Ma	Marangoni number	$Ma = -\frac{\partial \sigma_{LV}}{\partial T} \frac{H^2 \Delta T}{\rho \nu \alpha R}$
Ra	Rayleigh number	$Ra = \frac{\beta g H^4 \Delta T}{\nu \alpha R}$

Chapter 1

Introduction

1.1 Background

Liquid drops or droplets are omnipresent in nature and have inevitably caught people's eye in the sweep of history as found in classic Japanese poems (*waka*) compiled in "*Man'yoshu*" in the eighth century. In the poems, the unidentified poet clearly observed raindrops rolling on a lotus leaf (Figure 1.1 (a)), which is under intensive research today, interestingly. Technically, a drop may be defined as a small (millimetric or smaller) column of liquid which is bounded by interfaces with other fluids or solids. In most situations, liquids come into contact with solid surfaces—sessile drops such as raindrops on an umbrella or window, spilled coffee on a desk and dew drops on a glass of cold drink, to name but a few (Figure 1.1 (b)–(d)). Besides the presence in nature, phase change and wetting of drops/droplets are also fundamental processes in practical applications *e.g.* inkjet printing, spray cooling and pesticide application in agricultural fields (Figure 1.1 (e)–(g)). Thanks not only to the ubiquity but also to the importance in industrial and life processes, enormous scientific interest has been attracted to understanding the physics involved in sessile drops for centuries.

"*A fluid of droplet on a solid surface is ostensibly so simple a physical system that one might suppose that all its behavior is thoroughly understood*."—Robert D. Deegan [1]. It is amazing to see, however, how complex a system where a small cluster of molecules sits on a solid surface can be: interaction between liquid and solid phases (wetting), internal/external flows, heat and mass transfer (phase change), vapour conditions and surface tension interplay at the macro-, micro- and meso-

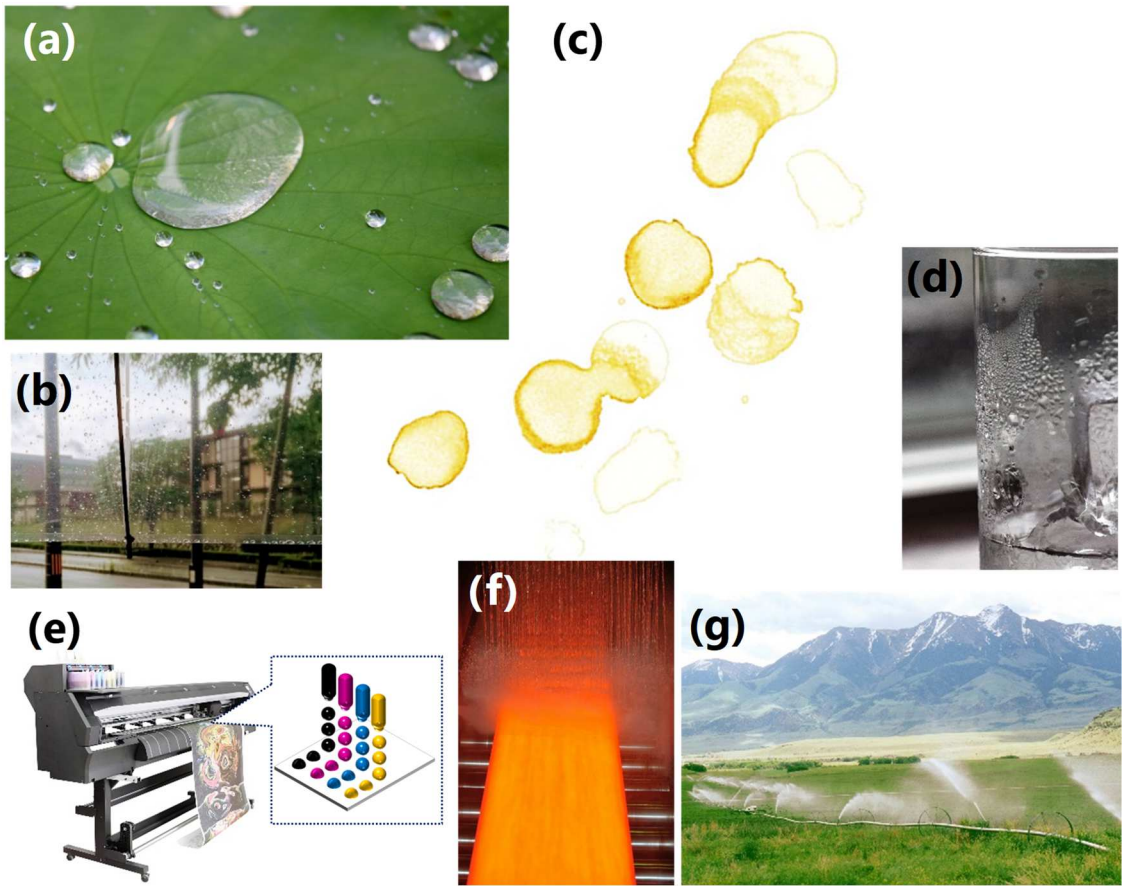

Figure 1.1 Various situations in which drops/droplets are present including rain drops on (a) a lotus leaf and (b) an umbrella, (c) coffee-stain, (d) dew drops on a glass, (e) inkjet printing, (f) cooling process of molten steel and (g) sprinkled pesticides in an agricultural field.

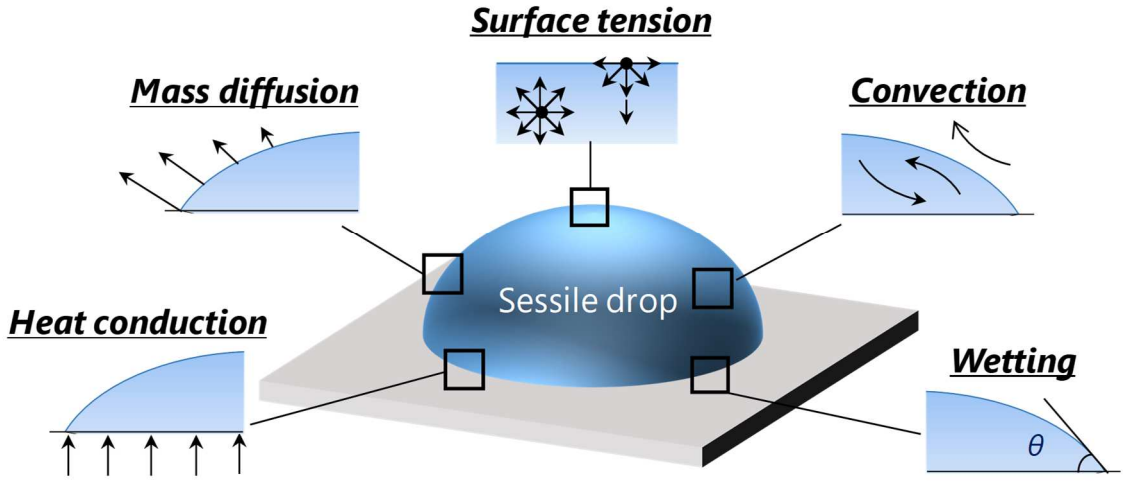

Figure 1.2 Different aspects of physics involved in a sessile drop.

scopic scales (Figure 1.2).

The first interpretation, but still the foundation of the field, to how the equilibrium shape of a drop is formed dates back to the year of 1805 when the English physicist Thomas Young [2] proposed that there should be an "*appropriate angle*" between the liquid-gas, solid-liquid and solid-gas interfaces. The "*angle*" is today called the contact angle and is subject to the forces acting along these three interfaces in order to minimise their areas.

The second problem that came up in the late 19th century was evaporation of drops, which was first rationalised by the Scottish scientist James Clerk Maxwell. In 1877, he published an article entitled "*Theory of the Wet Bulb Thermometer*" wherein drop evaporation was considered as a simple diffusion-controlled process [3]. His diffusion model has currently been proven to be although correct nonetheless insufficient: considerable contributions of other factors such as heat transfer, convection, surface tension and surface morphology to phase change phenomena are widely recognised today [4].

One of the modern interest is hydrodynamics within drops/droplets, study of which has been progressively growing since the 1980s due to rising demand for industrial and medical applications such as inkjet and polymer coating [5]–[10], micro-/nanotechnology [11]–[13], biomedical analysis and diagnosis (Figure 1.3) [14]–[17]. Especially in the biomedical field, drop-based microfluidics or "Lab-on-a-chip" devices have recently been a promising technique capable of performing laboratory operations on a single integrated circuit—a chip using a much smaller amount of reagents in significantly less time (Figure 1.4) [18]–[24]. In these devices, drops play roles as capsules to carry reagents and as reactors wherein chemical reactions take place, and hence, efficient transport and mixing of the drops are paramount.

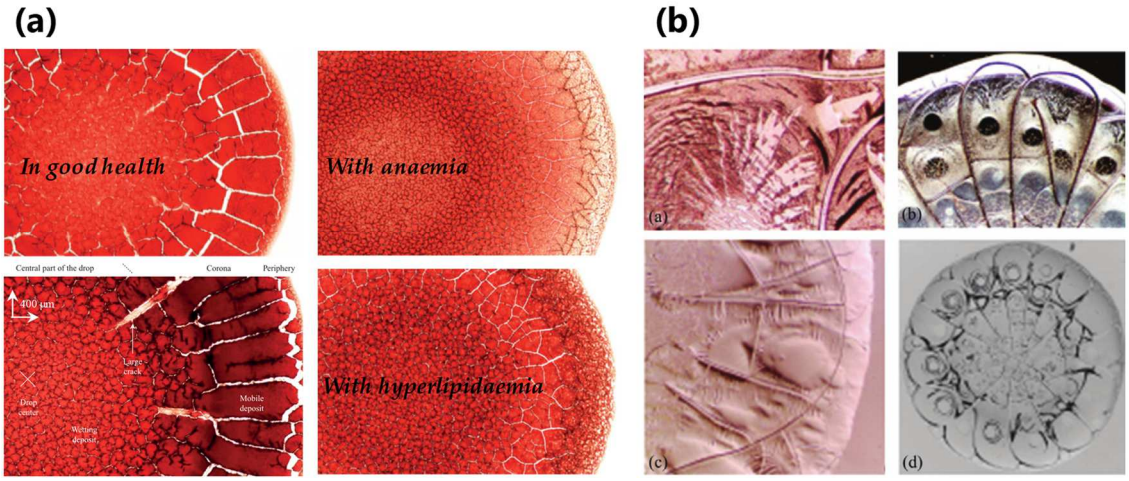

Figure 1.3 Patterns left by drying blood drops from people in good health (left panels in (a) and with different diseases (other panels). (a) and (b) are reproduced from Brutin *et al*. [16] and Sefiane [15], respectively.

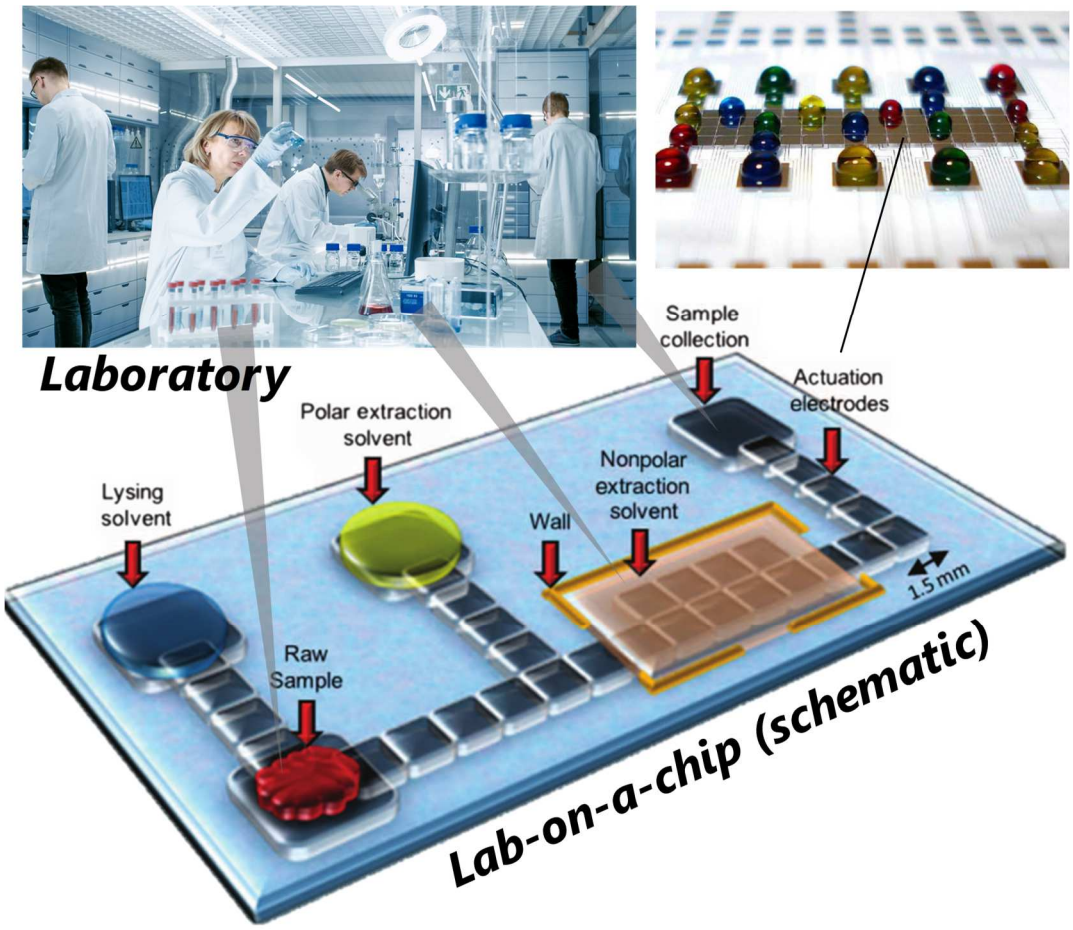

Figure 1.4 Pictorial concept of drop-based lab-on-a-chip devices. Schematic of the device (bottom) and photograph of the actuation electrodes (up-right) are adapted from [23] and [24], respectively.

Such particular functions can be added to a drop by dragging it away from the equilibrium state. Drops under a gradient of their nature *e.g*. surface tension, wettability and molar concentration become unstable (or "unhappy" as de Gennes *et al*. describe [25]). Consequently, they will drive convection, motion and/or phase change, depending on the type of gradient, in order to reach the energetically "happy" state. The comprehensive principle underpinning these actions was provided by American scientist and engineer Josiah Willard Gibbs in his pioneering article "*On the Equilibrium of Heterogeneous Substances*" [26], which formed the foundation of thermodynamics.

Capillarity is one of the tactics to functionalise a drop-based system due to the fact that surface (or interfacial) tension dominates the dynamics in micro/ millimetre-sized drops. In fact, besides abovementioned pioneers in this field, capillary phenomena have received great attention from other celebrated scientists. The first scientific article by Albert Einstein in 1901 was entitled "*Folgerungen aus den Capillaritätserscheinungen (Conclusions Drawn from the Phenomena of Capillarity)*" [27]. Another example is the Nobel Prize laureate in 1991, Pierre-Gilles de Gennes, who committed his important carrier to this subject [25], [28].

When a drop experiences a local surface-tension gradient along its free surface, molecules with a stronger surface tension will pull ones with a weaker surface tension, resulting in fluid motion. This phenomenon was first pointed out in 1855 when James Thomson interpreted the "tears of wine" [29]. In his paper, he proposed as the mechanism underlying the phenomenon, for the first time, an imbalance of surface tension arising from non-uniform alcohol evaporation. Despite his first discovery, the phenomenon is currently known as Marangoni effect, named after the Italian physicist Carlo Marangoni who demonstrated this effect resulted from a temperature variation in addition to chemical composition in his PhD dissertation [30]. In particular, surface tension of liquids is

temperature-dependent *i.e.* the higher the temperature is, the lower the surface tension becomes for typical fluids. Thus, when a temperature gradient exists at a liquid surface, a tensile force acts along the surface from the hot region toward the cold one (thermocapillary effect). Thermocapillary convection has been found in various pure liquids such as organic solvents and oils in forms of recirculating vortices and waves *i.e.* hydrothermal waves (HTWs), albeit its existence in pure water remains elusive [31]–[37]. Moreover, the nonlinearity or instability in dynamics arising from non-equilibrium systems often complicates the understanding and prediction of the phenomena.

In a similar fashion, if there is a tensile gradient along the solid-liquid interface, namely wettability gradient, one may expect the drop to move toward a high-wettability (attractive) region due to an imbalance of attraction forces acting on each side of the drop. Brochard first theoretically predicted drop motion on wettability gradients imposed by chemical and thermal principles [38]. The former was experimentally demonstrated for the first time by Chaudhury and Whitesides [39] and the latter was also proved by several researchers [40]–[42]. Besides the nature of surfaces, surface wettability can also be modified by their physical structures, which have already been put into practice by some wild creatures over their evolution (Figure 1.5): dessert beetles, for example, collect drinking water from moist wind using their bumpy backs [43]. Spider silk with micro-/nanoscale structural features can transport water by the resultant surface energy gradients [44]. However, the lack of our understanding of dynamic wetting phenomena *e.g.* contact line pinning and surface-kinetic energy conversion has made the development in this field challenging despite a great progress in bio-inspired surface manufacturing [45].

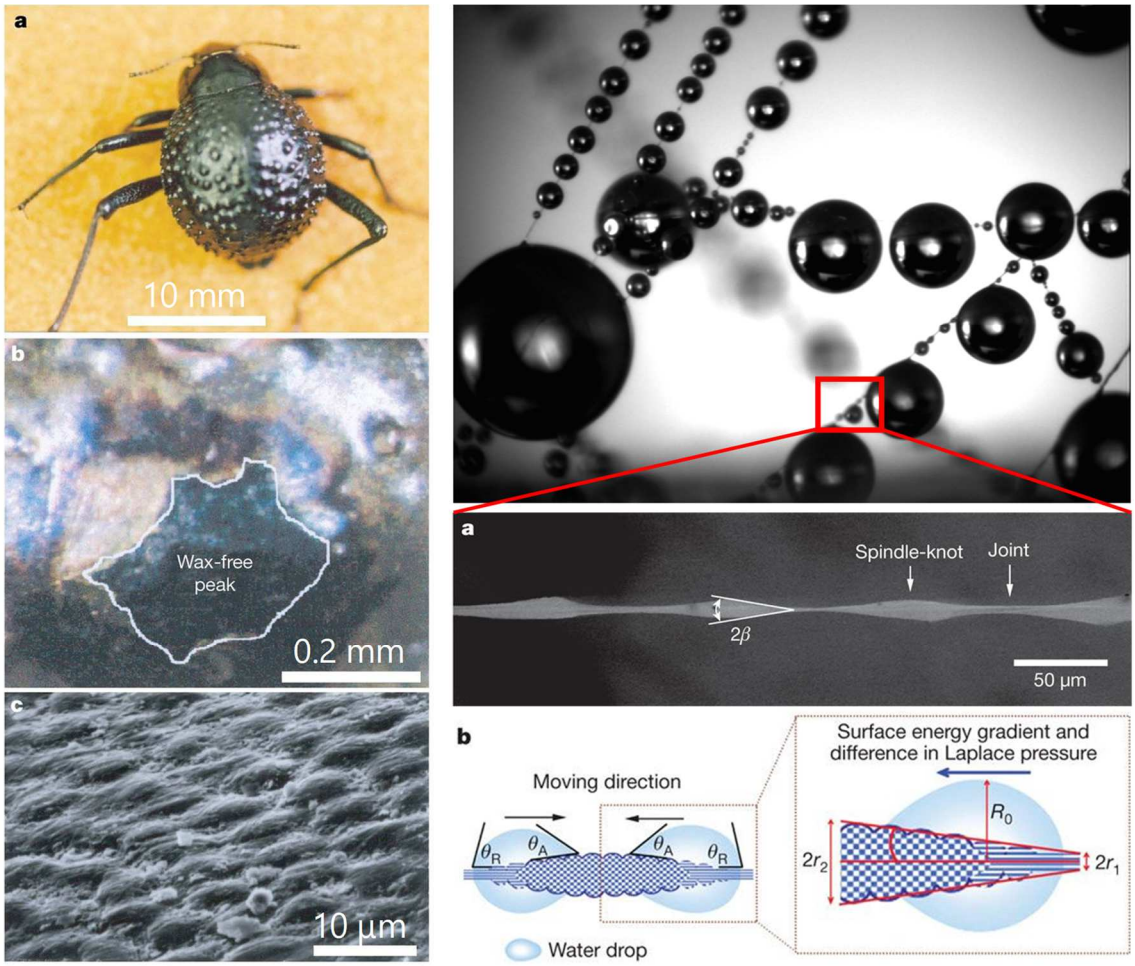

Figure 1.5 Surface structures of a desert beetle (left [43]) and spider silk (right [44]) capable of collecting water from moist air.

This thesis aims to contribute to the field of thermocapillary instabilities and wetting dynamics of drops under thermal and wettability gradients along the interfaces. These phenomena are not only of fundamental scientific interest but also the key issues for the aforementioned drop-based applications. Before proceeding to the present experimental work and discussions, this chapter will describe fundamental notions of physics involved in drops to establish the basic knowledge of the subject matter. Then, a brief review of the recent works in the fields that this thesis particularly focuses on will be given in order to highlight the latest advances as well as remaining problems, which will eventually identify the objective of the present study.

1.2 Fundamentals of Drops

A sessile drop, a small cluster of molecules sitting on a solid surface, may seem like a simple system at first glance. However, the presence of drops originates in interplay of many physical mechanisms including wetting, phase change, heat transfer and convection. Each of these aspects takes place at the molecular scale and can be very complex. This section briefly introduces basic knowledge of physics related to the focus of the thesis, which has been widely accepted in the field. More complete description of the phenomena can be found in the books such as "*Interfacial Science* [46]", "*Capillarity and Wetting Phenomena* [25]" and "*Droplet Wetting and Evaporation* [47]".

1.2.1 Surface tension

When considering a system in which a liquid and its vapour coexist in a space *i.e.* a two-phase system, one may define a sharp boundary between the liquid and vapour phases, namely a surface. At the molecular scale, in fact, the surface is a layer wherein physical values (*e.g.* density) vary as depicted in Figure 1.6. In the liquid phase, neighbouring molecules interact each other with the cohesive forces such as van der Waals forces and/or hydrogen bonds. The net force acting to each molecule is zero in the bulk liquid phase since they are attracted equally in every direction. By contrast, a molecule wandering near the surface has more neighbours on the liquid-phase side than on the vapour side, leading to a net force toward the liquid side normal to the surface. This resultant force is called the surface (or interfacial) tension and acts such that the surface forms a possible shape with a minimum area.

In terms of energy, another aspect of surface tension, an interior molecule possesses a lower energy than that at the surface since it consumes more energy to interact with surrounding molecules. However, a molecule at the surface has fewer neighbours to attract on the vapour-phase side, resulting in a higher energy

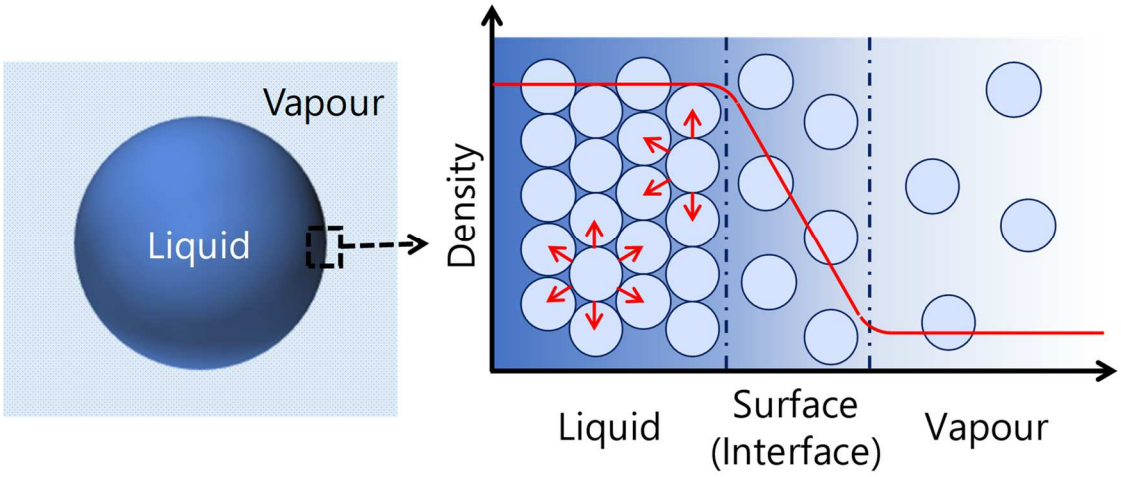

Figure 1.6 Pictorial representation of (left) a liquid/vapour system and (right) schematic molecular distribution in the vicinity of the liquid-vapour interface. The fluid density through the phases is plotted in red. Red arrows depict the interactive forces between neighbouring molecules.

state. This "unused energy" is the surface free energy and a larger surface area leads to higher surface free energy. For the system to be the minimum energy state, the surface area must be minimised to reduce the number of molecules experiencing an imbalance of attraction: a sphere has the smallest surface area for a given volume.

Surface tension, denoted as σ_{LV}, can be quantified as the surface free energy per unit area (J/m^2), which can be equivalently expressed as the force per unit length (N/m). σ_{LV} depends on the nature of the liquid as well as the temperature and pressure. Typical values of the surface tension of a few common liquids are listed in Table 1.1.

Note that the term "surface" is specific to a boundary between liquid (or solid) and vapour phases. On the other hand, "interface" is a general term which includes boundaries between multiple immiscible fluids or between fluids and solids.

Table 1.1 Typical surface tension values of water, ethanol, acetone, glycerol and mercury at 20 °C under atmospheric pressure [25].

Liquid	Water	Ethanol	Acetone	Glycerol	Mercury
σ_{LV} (mN/m)	73	23	24	63	485

1.2.2 Wetting of drops

Ideal surfaces

A perfect sphere of liquid is rarely seen around us since drops/droplets with a certain volume can hardly stay still in the air: for example, raindrops and sprayed mist eventually fall due to gravity and come into contact with solid surfaces. Wettability refers to the ability of a solid surface to attract a liquid or of a liquid to keep contact with a solid surface. When a homogeneous solid surface "moderately" attracts a liquid so that it will be partially wet, liquid, vapour and solid phases will coexist in the system, bounded by three interfaces *i.e.* liquid-vapour, solid-liquid and solid-vapour. The line where those three phases meet is called the triple-phase contact line, or just the contact line. Due to the action of interfacial forces, the contact line is pulled by each interface resulting in an equilibrium shape of the drop. Wettability is a result from the balance between those three forces at the contact line, which can be quantified using a macroscopic measure, contact angle (Figure 1.7). In 1805, Thomas Young proposed a pioneering relation between the contact angle and the interfacial tensions [2], which was later formulated by Athanase Dupré and Paul Dupré [48]:

$$\sigma_{LV} \cos \theta_E = \sigma_{SV} - \sigma_{SL}, \tag{1.1}$$

where θ_E is the equilibrium contact angle, σ the interfacial tension, and subscripts LV, SV and SL denote the liquid-vapour, solid-vapour and solid-liquid interfaces, respectively. Based on the contact angle, wettability can be categorised into two

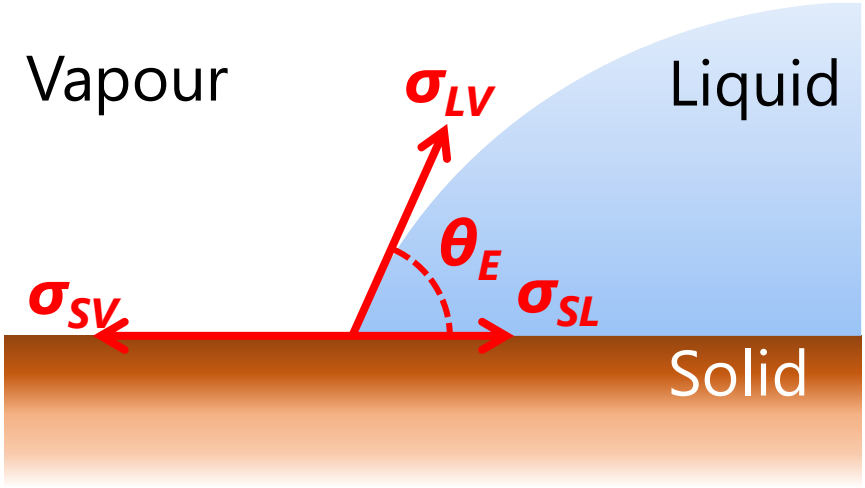

Figure 1.7 Schematic illustration of Young's relation, Eq. (1.1).

levels: hydrophilic ($\theta_E < 90°$) and hydrophobic ($\theta_E > 90°$).

Real surfaces—Wetting dynamics

Young's relation assumes an ideal surface *i.e.* chemically and physically homogeneous whereas real surfaces quite often contain either chemical (stains, blotches, blemishes) or physical (surface roughness) heterogeneities. Due to such deviations from ideality, the contact angle θ can vary within a certain range—the contact angle hysteresis (CAH). For instance, if one tilts a surface on which a drop sits (Figure 1.8), the drop can still remain at the original position despite gravity. Instead, θ on the downside exceeds θ_E without any motion of the contact line until it reaches a threshold value θ_{adv} (referred to as the advancing contact angle) beyond which the contact line finally proceeds. Likewise, θ on the other side of the drop decreases below θ_E with the contact line being pinned. When θ reaches the receding contact angle θ_{rec}, the contact line shifts in such a way that the liquid retreats from the surface. Eventually, the drop will move downhill when θ on both sides attain to θ_{adv} and θ_{rec}, respectively. Therefore, CAH can be defined as the difference between θ_{adv} and θ_{rec}: CAH = $\theta_{adv} - \theta_{rec}$. CAH is a critical characteristic of dynamic wetting in which motion of interfaces is involved: a drop will be immobile if CAH is large.

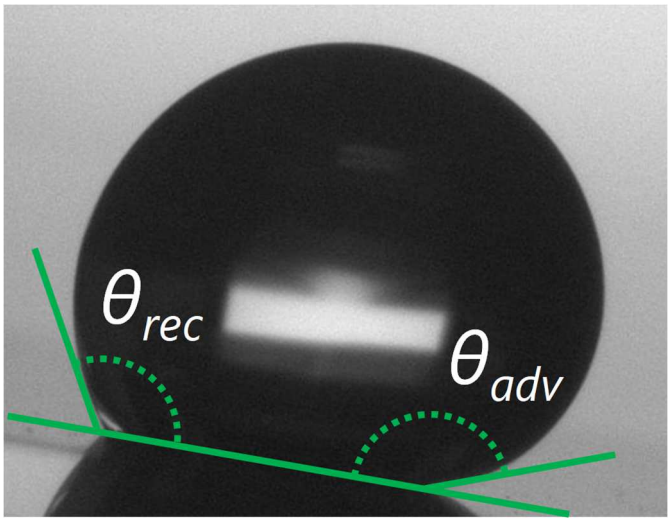

Figure 1.8 Drop on a tilted surface, exhibiting the limit contact angles θ_{adv} and θ_{rec} before it slides off.

The comprehensive review of general wetting dynamics from a theoretical perspective has been given by de Gennes [28].

Effect of roughness

A typical non-ideal wetting situation is a drop on a surface with rough structures. Surface roughness is known to greatly influence the wettability as well as drop mobility. In what follows, two famous models that describe different wetting regimes (complete and composite solid-liquid contact) on rough surfaces are introduced.

Wenzel in 1936 [49] was the first to explain the contact angle deviating from θ_E when a surface has asperities with the roughness factor r defined as the ratio of the actual surface area to the projected (apparent) area, therefore $r > 1$. When the liquid completely wets all the peaks and valleys of the surface(Figure 1.9 (a)), the apparent contact angle θ_{app} follows the relation:

$$\cos\theta_{app} = r\cos\theta_E. \qquad (1.2)$$

Eq. (1.2) implies that surface roughness magnifies the intrinsic wetting properties of the liquid and solid *i.e.* if $\theta_E < 90°$, $\theta_{app} < \theta_E$, and vice versa.

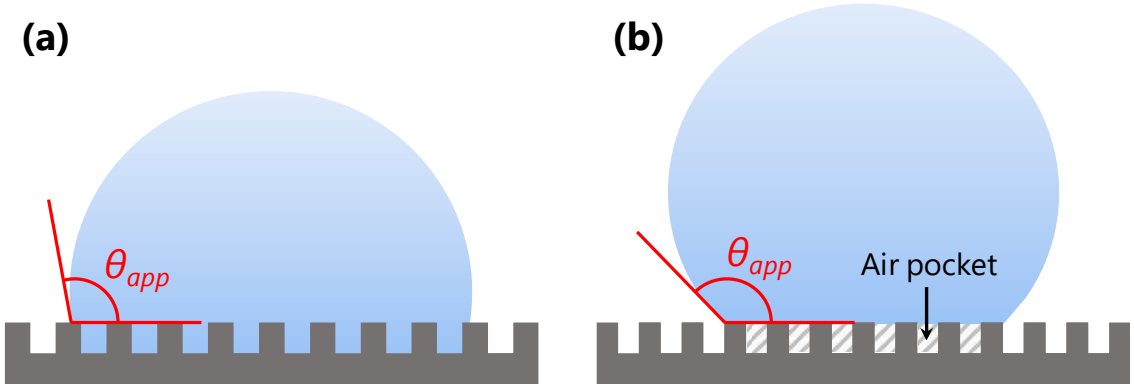

Figure 1.9 Schematic models of two different wetting states on rough surfaces: (a) Wenzel and (b) Cassie-Baxter states.

In contrast to the Wenzel model, Cassie and Baxter in 1944 [50] considered the heterogeneous wetting scenario: the liquid only contacts the top of the asperities, trapping air underneath the drop and between the structures (as shown in Figure 1.9 (b), often referred to as a "fakir" drop [51], [52]). Defining the surface area fraction of the solid that touches the drop as ϕ, the apparent contact angle θ_{app} of the fakir drop can be expressed by

$$\cos\theta_{app} = -1 + \phi(\cos\theta_E + 1). \quad (1.3)$$

For a Cassie-Baxter (CB) regime to be stable (energetically favourable), θ_E must be larger than a critical value θ_c, which can be derived by the energy comparison between Wenzel and CB regimes *i.e.* $\cos\theta_c = (\phi - 1)/(r - \phi)$. In practice, the CB regime can be metastable even if $\theta_E < \theta_c$. In the CB wetting state, a drop attains θ_{app} higher than 150° and exhibits small CAH (high mobility) compared with that in the Wenzel state. Such "superphobicity" can be found in nature *e.g.* lotus leaves and water strider's legs and today, we are able to mimic these wetting characteristics by virtue of the recent development of microfabrication techniques and hydrophobic coating materials (Figure 1.10).

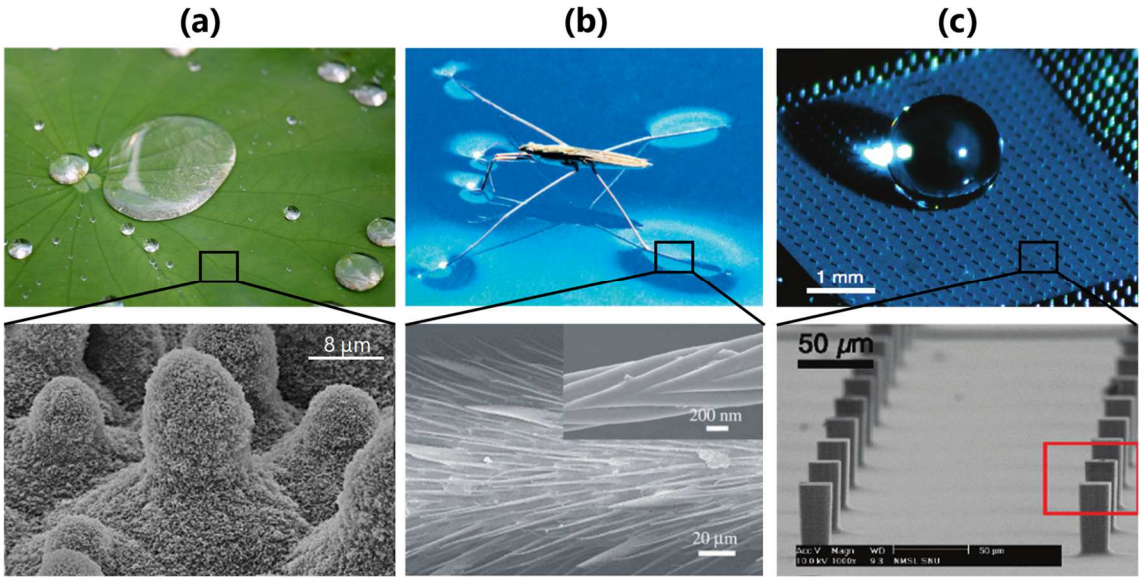

Figure 1.10 Exemplary photographs (upper panels) and scanning electron microscopic images (lower panels) of superhydrophobic rough surfaces: (a) a lotus leaf (lower panel is reprinted from [53]), (b) legs of a water strider [54] and (c) a surface with engineered micropillars [55].

Contact angle measurement

As described above, the contact angle is an essential factor that quantifies the wettability of a solid surface and determines what a drop will look like. Therefore, it is crucial to precisely measure contact angles for sessile drop analysis. From an image of a sessile drop viewed from the side (Figure 1.11), one can readily find the base radius R_{base} and the height of the drop H. Using these values, the equilibrium contact angle θ_E can be simply obtained by the half-angle method:

$$\theta_E = 2\tan^{-1}\frac{H}{R_{base}}. \tag{1.4}$$

In this method, the drop profile is assumed to be a circular arc and axisymmetric, which is quite often far-fetched in real situations. Alternatively, the polynomial fitting method [56] finds an angle of tangent of the drop contour at the triple-phase contact point (Figure 1.11). In particular, the contour near the baseline is fitted with a polynomial function and the contact angle can be calculated as the

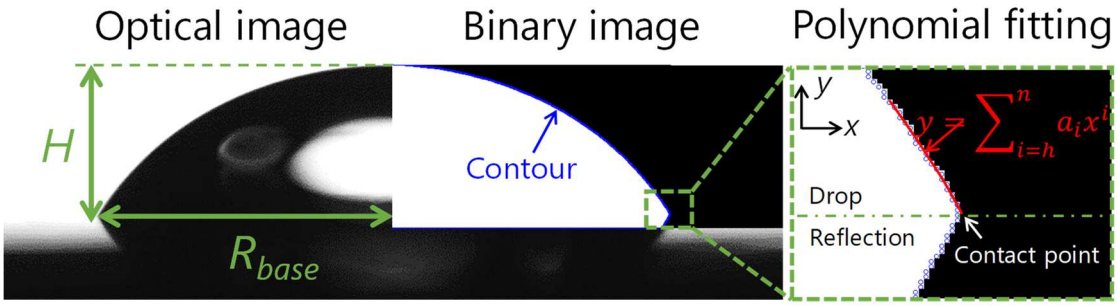

Figure 1.11 Side view of a sessile drop taken by (left) an optical camera and (right) the binary image. The definitions of the height H, the base radius R_{base} are indicated with the green arrows, respectively. The red line shows a polynomial curve fitted along the drop contour near the contact point.

slope of the fitted curve at the contact point:

$$\theta_E = \tan^{-1}\left(\frac{dy}{dx}\right)_{\text{Contact point}} = \tan^{-1}\left\{\frac{d\left(\sum_{i=0}^{n} a_i x^i\right)}{dx}\right\}_{\text{Contact point}}, \quad (1.5)$$

where x and y are Cartesian coordinates, and a_i is the polynomial coefficient. Unlike the half-tangent method, the polynomial fitting method has no assumptions regarding the profile of the drop contour. Hence this approach is highly flexible to the contour of non-spherical drops and even asymmetrical ones, which further enables dynamic contact angle measurements with a tilting stage (Figure 1.8).

1.2.3 Shape of Drops

Properly tracing a drop profile is important for any experimental and theoretical study with drops. The drop shape is determined by capillary and gravitational forces and therefore, the static Bond number Bo is normally used as a criterion to evaluate which force will dominate the drop profile. Essentially, Bo measures the importance of gravity compared to capillarity and can be expressed as

$$Bo = \frac{\rho g R^2}{\sigma_{LV}}, \quad (1.6)$$

where ρ is the density, g the acceleration due to gravity and R the characteristic radius of the drop. Notably, *Bo* smaller than unity (*Bo* << 1) suggests that the surface tension mainly dominates and thus, such drops shall form a spherical cap. In contrast, if *Bo* > 1, then gravitational forces come into play and the drop shape will deviate from spherical.

Many of the works reported to date assumed a spherical cap as they usually dealt with small drops which satisfied *Bo* << 1. In such situations, one may obtain a simple relation between the volume V, the areas of the spherical cap (A_{cap}) and drop base (A_{base}), R and θ_E as

$$V = \frac{\pi R^3 (1 - \cos\theta_E)^2 (2 + \cos\theta_E)}{3\sin^3\theta_E}, \tag{1.7}$$

$$A_{cap} = \frac{2\pi R^2}{1 + \cos\theta_E}, \qquad A_{base} = \pi R^2 \sin^2\theta_E . \tag{1.8}$$

In spite of the fact that *Bo* for water with V = 80 μL in normal gravity (*i.e.* ρ = 998 kg/m^3, g = 9.8 m/s^2 and σ_{LV} = 73 mN/m) still remains smaller than unity, even a 10 μL water drop will be significantly flattened due to gravity. Shape of such large drops shall follow the Young-Laplace equation, which determines the curvature at any point of a drop accounting for the gravitational effect [57]:

$$\sigma_{LV}\left(\frac{1}{R_1} + \frac{1}{R_1}\right) = \rho g H + \frac{2\sigma_{LV}}{R}, \tag{1.9}$$

where R_1 and R_2 are the principal radii of curvature at any point of the drop. Eq. (1.9) can only be solved numerically or analytically using approximations [58]. Figure 1.12 shows drop profiles predicted from numerical solution of Eq. (1.9), analytical approximation solution and spherical assumption for different *Bo* ranging from 0 to 3.6.

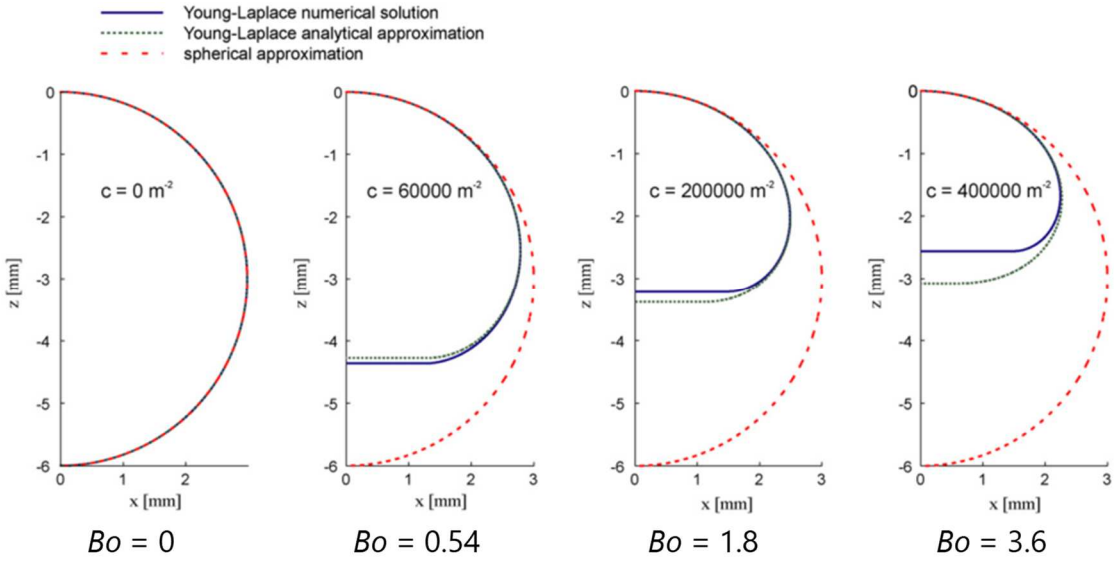

Figure 1.12 Half drop profiles calculated from numerical integration of the Young-Laplace equation, Eq. (1.9) (blue line), analytical approximation (green dotted line) and spherical approximation for a drop with R = 3 mm, θ_E = 180° and various Bo indicated below each panel [58].

1.2.4 Drop evaporation

Diffusion model

In the very vicinity of the liquid-vapour interface, one observes molecules going from the liquid to the vapour phase and vice versa. If the vapour phase is not saturated with the molecules, more will leave the liquid phase than those coming into, resulting in a decrease in mass/volume of the liquid—evaporation. Natural drop evaporation is essentially controlled by the vapour diffusion into the vapour phase, which follows Fick's law.

Maxwell [3] was the first in 1877 and Langmuir [59] the second in 1918 to describe the evaporation of a sphere drop based on the diffusion theory. Both derived the rate of mass decrease as $-dm/dt = 4\pi R D_{AB}(c_s - c_\infty)$, where m denotes the mass, t the time, D_{AB} the diffusion coefficient, c_s and c_∞ the vapour concentrations at the interface (saturated) and the surroundings, respectively.

In the case of sessile drops, the existence of a solid surface drastically changes

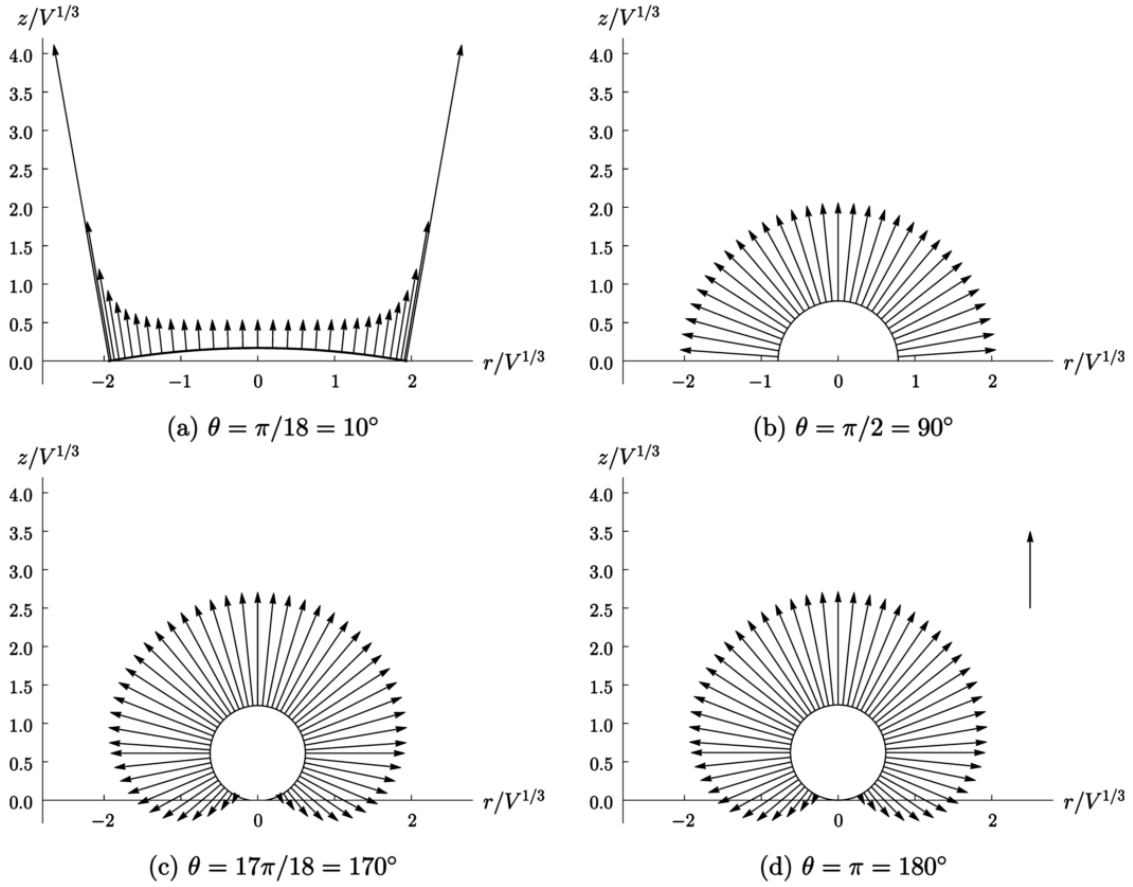

Figure 1.13 Distribution of the evaporative flux along the surfaces of drops with different contact angles: (a) θ = 10°, (b) θ = 90°, (c) θ = 170° and (d) θ = 180° [60].

the evaporative behaviour. Unlike spherical drops, in fact, the mass flux distribution along the surface of a sessile drop is not uniform and can be expressed as a function of the contact angle. Applying Maxwell's analogy with electrostatics to the sessile drop case, Picknett and Bexon [61] obtained the rate of evaporation as

$$-\frac{dm}{dt} = \pi R_{base} D_{AB} \left(c_s - c_\infty\right) f(\theta), \tag{1.10}$$

where $f(\theta)$ is the drop shape factor, which is a function of the contact angle. The analytical and approximated expressions of $f(\theta)$ have been proposed by many relevant works such as Hu and Larson [62] and Popov [63]. Figure 1.13 shows the evaporative flux numerically solved for drops with different contact angle [60].

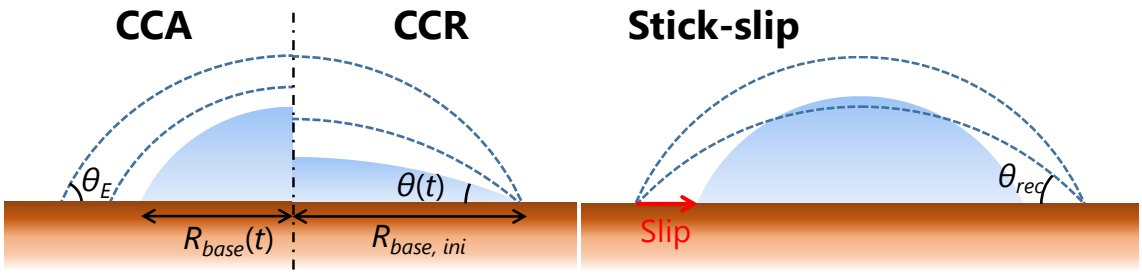

Figure 1.14 Schematic representation of drop evaporation modes: (left) constant contact angle (CCA), (middle) constant contact radius (CCR) and (right) stick-slip.

Evaporation modes

As a sessile drop evaporates, its shape shall change. The evaporation mode describes how the drop shape evolves during the evaporation. Two extreme modes and their mixed mode are usually observed (Figure 1.14):

1. Constant contact angle (CCA) mode. A drying drop keeps its aspect ratio. In other words, the contact line recedes with θ being kept constant *i.e.* θ_E during the evaporation. CCA mode is considered ideal since it can only be realised when any contact angle hysteresis (CAH) is absent.
2. Constant contact radius, CCR. The second extreme case is a drop evaporating with its contact line being fixed over the lifetime. Simultaneously, θ decreases in order to adapt to the volume loss.
3. Mixed or stick-slip mode. In most actual situations, a drop begins to evaporate in CCR mode where the contact line is pinned due to CAH (stick). θ decreases as the evaporation proceeds until it reaches θ_{rec}, at which point the contact line begins to slide, recovering θ.

The evaporation modes depend on the wetting properties of the solid surface, especially CAH, and strongly influence the drop lifetime [61], [64]–[66].

Influential factors

Although drop evaporation is mainly limited by vapour diffusion, there are many factors that affect the evaporation behaviour [4]. In addition to vapour concentration gradients and wettability, substrate thermal properties [67]–[70], substrate heating [71]–[73], internal/external convection [72], [74]–[76] and components in liquid and vapour phases [77]–[80] are known to contribute to drop evaporation.

1.3 Literature Review

Having established the fundamentals of wetting and evaporation of drops, let us now further look at recent research topics including fluid motion inside drops and drop manipulation using capillary phenomena.

1.3.1 Flows in drops

Impacts of fluid flows on drop-based applications

Control of convection/flow in liquid drops has been a key issue, for decades, as a fundamental phenomenon involved in inkjet printing/polymer coating [5]–[7], [9], [81], [82], DNA mapping [83]–[87], and pattern formation [88]–[90] to name a few. In these applications, uniform particle deposition is normally desired and internal flows of a drop plays a principle role in transporting particles during the which is responsible for the ring-like pattern formation. Figure reproduced from Deegan *et al*. [34]. evaporation. Moreover, as mentioned above, use of drops as a working fluid in microfluidic "Lab-on-a-chip" devices has recently been explored [18]–[22], [91]. In these devices, efficient mixing inside a drop is paramount for reducing time of chemical reaction or biomedical diagnosis [22], [92]–[96]. However, in a millimetre sized drop whose Reynolds number is usually low, the mixing rate often relies on mass diffusion, making the process optimisation challenging [94], [96]. In what follows, three different types of fluid

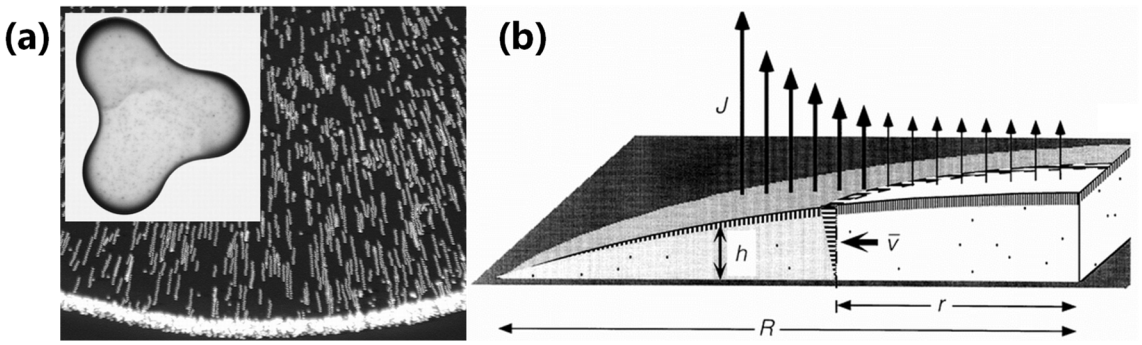

Figure 1.15 (a) Small spheres in a water drop during evaporation accumulated at the edge. The inset is a stain left by a 2 cm-diameter drop of coffee having dried on a solid surface. (b) Schematic illustration depicting the mechanism of the outward capillary flow

motion in pure drops, which originate in evaporation and temperature gradients, are reviewed with the recent experimental/theoretical reports.

Outward capillary flow

Although a drop of coffee is a solution of colloidal particles dispersed over entire liquid, it leaves a concentrated, ring-like stain along the periphery after its evaporation (Figure 1.15 (a)). Why? Deegan *et al*. first attempted to explain so-called "*coffee-ring effect*" as a deposition of particles transported toward the drop edge by the capillary, outward flow [34]. This outward flow is induced by the non-uniform evaporation flux over the drop (Figure 1.15 (b)). In particular, as shown in Figure 1.13, a drop whose θ is smaller than 90° evaporates mainly from the vicinity of the contact line. The fluid then begins to flow radially toward the edge to replenish the liquid lost by evaporation. The resultant outward flow is capable of carrying virtually all the dispersed materials to the periphery. The coffee-ring effect is detrimental to practical applications such as inkjet printing, coating, crystal growth and DNA mapping, which require uniform deposit. There have been several techniques proposed to suppress this effect by adding elongated particles [97]–[99], solvents with different volatility [9], wettability modification [73], [100], electrowetting and acoustic principles [101], [102].

Natural convection

When a drop on a horizontal substrate evaporates freely under isothermal condition, the drop will cool down as the energy required for the molecules to leave the drop is consumed (the latent heat). Heat will be then supplied from the substrate if it is thermally conductive, giving rise a temperature gradient across the entire drop. The temperature profile has been identified experimentally and theoretically, that the temperature becomes colder at the apex than the bottom due to the differential length of heat conduction path [72], [103]–[105]. This thermal gradient will be pronounced when heating the substrate.

With such temperature profile (colder at the apex than the edge), one may expect an emergence of buoyancy-driven natural convection inside the drop. Kang *et al*. [106] performed experimental and numerical investigations of natural convection in evaporating aqueous solutions of NaCl. They presented the particle image velocimetry (PIV) and computed velocity fields which showed a pair of vortices that recirculated particles in an opposite direction to the outward capillary flow.

More recently, Dash *et al*. [95] reported different flow patterns in water drops depending on substrate temperature as well as the degree of hydrophobicity (Figure 1.16 (a)). As a systematic analysis, they attempted to scale the flow velocity by the non-dimensional Rayleigh number *Ra*:

$$Ra = \frac{\beta g H^4 \Delta T}{\nu \alpha R} \ , \tag{1.11}$$

where β denotes the coefficient of thermal expansion, ν the kinematic viscosity, , α the thermal diffusivity and ΔT the temperature difference. It is readily apparent from Eq. (1.11), that *Ra* represents the magnitude of buoyant force compared to viscous force. In their work, PIV was also conducted and the velocity was found to increase proportionally as *Ra* increases (Figure 1.16 (b) and (c)), leading to the conclusion that the flow was buoyancy in origin.

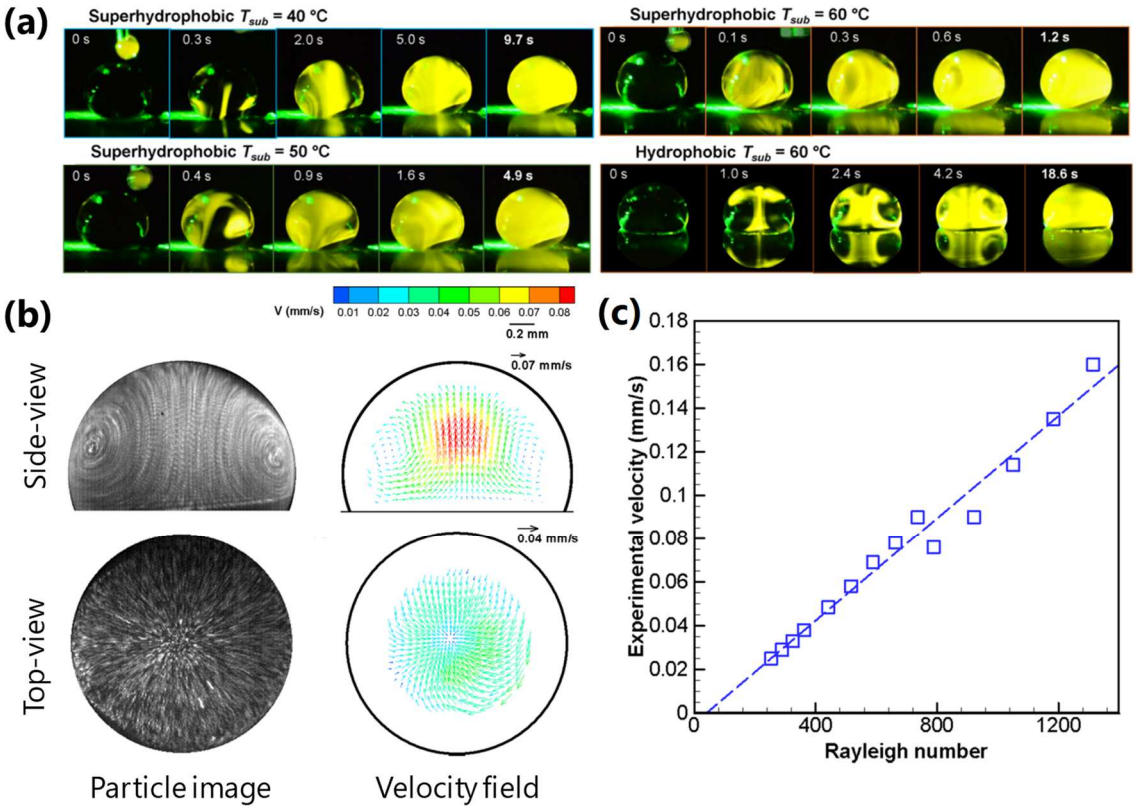

Figure 1.16 Buoyancy-driven natural convection in water drops on substrates with different temperature and wettability. (a) Temporal snapshots demonstrating dye mixing in evaporating water drops on a superhydrophobic substrate kept at (upper-left) 40 °C, (lower-left) 50 °C, (upper-right) 60 °C, and (lower-right) on a hydrophobic substrate kept at 60 °C. (b) Flow visualisation and velocity maps inside a drop on a hydrophobic surface maintained at 50 °C. (c) Maximum velocity measured for each drop as a function of Rayleigh number. Figure reproduced from Dash *et al*. [95].

Except for the superhydrophobic cases, the natural convection in the drops was such that the fluid was lifted upward at the centre and it returned along the liquid surface which acted as a wall. Then, the fluid flowed inward along the substrate and eventually recirculated. The flow velocity due to natural convection was reported to be typically order of 10–100 μm/s. These experimental observations have been corroborated by numerical simulations such as Kang *et al*. [106], Pan *et al*. [107], and Pradhan and Panigrahi [108].

Thermocapillary convection

For a drop whose size is comparably small as the capillary length $\lambda_c = \sqrt{\sigma_{LV}/\rho g}$, capillary forces predominate the dynamics. As described in subsection 1.2.1, surface tension varies as a function of temperature T: $\sigma_{LV}(T) = \sigma_{LV}(T_0) - (-\partial\sigma_{LV}/\partial T)(T - T_0)$ for pure liquids. Therefore, temperature gradients arising across the drop due to its evaporation and/or heating can lead to surface tension gradients, which in turn induce forces acting along the surface, from the hot region, where σ_{LV} is small, to the cold region, where σ_{LV} is large. This force is called the thermocapillary force and is capable of driving a fluid flow *i.e.* thermocapillary or Marangoni convection. The dimensionless Marangoni number *Ma* measures the strength of the thermocapillary force compared with viscous one and can be expressed as

$$Ma = -\frac{\partial\sigma_{LV}}{\partial T}\frac{H^2\Delta T}{\rho\nu\alpha R} \ . \tag{1.12}$$

Considering the stability of a horizontal liquid layer subject to a temperature gradient, Pearson [109] proposed the critical *Ma* for the Marangoni convection to ensue as $Ma \approx 80$.

Numerous experimental and numerical studies have revealed the characteristics of Marangoni flows in a drop of various liquids and their influences on evaporation, heat transfer and pattern formation.

Ruiz and Black [74] developed an axisymmetric numerical model to demonstrate the contribution of the surface-tension-driven fluid motion to heat transfer and evaporation (Figure 1.17 (a)). Hu and Larson [104] then theoretically investigated the effect of contact angle on the velocity field and the temperature profile developed by Marangoni effect. In their numerical solutions, a strong recirculating flow along the liquid-vapour interface from the edge to the apex of the drop was observable when the contact angle was high (Figure 1.17 (b)).

In the experimental work done by Hu and Larson [32], a strong recirculating flow in octane drops was clearly visualised by means of fluorescent particle illumination. The flow regime resembled that predicted by their numerical simulation (Figure 1.18 (a)). Moreover, they stressed the possibility that the Marangoni effects could reverse coffee-ring depositions (Figure 1.18 (b)).

Chandramohan *et al*. [110] carried out PIV and reported strong Marangoni convection in volatile organic drops on a nonwetting surface. The velocity in the drop was reported to be on the order of 10–45 mm/s for a high contact angle, leading them to stress the importance of Marangoni flow in heat transfer within the drop and in predicting the evaporation rate.

It was a decade ago when Sefiane *et al*. in 2008 made use of infrared (IR) thermography for the first time to unveil thermal activities in volatile drops *e.g*. ethanol, methanol and FC-72 [33]. These drops displayed wave-like thermal instabilities propagating across the drop surface, which were similar to so-called hydrothermal waves (HTWs) as conventionally observed in thin liquid layers and disks [111]–[115]. What was unique in the case of evaporating drops is the fact that HTWs were self-excited: thermal gradients that drove the instability were generated spontaneously by the evaporative cooling effect whereas a radial temperature gradient needed to be imposed in liquid layers. Figure 1.19 presents IR thermal images of drying drops of water, methanol and FC-72 reported by Sefiane *et al*. [33] as well as HTWs in an annular liquid disk imaged by the shadowgraph technique shown by Garnier *et al*. [115].

Following the criterion proposed by Garnier *et al*. [115], that is the dynamic Bond number Bd—the ratio of buoyancy over thermocapillarity *i.e*. $Bd = Ra/Ma$, Sefiane *et al*. identified the thermal patterns as HTWs induced by Marangoni effects as $Bd \ll 1$. This fact was further supported by a linear stability analysis completed by Karapetsas *et al*. [116] and more directly by Carle *et al*. [117] who observed the same thermal patterns regardless of gravity during parabolic flights.

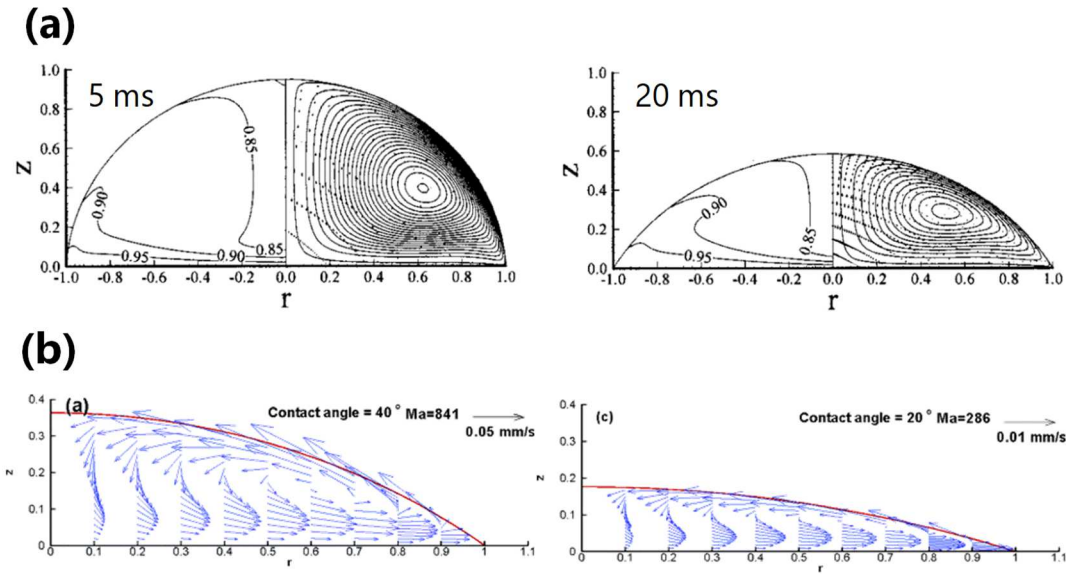

Figure 1.17 Numerical simulations of Marangoni recirculation in an evaporating drop. (a) Temporal evolution of isotherm (left) and stream (right) contours for a water drop with an initial base diameter of 0.1 mm on a 100 °C substrate [74]. (b) Velocity fields on a drop with different contact angles, 40° and 20° [104].

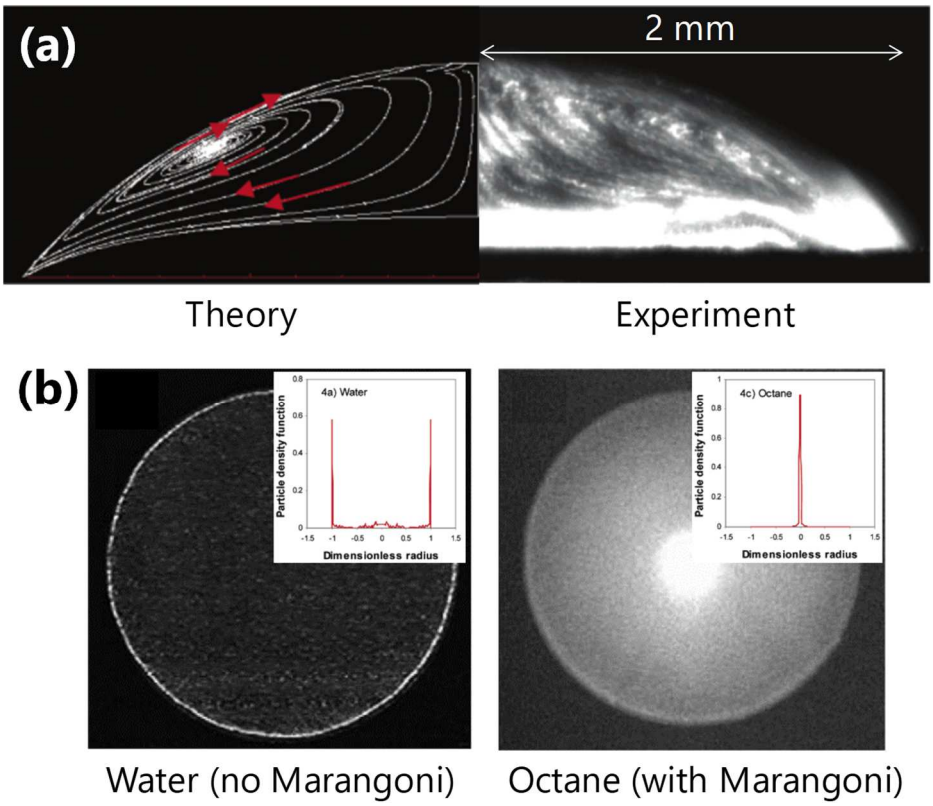

Figure 1.18 (a) Visualisation and prediction of flow in a drying octane drop. (b) Deposition patterns of fluorescent particles left after evaporation of (left) water and (right) octane drops. Insets are particle distributions across the deposition. Figure reproduced from Hu and Larson [32].

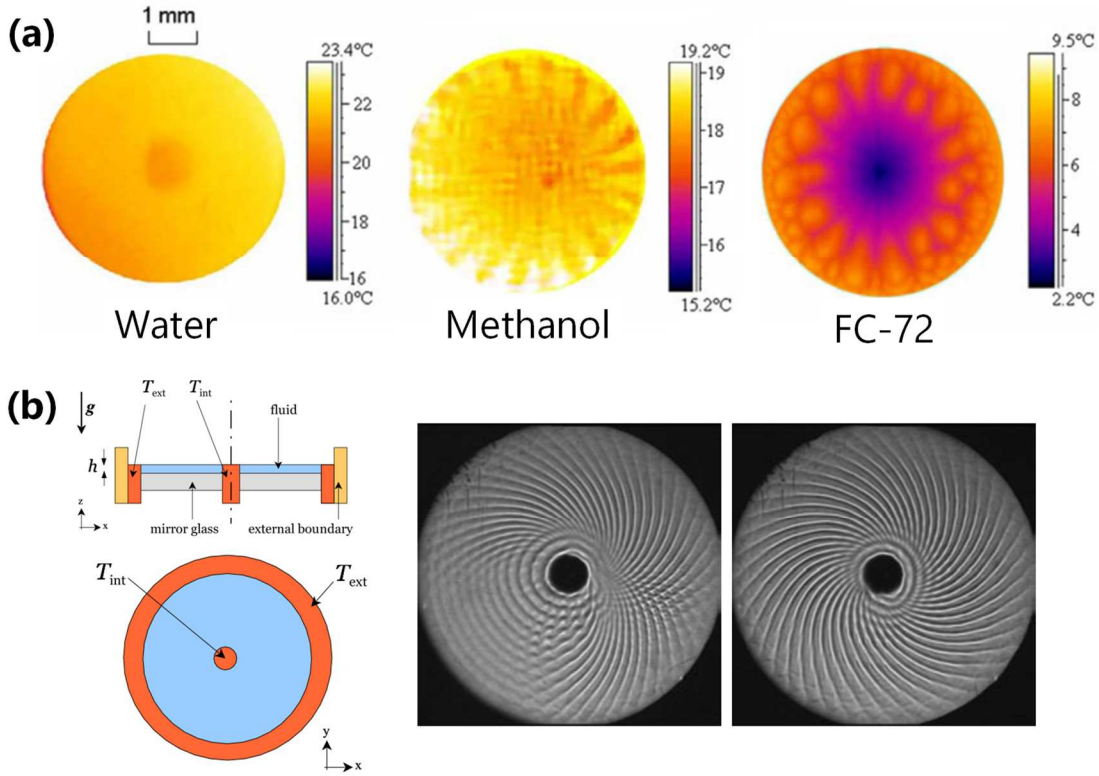

Figure 1.19 Hydrothermal waves (HTWs) in evaporating drops and an annular liquid layer. (a) Temperature maps of water, methanol and FC-72 drops obtained by IR thermography [33]. (b) Shadowgraphs of an annular, thin disk of silicon oil where a temperature difference was imposed from the centre (cold) to the exterior (hot) [115].

Since their pioneering findings, a lot of effort has been made to investigate the contribution of HTWs to evaporation and heat transfer [118], and the effects of substrate thermal conductivity [119], heating [37], [118], [119], atmospheric component or humidity [79], [120] and the geometry of drops [121] on HTWs.

In spite of abundant experimental [31]–[33], [37], [110], [117]–[119], [121] and theoretical [72], [104], [105], [116], [122]–[127] evidence of Marangoni flows in evaporating drops of highly volatile liquids, the existence of which in pure water remains controversial [128].

Many theoretical works have predicted vigorous thermocapillary-driven recirculating flows in water, such as Ruiz and Black [74], Hu and Larson [104], Girard *et al*. [122], Yang *et al*. [105] and Sáenz *et al*. [126]. However, there has been

little experimental corroboration despite a number of attempts made for more than a decade [32], [33], [35]–[37], [126], [129], [130].

Savino *et al*. [129] captured motion of tracers in evaporating hanging drops and reported an absence of Marangoni convection in water, albeit n-octane exhibited the convection. The same conclusion was made by Hu and Larson [32] who looked at the deposition pattern after a water drop dried: a clear ring-like deposition was formed due to the outward flow while the Marangoni-driven reversal of the coffee-ring effect was evident for octane drops (Figure 1.18 (b)). Sefiane *et al*. [33] reported no thermal activities on the surface of a water drop viewed by IR thermography (Figure 1.19 (a)) in contrast to HTWs which appeared in volatile liquids. This observation has been agreed by follow-up investigations *i.e*. Brutin *et al*. [37] and Sáenz *et al*. [126].

Deegan *et al*. [131] and Hu and Larson [104] attributed the deviation from the theoretical predictions to surface-active contaminants that aggregate on the drop surface. These contaminants are capable of supressing Marangoni effect and almost unavoidable for water, which possesses a strong attracting force due to the high polarity.

The work done by Ward and Duan [130] was successful to detect the existence of Marangoni convection by monitoring the temperature profile in the liquid phase closely to the interface, which was homogenised in a thin, *ca*. 0.1 mm below the interface due to the turbulent thermocapillary flow (Figure 1.20 (a)). They employed a stainless-steel funnel enclosed in a chamber, where water was supplied through the funnel throat to the mouth in order for the height of the surface to be kept constant (Figure 1.20 (b)). In their experiments, extreme care was taken such that water was not exposed to atmosphere after degassing and filtering, and the pressure of the chamber was reduced to ~10^{-5} Pa which might have helped minimise contamination. They also questioned the applicability of aforementioned Peason's model [109] to evaporating liquids as it did not take

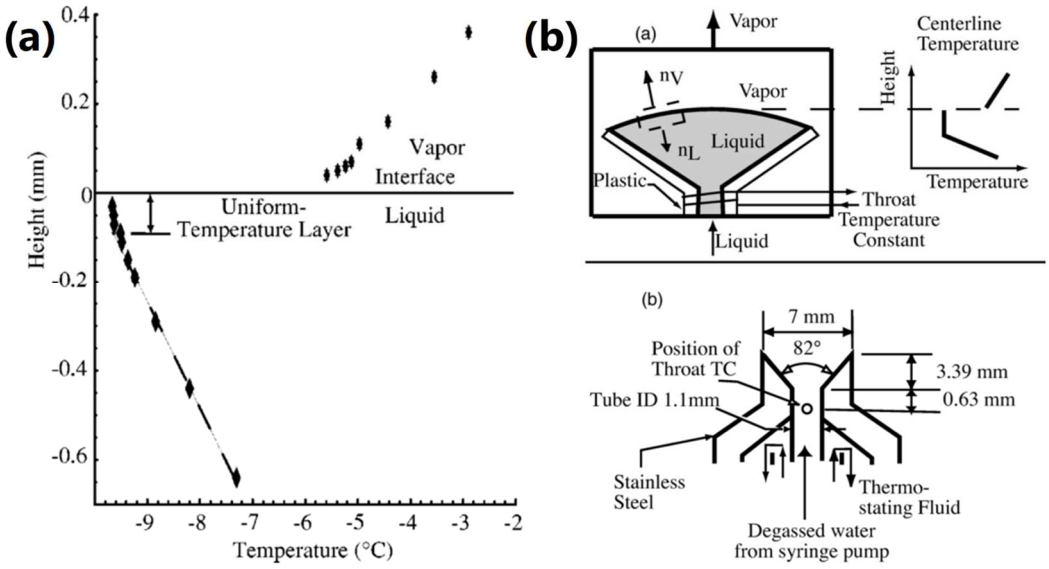

Figure 1.20 (a) Temperature profile measured across the liquid and vapour interfaces when water evaporates from (b) the stainless-steel funnel in the environmental chamber. Figure reproduced from Ward and Duan [130].

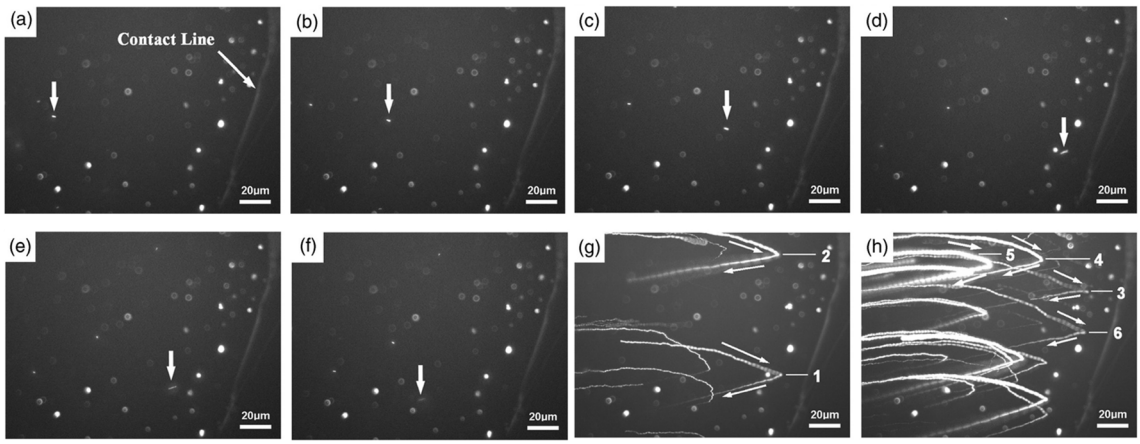

Figure 1.21 Particle motion at the edge of an evaporating water drop. The arrows in (a)–(f) indicate the different positions of a particular particle at different time: (a) 0 s, (b) 0.75 s, (c) 1.5 s, (d) 2.25 s, (e) 2.5 s and (f) 2.75 s.(g) and (h) are superimposed pictures to illustrate the streak of the particles. Figure reproduced from Xu and Luo [35].

phase change into account. Therefore, they attempted further analysis to verify the critical *Ma* (≈ 80) and demonstrated that above *Ma* ≈ 27,000 was required for water to induce the convection [36].

Xu and Luo [35] observed using a microscope fluorescent particles, which were seeded in a drying pendant drop of water, being carried by outward flow,

and then, returning along the surface (Figure 1.21). The return flow was attributed to the Marangoni stress arising from the evaporation. They implied that the suppression of the Marangoni effect in water may be caused by other factors besides surfactant contaminant.

1.3.2 Drops on wettability gradients

In addition to what happens in a liquid drop experiencing temperature gradients, and thus surface-tension gradients along the drop surface, how a drop behaves on wettability gradients has also been of great interest in scientific and industrial communities for decades. In particular, drop manipulation/transport is a critical issue in the development of microfluidic devices for bio-chemical assays [18]–[22], [132], [133], self-cleaning surfaces [134]–[137], anti-icing [138]–[142] and better heat transfer surfaces *e.g.* dropwise condensation enhancement [143]–[146], amongst others. The study on how to "*fuel*" or propel drops in such systems has been progressively active in recent years and this subsection provides an overview of the strategies that have been proposed to date. A review paper by Lach *et al*. comprehensively summarises the recent progress in this field [147].

In contrast to drop manipulation in a liquid bath, where a drop can either crawl [148], [149] or drift on a fluid current [150], [151] by chemically-/thermally-induced Marangoni effect, triggering drop motion on horizontal solid surfaces has been rather challenging due to the strong adhesion [28]. In 1989, Françoise Brochard-Wyart [38] first theoretically predicted drop motion on wettability gradients imposed by chemical or thermal gradients. She proposed the differential capillary forces acting on each side of a drop as the driving force.

Chemical gradients

In their seminal work, Chaudhury and Whitesides [39] followed Brochard's approach and fabricated surfaces with a spatial chemical gradient imposed by the silanisation process. They reported the resulting wettability gradient varying

from 97° to 25° for water over a distance of 1 cm and very low contact angle hysteresis (CAH, 6–8°). On these surfaces, water, glycerol and chloroform drops were capable of climbing up to a 15° incline (Figure 1.22 (a)).

Inspired by their work, successful experimental and theoretical achievements on motion of a drop on chemical gradients have been abundantly reported [41], [143], [146], [152], [153]. Hernández *et al*. [152] demonstrated similar motion of water and dimethyl-methylphosphonate drops on gradually oxygenated graphene (Figure 1.22 (b)). Essentially, graphene is molecularly so smooth that it should have almost zero CAH. By adding oxygen to graphene surfaces, they attained higher attraction force than bare graphene, which mainly originates in the van der Waals forces, resulting in drop motion toward the oxygen-rich graphene surface. Their experiments have been corroborated by molecular dynamics simulations performed by Liu and Xu [153].

Thermal gradients

As surface tension is dependent on temperature, Brzoska *et al*. [40] showed polydimethylsiloxane (PDMS) oil drops moving on thermal gradients of 0.35, 0.57, 0.75 and 1.0 K/mm. They prepared a very smooth, hydrophobic surface using temperature-controlled silanisation on a silicon wafer, which provided CAH of *ca*. 2°. In spite of such large temperature gradients, the drop velocities were quite slow and order of 1 mm/min.

More than two decades later, Bjelobrk *et al*. [42] recently demonstrated the remarkable enhancement of drop motion using lubricant-impregnated surfaces, which provided negligible CAH (Figure 1.22 (c)). Other techniques to boost thermocapillary drop motion have been reported by coupling chemical gradients [155] and physical vibration [156].

Electrowetting

Electrowetting has been a powerful principle that allows to actuate and switch drops on a solid surface (Figure 1.22 (d)) [154], [157], [158]. Based on the theory

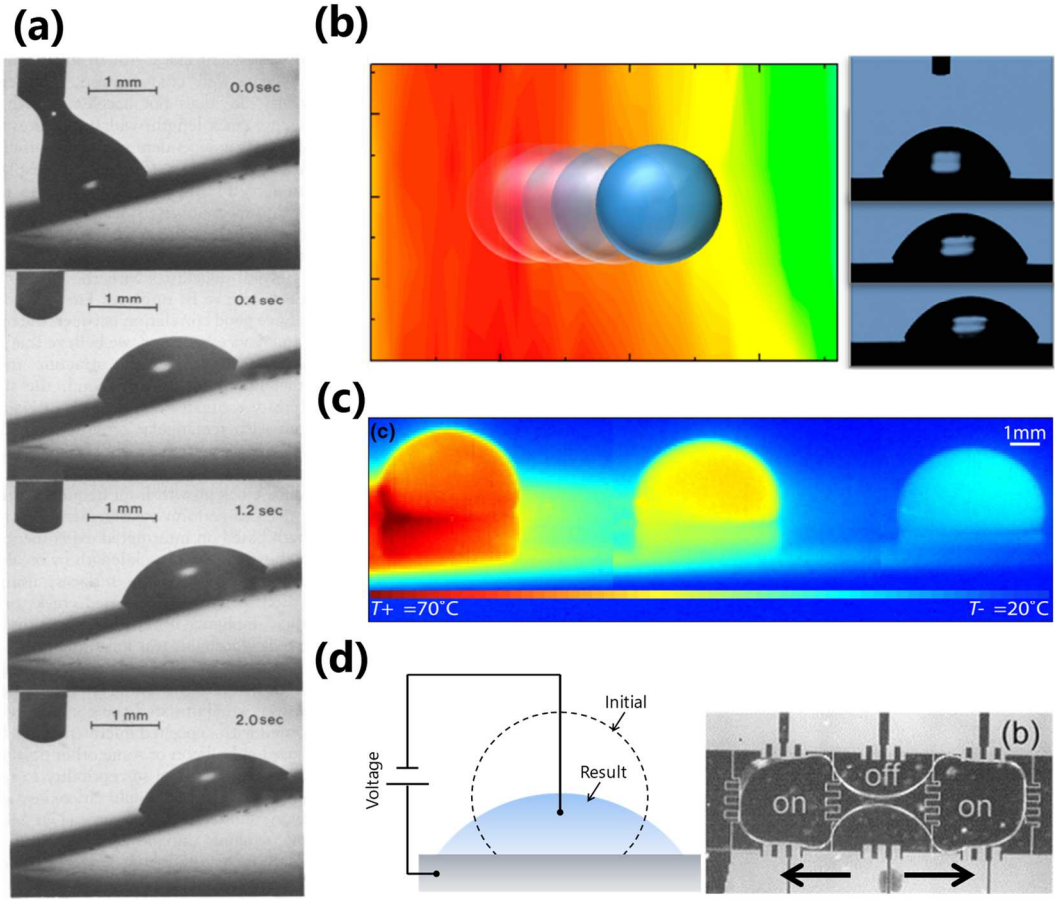

Figure 1.22 Several tactics for drop manipulation based on chemical, thermal and electrowetting principles. (a) Uphill motion of a water drop on a chemical-gradient surface [39]. (b) Colour map showing a gradient of oxygenized graphene and snapshots of actual drop motion [152]. (c) IR thermographic images showing thermocapillary-driven motion of a drop on a lubricant-impregnated surface [42]. (d) Schematic illustration of electrowetting phenomenon and its application for separation of a drop [154].

from a thermodynamic perspective, an electric field applied across a drop on a substrate is capable of modifying the interfacial tension—the Gibbs free energy, which contains both chemical and electrical components. Recently, electrowetting-based drop actuation has been applied in digital microfluidics [19], [21], [24]. However, the performance of wettability control is limited by substrate materials, type of fluids and the unrevealed contact angle saturation phenomenon.

Roughness gradients

Microtexture/pillar fabrication on solid surfaces is another promising technique which allows precise control of wettability. As introduced in subsection 1.2.2, when a liquid completely penetrates microstructures of a surface *i.e*. the Wenzel state, the apparent contact angle θ_{app} is subject to the roughness factor *r*. On the other hand, in the Cassie-Baxter (CB) state where a drop is supported on the pillars with air trapped underneath, θ_{app} can be controlled by the surface area fraction ϕ. As pointed out above the importance of CAH which can oppose any motion of drops, CB drops are generally preferred for high mobility compared with those in the Wenzel state.

Shastry *et al*. [159] were the first who experimentally demonstrated directional motion of 5 μm water drops on microstructure gradients—from the region with small ϕ to that with large ϕ. However, the motion was not spontaneous and mechanical vibration was required to drive the drop. They interpreted this by an analytical force balance calculation which accounted for CAH and estimated a slope of ϕ necessary to overcome CAH and to ensue the motion. However, they were not able to create such surfaces and to report spontaneous motion.

Reyssat *et al*. [160] also manufactured a gradient of micropillars and observed drop motion only when the substrate was vertically shaken (Figure 1.23 (a)). Along the substrate vibration, the drop itself also oscillated, experiencing wetting and dewetting events (Figure 1.23 (b)). They carefully monitored the drop shape and position, and found that the displacement took place mainly during thedewetting events as a result of asymmetric retreat of the contact line (Figure 1.23 (c)). Then, they approximated the dewetting event as a rebound of an impinging drop and derived a scaling-law model which suggested that drop velocity would increase as a function of input vibrational energy as well as micropillar gradients. Moreover, they reported that the velocity reached maximum when the substrate was shaken at the resonant frequency of the drop.

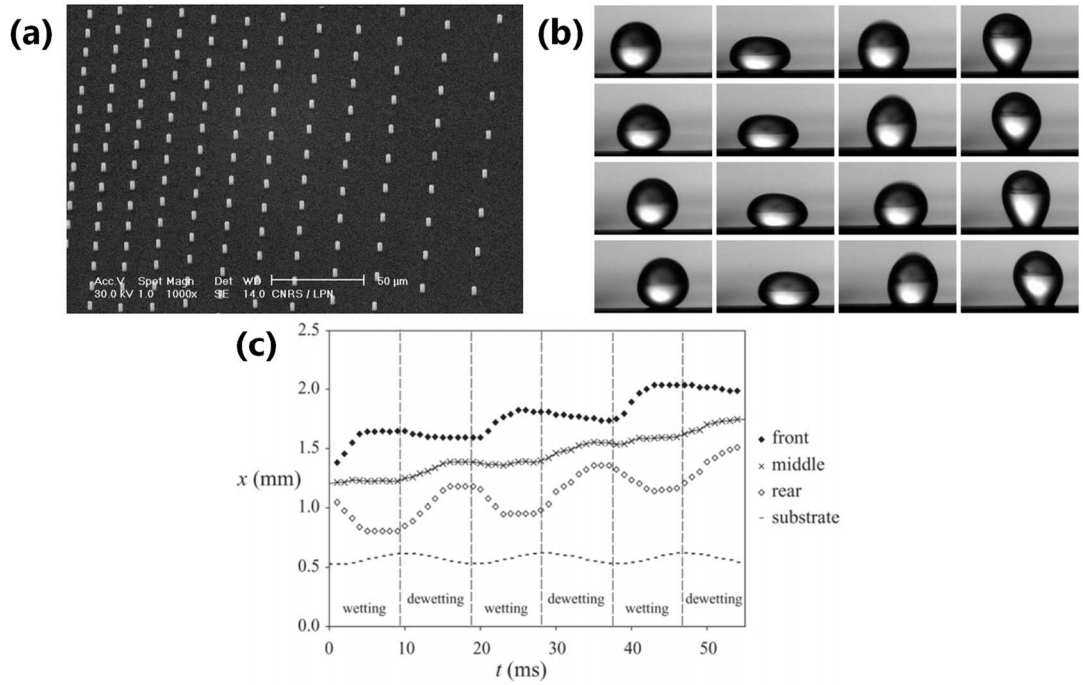

Figure 1.23 (a) Circular micropillars gradually spaced such that the slope of ϕ was 70 m^{-1}. (b) Snapshots of a water drop (R = 1 mm) moving on a vibrating micropillared surface. (c) Evolution over time of positions of the drop (front, middle, and rear) presented in (b). Both wetting and dewetting events are indicated in the graph. Figure reproduced from Reyssat *et al*. [160].

Unfortunately, they did not experimentally investigate the effect of the slope of micropillar density, neither did Shastry *et al*. [159], and the validity of their model has not been entirely confirmed.

Moradi *et al*. [161] performed a lattice Boltzmann simulation to study spontaneous drop motion induced by roughness gradients. They pointed out significant dependence of drop velocity on surface tension of the liquid as well as pillar arrangements.

1.4 Research Objectives

In the previous sections, fundamental phenomena involved in sessile drops and recent research works regarding internal flows and motion of drops have been thoroughly reviewed. It is apparent that capillary and wetting phenomena are

promising strategies to functionalise drops for drop-based applications such as microfluidic devices.

Thermocapillary or Marangoni effect often dominates fluid motion inside drops. Spontaneous onset of Marangoni convection has been observed in many liquids that are highly volatile *e.g.* alcohols, oils and refrigerants. In spite of the fact that water is the most common liquid, the existence of Marangoni flow in pure water has still been an open debate: strong fluid flows induced by thermocapillary effect have been predicted by theoretical studies whereas there has been few experimental observations in atmospheric conditions. Overall, the underpinning mechanisms of thermocapillary instabilities remains elusive.

As for drop manipulation, various drop manipulation techniques have been proposed based on introducing heterogeneous surface tension using chemical, thermal and electrical principles. However, these mechanisms might lead to undesirable side effects such as chemical compatibility, temperature change, phase change and electrical interference, which could narrow the range of practical applications. Gradients of superhydrophobic microtexture have become a rising technique for the virtue of wettability controllability. However, reported drop motion was not spontaneous and required extra forces such as mechanical vibration. Although several physical models have been proposed to predict drop mobility, no systematic analysis has been reported and its validity and limitations of the theory are questionable.

With an aim to shed light on the aforementioned problems, the present thesis firstly investigates thermocapillary/Marangoni instabilities in pure water drops and explores a way to manipulate the flow using localised heating. Localised heating should be capable of imposing distinct and significant thermal gradients in contrast to isothermal or uniform heating situations as in the previous works. To this end, a laser is used to heat a water drop locally at two locations of interest: the centre and the edge. A systematic analysis of the influence of heating power

is carried out to establish the criterion for the onset of Marangoni flows. Moreover, the contribution of local heating to drop evaporation is also discussed.

Secondly, this thesis addresses drop mobility on wettability contrasts imposed by superhydrophobic microtexture patterns. In contrast to a "wettability gradient", the term "wettability contrast" in this thesis refers to the boundary/ interface between two surfaces with different associated wettabilities. Focusing on the incipience of drop motion, the effects of differential surface area fractions and pinning forces on drop velocity are systematically investigated. Finally, this thesis attempts to describe how surface free energy is converted into kinetic energy and how the drop is directed from a thermodynamics perspective.

Contributions made in this thesis are believed to illustrate the long-standing question about Marangoni convection in water as well as a universal mechanism underpinning drop motion, both of which will eventually inform the design of functional drops and surfaces used in applications such as bio-sensing microfluidics.

1.5 Thesis Organisation

This thesis is organised into four chapters. Following the first introductory chapter, Chapters 2 and 3 guide the reader into the investigation part wherein the experiments, results and discussion are presented. Finally, main conclusions are summarised in Chapter 4.

Chapter 1 has covered an introduction to drops/droplets as a scientific field of study with a brief overview of research history. Then, this chapter has provided basic knowledge of physics involved in drops, such as wetting and phase change, to ease the reader into what is discussed in the rest of the thesis. Literature review has been also included in this chapter to illustrate the recent progress in the fields of hydrodynamics inside a drop and wettability modification for drop actuation. Having established current scientific challenges and needs for practical

applications involving drops, the objective of the present study has been identified. In addition, this chapter has included a quick guidance of each chapter composing the present thesis.

Chapter 2 reports the first observation/visualisation of thermocapillary or Marangoni convection in pure water using infrared thermography and particle imaging. Strong recirculating vortices are observed when the centre of the drop base is heated locally using a laser. Marangoni-origin instabilities are proved by dimensionless number criteria and supplemental experiments under inverted gravity. Following the novel finding above, this chapter further explores a way to manipulate the flow using the local heating method. In particular, the influence of heating location and power on the convection is investigated. Additionally, the effect of local heating on evaporative kinetics is briefly discussed.

Chapter 3, on the other hand, focuses on what happens to a drop placed on a wettability contrast. A systematic analysis is performed using a number of combinations of surfaces with distinct microtexture patterns, which realise a variety of wettability. Special attention is paid to the rapid motion of triple-phase contact lines with high-speed imaging and subsequent image analysis. The criteria of drop motion and the effect of contact angle hysteresis are addressed by the surface free energy analysis.

To conclude what is found in each chapter above, Chapter 4 remarks the contributions to the field of the subject, potential applications using the findings and suggested future work to cover open questions raised by the present work.

Chapter 2

Thermocapillary Instabilities in Pure Water Drops

There is abundant experimental [31]–[33], [37], [110], [117]–[119], [121] and theoretical [72], [104], [116], [122]–[127] evidence of vigorous convective flows driven by thermocapillary effect in evaporating drops of many liquids *e.g.* organic fluids and oils. However, in case of water, the existence of Marangoni convection has still been controversial [128].

This chapter reports the first direct observation/visualisation of Marangoni- or thermocapillary-driven flows in pure water drops via infrared (IR) thermography coupled with particle imaging using a visual CCD camera. A temperature gradient that drives the flows is imposed on the drop by locally heating the substrate directly below the centre with a laser. Upon heating, twin counter-rotating vortices appear which eventually shift to an oscillatory emerging/splitting behaviour. Origin of the instabilities is identified by evaluating the dimensionless Marangoni and Rayleigh numbers, which is further supported by a second set of experiment with an inverted system.

Having proven the emergence of Marangoni flows in pure water, the rest of this chapter is devoted to a systematic analysis of the effect of local heating on the internal flows and evaporation of drops. In particular, experiments are designed to investigate how heating the centre or the edge of a pure water drop using a laser with three different levels of irradiation power affects the emerging Marangoni instabilities and the evaporation kinetics such as evaporation rate and triple-phase contact line behaviour.

The experiments and analysis presented in this chapter are also reported in Kita *et al*. [162] and [163].

2.1 Experimental Methodology

Experiments are designed to provide a drop with local heating and to observe its thermal activities and evaporative behaviour. To this end, experimental setup, depicted in Figure 2.1 (a) and (b), consists of an IR camera (FLIR SC-4000 with spectral range from 3.0 to 5.0 μm, temperature resolution of 18 mK) and a charge-coupled device (CCD) visual camera (Sentech STC-MC152USB with a Cosmicar TV Zoom lens and a 30 mm spacing ring). Following subsections describe the experimental procedures as well as the important techniques for the experiments such as infrared thermography

2.1.1 Procedures

A 10 μL drops of deionised water is gently deposited on a substrate using a micropipette and simultaneously recorded by the CCD camera from the side and by the IR camera from the top. The substrate is a 10 × 10 mm^2 copper plate with 50 μm thickness allowing a well-defined and fixed heating pattern, which is coated with a very thin (~20 nm) layer of CYTOP (a fluoropolymer composed of C-C, C-F and C-O bonds, purchased from AGC) in order to control the drop shape.

The drop is heated locally, through the substrate, under its centre or edge via a continuous diode laser (Integra-MP-30WW, Spectra-Physics, with 808 nm wavelength) as shown in Figure 2.1 (c). The substrate is mounted on a two-axis horizontal translation stage allowing to locate the hot spot to a desired position. Laser power is variable and set to be 3.4 W (high), 1.9 W(middle) and 0.3 W (low), as measured with a laser power meter (Vega, Ophir Optronics Solutions Ltd).

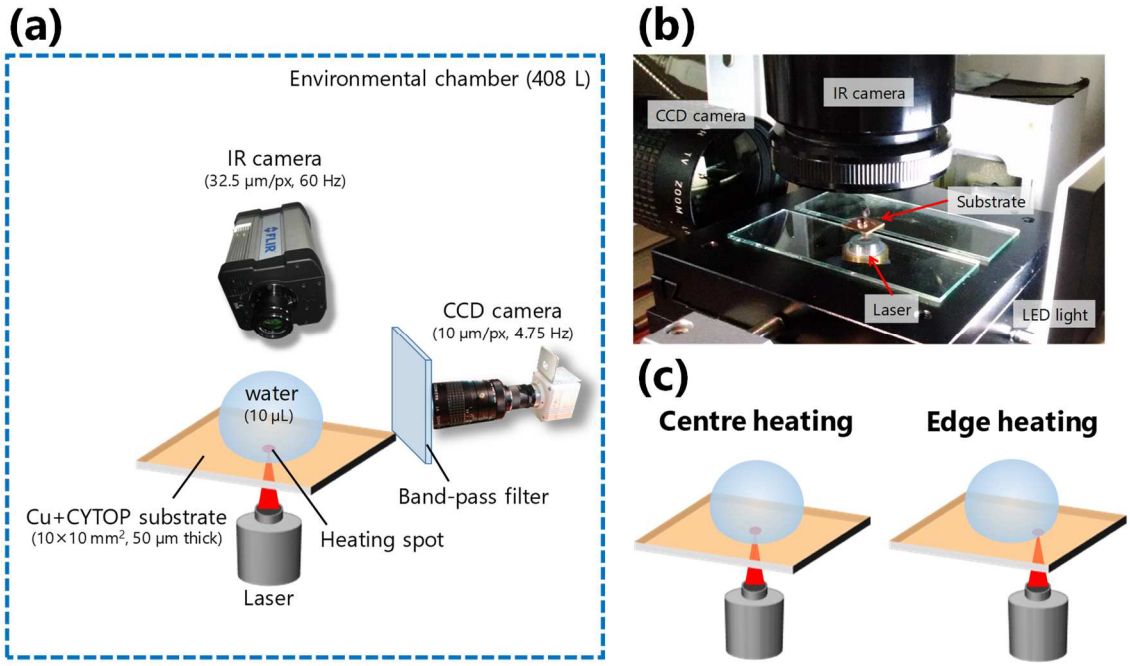

Figure 2.1 (a) Schematic illustration and (b) photograph of the experimental setup. (c) Heating locations of interest (centre and edge).

As soon as laser irradiation begins, the thermal activities of the drops are captured with the top-view IR camera at frequencies of 5, 30 and 60 Hz for each irradiation power (low, middle and high, respectively). Simultaneously, evaporative behaviour of the drop is monitored by the side-view visual CCD camera at 4.75 Hz. IR and CCD images are subsequently processed to extract the temporal temperature maps and drop profiles (contact angle, radius and volume) using custom-built Matlab code. All the experiments are performed in an environmental chamber (PR-3KT, ESPEC Corp) where temperature and relative humidity are kept at 18.0 ± 0.5 °C and 40 ± 10 %, respectively, to minimise the influence of the change in ambient conditions. Experiments for each laser power and heating location are repeated at least 10 times and showed good reproducibility.

2.1.2 Infrared thermography

Infrared thermography is a powerful technique to obtain spatio-temporal temperature maps of an object. An IR camera displays temperature calculated based on infrared energy emitted, transmitted and reflected from the object to the sensor. In contrast to ideal black body radiation, which is only a function of temperature and wave length *i.e*. Planck's law, the energy flux that the IR camera receives from the real object should be a product of the black body radiation and the optical properties (emissivity, transmissivity and reflectivity). Therefore, it is paramount for a precise temperature measurement to account for the infrared characteristics of the system. Essentially, an object with a high emissivity (close to black bodies) has a low transmissivity and reflectivity, and hence, is easy to measure the precise surface temperature.

In the present experiment, a high contrast in the emissivities for water and polished copper, which are 0.96 and 0.03, respectively, results in a sharply defined edge of the drop. Moreover, such high emissivity of water allows the IR camera to capture very accurate interfacial temperature of the drop. In fact, more than 90% of the radiation that reached to the sensor of camera should be emitted from a thin layer beneath the drop surface of 10 μm.

2.1.3 Heating profiles

Figure 2.2 shows the sequential images of the imposed temperature distribution on the substrate during laser irradiation at each power. The substrate surface presented in Figure 2.2 is painted in black for the sake of a high emissivity. The temperature profiles along the dashed lines A–B are also plotted above each IR images. A dashed circle in the top-left panel of Figure 2.2 represents the typical drop circumference for comparison. How the heating profile is localised can be quantified by estimating the full width at half maximum (FWHM), which is often defined as a spot diameter of a Gaussian laser beam, of the temperature peak.

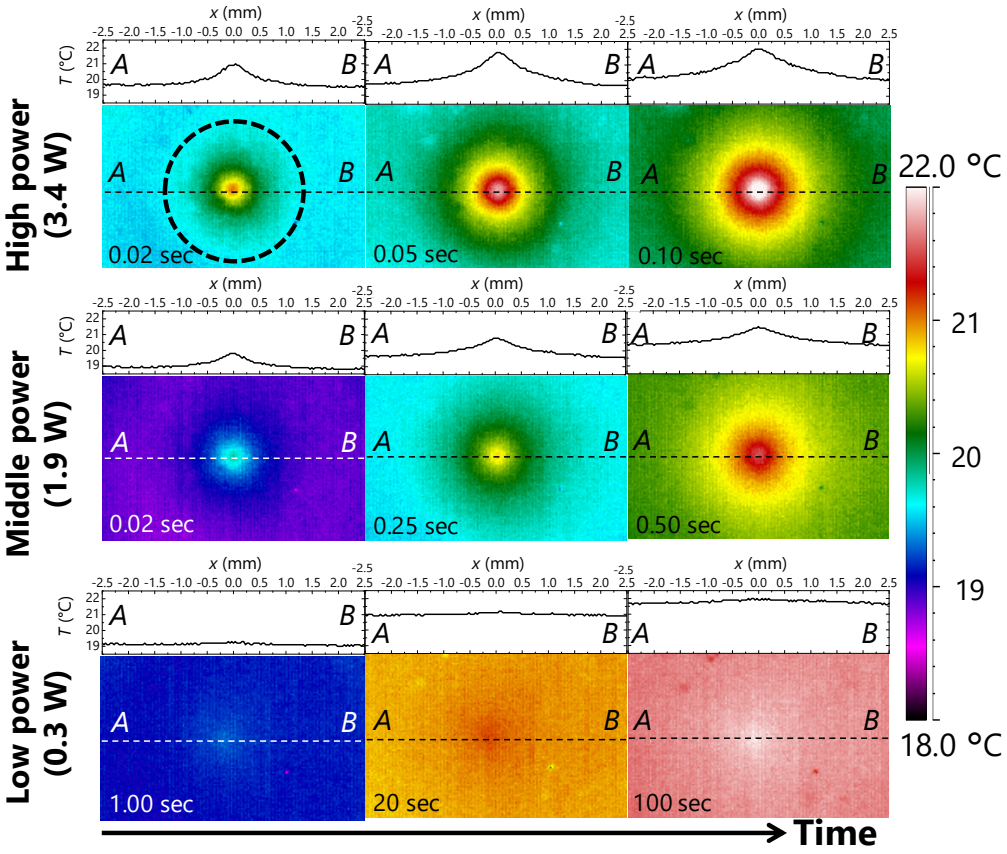

Figure 2.2 Sequential IR snapshots showing evolution over time (from left to right) of the temperature distribution on the substrate surface without a drop imposed via laser irradiation at high (3.4 W, top), middle (1.9 W, middle) and low (0.3 W, bottom) power. Temperatures along the dashed lines A–B are plotted above each images. Dashed circle in the top-left panel indicates the typical base circumference of a 10 μL drop.

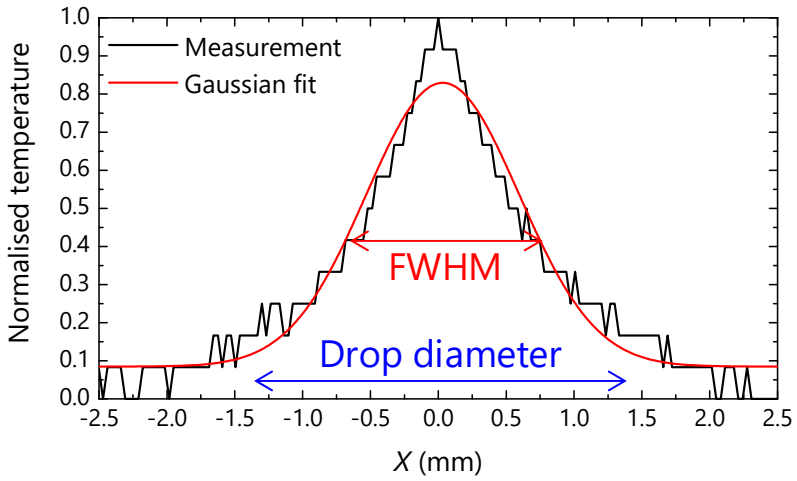

Figure 2.3 Normalised temperature profile on the surface at 0.50 sec for the middle-power heating case extracted from the IR camera (black) and its Gaussian-fitted curve. Red and blue arrows indicate the full width at half maximum (FWHM) and the typical drop base diameter, respectively.

Normalised temperature profile at 0.50 sec during middle-power heating extracted from the measurement (black line) and its Gaussian-fitted curve (red line) are plotted in Figure 2.3 with FWHM and the initial drop diameter indicated with red and blue arrows, respectively. It is readily apparent that the local heating areas defined by FWHM are approximately 20–25% of the drop base area for the middle- and high-power cases. On the other hand, no satisfactory sharp peak of temperature for the accurate Gausian-curve fitting is detectable for the low-heating power. Nevertheless, a slight radial temperature gradient spreading from the laser spot can be seen in the IR images in Figure 2.2.

2.2 Induction of Internal Flows of Drops

In the following two sections, let us first focus on the onset of convective flows in water drops under local heating by looking at the representative case of centre heating at the middle power.

2.2.1 Emergence of twin vortices

The thermal activities at the liquid-vapour interface of a freely evaporating pure water drop has been reported to be comparatively weak, due to an almost uniform spatial temperature distribution [33], [122], [164]. Indeed, the experimental observation corroborates the uniform thermal distribution, as shown in the IR thermography image in Figure 2.4 (a) of a freely evaporating water drop captured from above. A dot with a lower temperature is due to the reflection of the camera and is hence neglected.

Upon locally heating the substrate directly below the centre, a temperature gradient in the form of a concentric ring is induced between the apex and the edge of the drop, as shown in Figure 2.4 (b). This temperature gradient can be attributed to heat transfer from the substrate to the drop and eventually to the liquid-air interface. Notably, lateral heat conduction within the substrate is

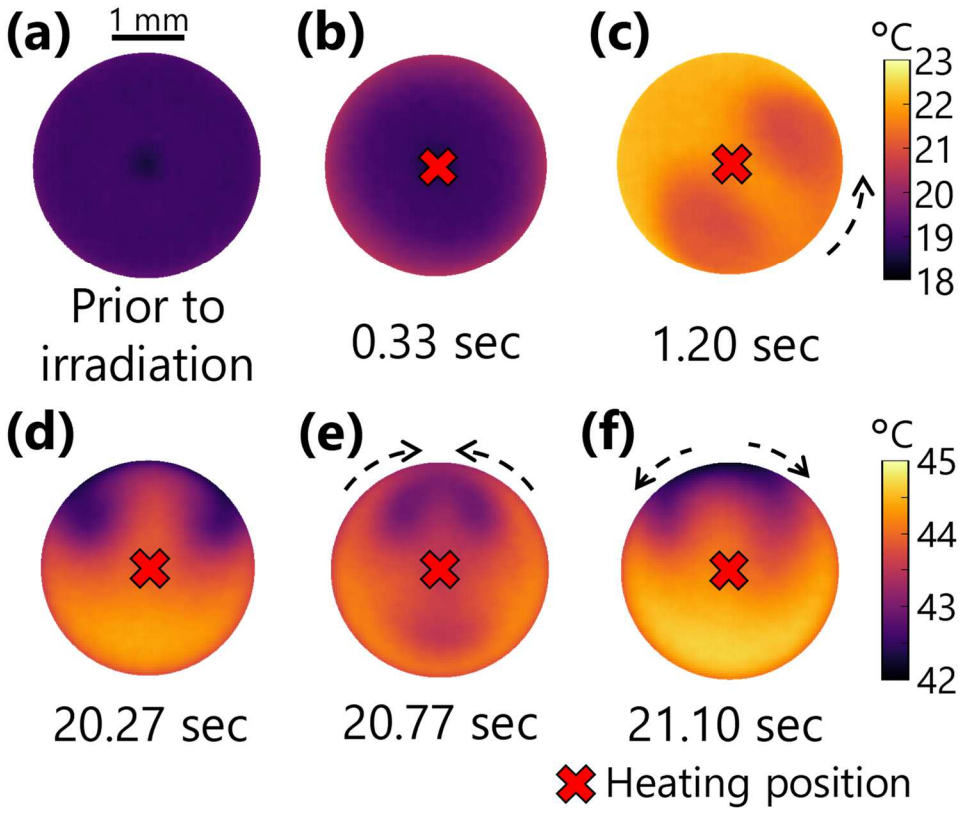

Figure 2.4 Representative temperature maps of a pure water drop viewed from above via the IR camera (a) prior to heating and (b)–(f) heating at the centre. Red crosses denote the location of the heating spot. Arrows show the motion of the vortices.

minimal due to its thickness (50 μm), which is verified in Figure 2.2. At the contact line, the liquid layer is much thinner and is heated faster, giving rise to the hotter exterior ring. The longer the path the heat has to travel, the cooler the interface should be, giving rise to a cooler drop apex. Evaporative cooling should be considered fundamental to the evaporation process [105]. However, this effect is overcome by substrate heating, leading to the ring in Figure 2.4 (b) similar to the previous reports [105], [126], [164].

As the convective flows set in, the temperature distribution becomes irregular and a pair of counter-rotating vortices emerge that start travelling azimuthally, as can be seen in Figure 2.4 (c). The arrow in panel (c) presents the direction of the motion of the vortices pair, not of the liquid. Ultimately, the twin vortices

begin to sequentially merge and split (Figure 2.4 (d)–(f)) in an oscillatory manner. After *ca*. 30 sec, the thermal patterns become chaotic which is beyond the scope of this work and therefore they are not discussed in this study.

To better understand the liquid flow within the drop and the oscillatory merging and splitting behaviour of the vortices, a water drop seeded with 0.01% w/w tracer particles (Vanadyl 2, 11, 20, 29-tetra-tert-butyl-2, 3-naphthalocyanine, Sigma Aldrich) is followed with the CCD camera mounted with a 5× magnification, self-illuminating microscope objective. Care is taken for the particles to have a minimal effect on both flow patterns and the evaporation process. Representative snapshots are shown in Figure 2.5, corresponding to Figure 2.4. Notably, the edge of the drop appears brighter than the rest and a bright ring can be seen at the centre of the drop, due to lens lighting and substrate reflectance.

Initially, Figure 2.5 (a), the particles are almost stationary in the absence of a strong current at the top of the drop (where the camera is focused), which corroborates the previous reports [31], [33], [34] and Figure 2.4 (a). Upon laser irradiation, Figure 2.5 (b), the particles start moving from the hot periphery to the cold apex (as shown in Figure 2.4 (b)) due to the onset of convective flows. As the convective flows set in and given the fact that the liquid-air interface is acting as a boundary/wall to the flow, the liquid recirculates along the periphery forming the observed counter rotating vortices, which is presented in Figure 2.5 (c) with arrows highlighting the liquid flow. The vortices recirculate the liquid (Figure 2.5 (d)) and the convective flows diminish resulting in the merging of the vortices (Figure 2.5 (e)). However, laser irradiation continues to heat the drop leading to stronger convective flows and vortices split again in order to compensate (Figure 2.5 (f)). As both fluid recirculation and heating persist, the vortices merge and split in an oscillating manner in an attempt for the drop to attain thermal equilibrium.

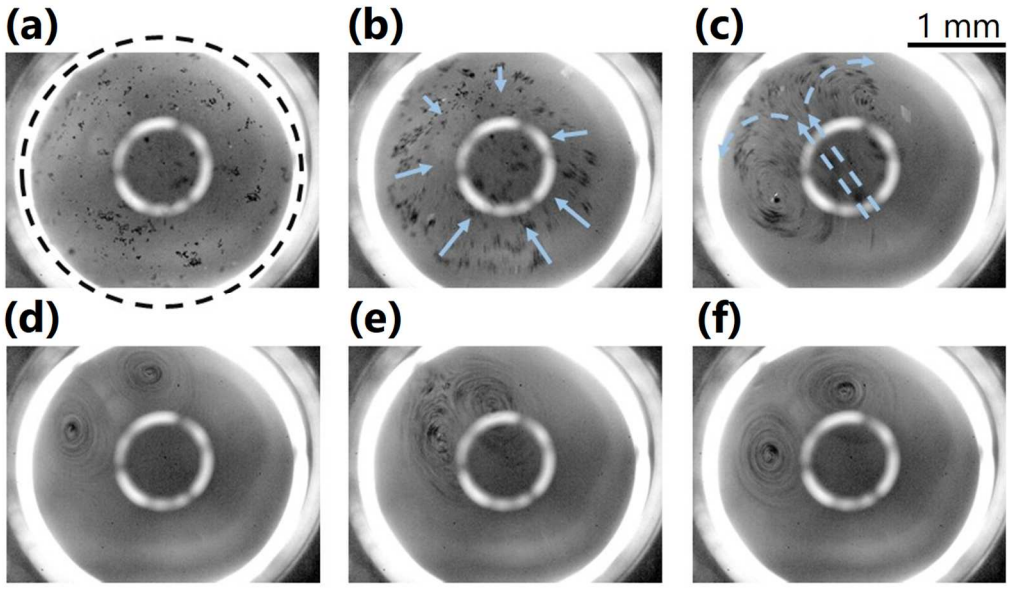

Figure 2.5 Top-view sequential snapshots corresponding to the panels in Figure 2.4 of a water drop containing 0.01% w/w tracer particles. Dashed circle in panel (a) shows the periphery of the drop and arrows in (b) and (c) denote liquid flow. Panels (d)–(f) present the emerging/splitting behaviour of the drop. The bright ring in the centre is a reflection of the light source embedded in the lens.

2.2.2 Evolution of instability

Drops that are progressively away from thermodynamic equilibrium *i.e.* inhomogeneous temperature gradients will recirculate the liquid in order to reach the equilibrium state. Such non-equilibrium states can be attained by some imposed constraint such as heating. The previous section demonstrates induction of flows in a pure water drop when heating it locally with laser irradiation. As the laser heating continues, however, the system will no longer be capable of dissipating the thermal gradient leading to more complex, oscillatory behaviour as presented in Figure 2.4 and Figure 2.5.

Further analysis of the thermographic data allows the depiction in Figure 2.6 of the interfacial temperature difference, $\Delta T = T_{max} - T_{min}$, where T_{max} and T_{min} are the maximum and minimum temperatures at the liquid-air interface of the drop,

respectively and are extracted from the IR images. Initially, the drop is freely drying on the substrate and ΔT is virtually 0 K. Consequent to heating, the temperature gradients appear in the form of concentric rings leading to a sharp increase in ΔT. The onset of the twin vortices coincides with the peak of ΔT (~ 2.25 K). At this point, ΔT plunges as fluid vortices attempt to restore thermal equilibrium to the system. However, uniform thermal distribution cannot be achieved due to the heat being continuously imposed to the drop and hence ΔT increases. Once ΔT reaches *ca*. 1.3 K, the twin vortices begin to travel azimuthally. At *ca*. 10 sec, a small fluctuation in ΔT appears that gradually becomes more prominent as its amplitude increases. A shift to the next stage of instabilities is readily apparent at *ca*. 20 sec after which ΔT fluctuates more significantly around 1.25 K. This oscillation could be attributed to the observed sequential merging (valleys) and splitting (peaks) of the vortices. Essentially, every time the vortices merge, the fluid recirculation slows down giving rise to a rapid ΔT increase that in turn results in splitting the vortices to recirculate the liquid. A fast Fourier transform (FFT) is performed in order to reveal the oscillatory characteristics of ΔT between 20–30 sec in Figure 2.6 and provides a power spectrum as presented in Figure 2.7. It is readily apparent that the dominant frequency appears to be the first one at 1.05 Hz and is followed by two minor ones at approximately 2.09 and 2.27 Hz. The major oscillation at 1.05 Hz corresponds to the merging/splitting events of the vortices whereas the minor frequencies could perhaps be attributed to minute temperature instabilities at the drop interface.

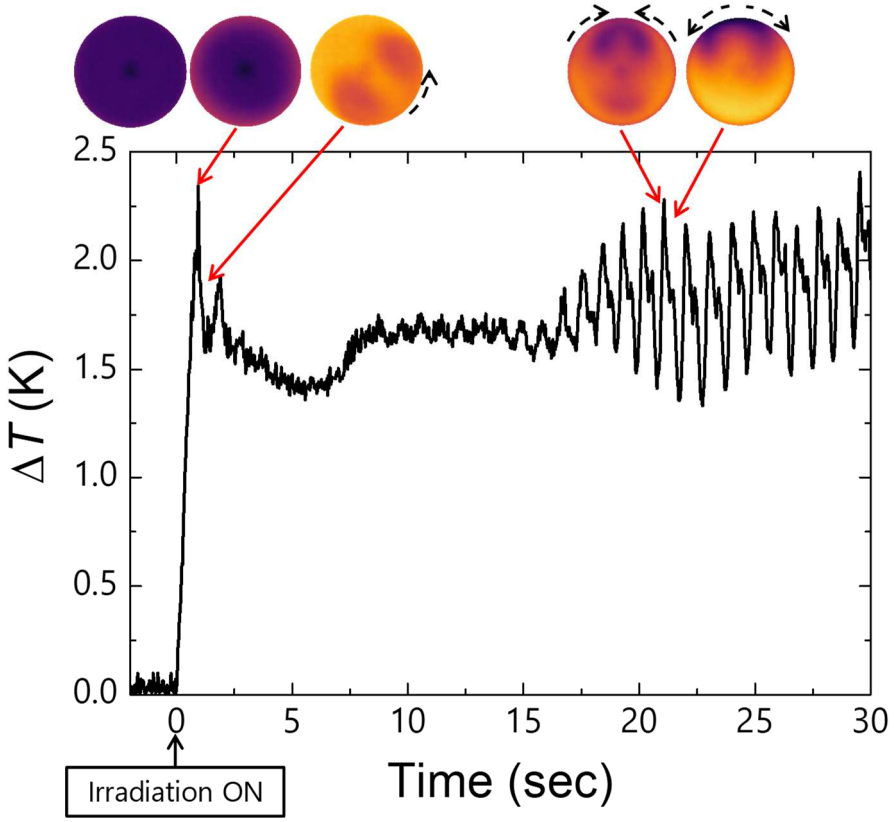

Figure 2.6 Evolution over time of interfacial temperature difference, ΔT. Insets show the corresponding IR images with red arrows pointing at incident ΔT.

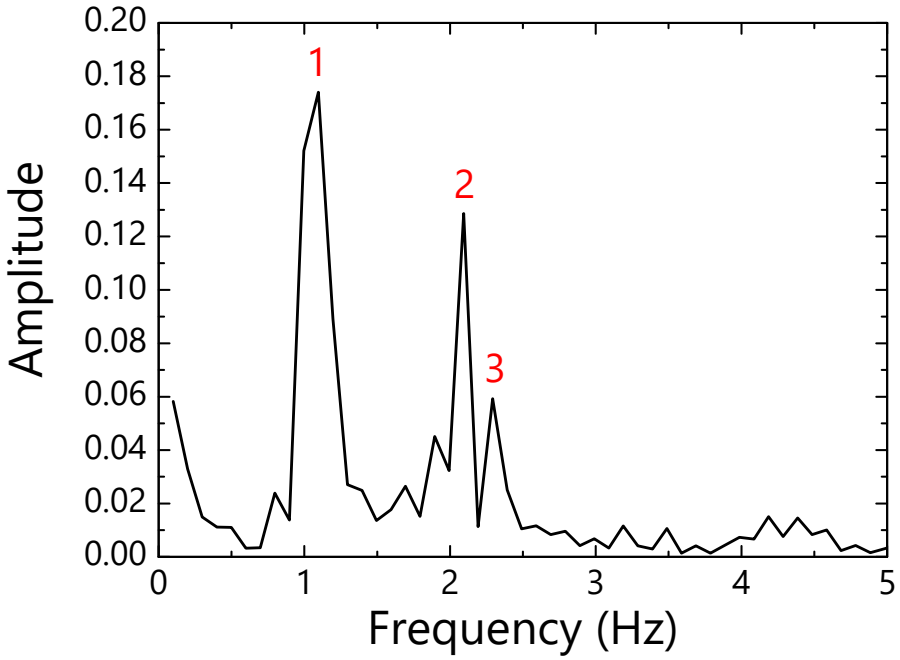

Figure 2.7 Power spectrum calculated by FFT analysis of oscillatory ΔT.

2.3 Origin of the Vortices

2.3.1 Dimensionless numbers

Let us now attempt to elucidate the origin of the thermal patterns or recirculating flows in Figure 2.4 and Figure 2.5, which are essentially convective, either buoyancy (natural convection) or surface tension (thermocapillary or Marangoni convection). Revisiting subsection 1.3.1, non-dimensional numbers such as the Rayleigh number *Ra* and the Marangoni one *Ma* are often used as the criteria to determine which is dominant, and can respectively be expressed as (identical to Eq. (1.11) and (1.12))

$$Ra = \frac{\beta g H^4 \Delta T}{\nu \alpha R}\ , \tag{2.1}$$

$$Ma = -\frac{\partial \sigma_{LV}}{\partial T}\frac{H^2 \Delta T}{\rho \nu \alpha R}\ . \tag{2.2}$$

Typical values of the thermophysical properties of distilled water (at 20 °C and 1 atm), which appear in Eq. (2.1) and (2.2), are listed in Table 2.1.

Ra and *Ma* are calculated using values of H, R and ΔT extracted by the CCD and IR cameras, respectively. *Ma* is found to vary around 4.0×10^3 in accordance with the previously reported cases of Marangoni-driven HTWs in organic liquids [33], [37], whereas *Ra* is calculated to be below 500 throughout the observation. Determining the dynamic Bond number, defined as the ratio of buoyancy to surface tension, $Bd = Ra/Ma$, leads to $Bd \ll 1$ [33], [37], [115], [117], [165]. Combining this result with the fact that the critical *Ra* value for the onset of natural convection is typically in the order of 10^3 [165], [166], which is almost twice the value estimated above, allows us to claim that the observed thermal patterns are a manifestation of Marangoni (or thermocapillary) convection. In fact, it is readily apparent from Eq. (2.1) and (2.2) that *Bd* is independent of ΔT and determined only by the physical properties and the geometries of the drop,

Table 2.1 Thermophysical properties of water at 20 °C and 1 atm [167].

α (mm^2/s)	β (1/K)	ν (mm^2/s)	ρ (kg/m^3)	σ_{LV} (mN/m)	$-(\partial\sigma_{LV}/\partial T)$ (N/(m·K))
0.143	2.09×10^{-4}	1.004	998	72.74	1.51×10^{-4}

which implies that the fluid dynamics in such drops used in this study should essentially be surface-tension dominant. Moreover, Ma ~ 5500 is required for Marangoni flow to set in and $Ma > 3000$ to maintain it.

2.3.2 Characteristic frequency

Once an instability in the drop sets in, it will develop if $Ma \gg 1$ as the de-stabilising (surface-tension gradient) effect overcomes the stabilising effects such as thermal and viscous dissipation [165]. Therefore, the oscillation of ΔT at frequencies presented in Figure 2.7 should be related to the thermocapillary time scale which can be defined as $\tau_{Ma} = \left[\rho RH^2 / \left(\frac{\partial \sigma_{LV}}{\partial T}\Delta T\right)\right]^{1/2}$. Hence the characteristic Marangoni frequency is simply given by $f_{Ma} = 1/\tau_{Ma}$ and is calculated to be approximately 8 Hz, which is in the same order of magnitude as the values reported in Figure 2.7.

2.3.3 Effect of gravity orientation

In addition, the claim for the Marangoni dominance over the flows observed is further pursued experimentally with the heating of a pendant drop, using the inverted setup shown in Figure 2.8 (a). Essentially, gravity, the main component of natural convection as described in Eq. (2.1), should be inverted in a pendant drop. Evidently, the thermal activities in Figure 2.8 (b)–(g) are similar to those in Figure 2.4. Analysis of ΔT and the dimensionless Ma, Ra showed similar oscillations appearing slightly sooner possibly due to the inverted action of gravity, which essentially contributes to the interfacial flows. Nonetheless,

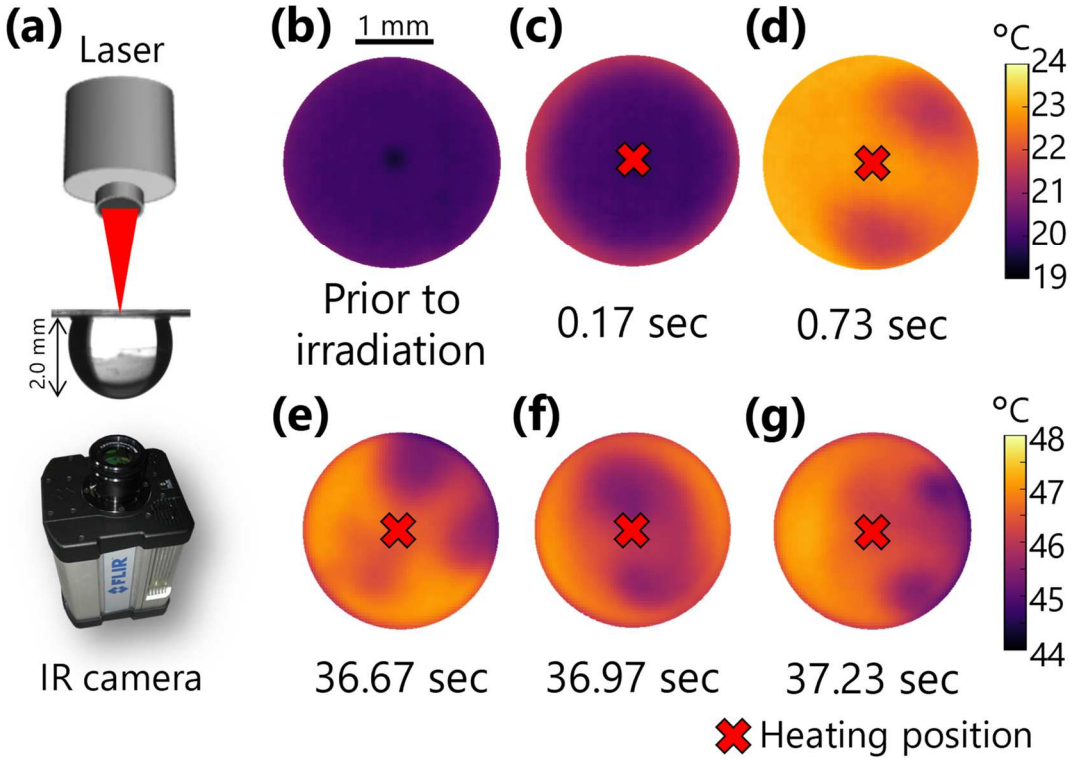

Figure 2.8 (a) Inverted experimental setup. (b)–(g) Evolution over time of the interfacial thermal patterns in the water drop induced by localised heating.

the Marangoni convection is still dominant.

2.4 Influence of Local Heating on Flows and Evaporation of Drops

Now that the existence of Marangoni or thermocapillary convection in pure water drops has been evidenced in the previous section, this section is devoted to a systematic analysis of the effect of local heating on the internal flows and evaporation of drops.

2.4.1 Influence of heating power and location on flows

This section presents how the thermal patterns at the drop surface evolve depending on heating locations and laser power.

Influence of laser power

Let us first focus on the effect of heating power on the thermal behaviour of the drops when heated directly below the centre. The IR thermography images in Figure 2.9 depict the spatiotemporal thermal distributions arising within the drops during centre heating at different irradiation powers (increasing from left to right). Temperature of the drop surface is found to reach approximately 30–80 °C depending on irradiation power (higher power leads to higher temperature, and vice versa).

Four stages of the thermal activities are distinguishable from the IR images for better understanding. Prior to irradiation, denoted as stage 1, every drop is freely evaporating without heating and the IR images exhibit a uniform temperature distribution, in agreement with the previous section. Heating is initiated in stage 2, where a ring-like hot region at the periphery of the drop arises due to heat transfer from the substrate to the liquid–air interface of the drop. Recirculating flows then set in, manifesting as twin counter-rotating vortices (stage 3). As described in subsection 2.2.2, the vortices are formed essentially when heat from the laser spot travels within the drop until arriving at the liquid–air interface, at which point the flow recirculates to the centre in an attempt for the system to attain thermal equilibrium. Eventually, each drop shifts to stage 4, during which the thermal activities become highly irregular, leading to distinct thermal patterns. In the low-power case (0.3 W), the recirculating front moves azimuthally along the drop periphery. The recirculating vortices for the middle-power case (1.9 W) initially displays a similar azimuthal motion, and then, the pair of vortices begins an oscillatory merging and splitting behaviour as revealed in the previous section. On the other hand, the high-power case (3.4 W) exhibits the merging/splitting motion of the vortices as seen in the middle-power case, but also a periodic traveling of the recirculating front from one side of the drop to the other. As the flows set in, this periodic shift of the recirculating front could

be attributed to a temperature gradient this time over the two hemispheres of the drop. As can be seen in the IR images, the temperature difference between the two hemispheres increases during heating and leads to a large surface tension gradient capable of dragging the front. This fact is further supported by the calculation of the time scale of the phenomenon in the following section about the temperature-gradient oscillations.

Influence of heating location

In addition to heating power, the effect of the location of the heating spot on the emerging thermal patterns is investigated. To this end, one side of the edge of each drop is heated locally, as presented in Figure 2.10, with increasing irradiation power from left to right. In this case, stage 1 corresponds to no heating, which is readily apparent given the uniform thermal distribution in all cases. Stage 2 corresponds to the onset of irradiation, which can be identified as the hotter region to the right of each image. As temperature gradients increase, convective flows appear and manifest in vortices (stage 3) with their strength in accordance with heating power. Notably, the low-power heating shown in the first column is insufficient to drive vortices, and the thermal motion in this case progresses in the same manner. By contrast, for the other two cases *i.e*. middle- and high-power, twin-vortical thermal patterns are clearly observable and they form such that the drop can be separated into two hemispheres defined by the dashed lines from the heating spot to the other side. As heating continues, the vortices become unstable, entering stage 4 during which they remain at the same location, however, their strength begins to fluctuate. In particular, the strength of one vortex increases while simultaneously the other one decreases in a sequential manner. This leads to an oscillation of the flow around the main heat conduction path (dashed lines in Figure 2.10). This oscillation could be attributed to a growth of perturbation which could perhaps be due to a surface defect interfering with heat conduction or a small, undetectable asymmetry in drop shape.

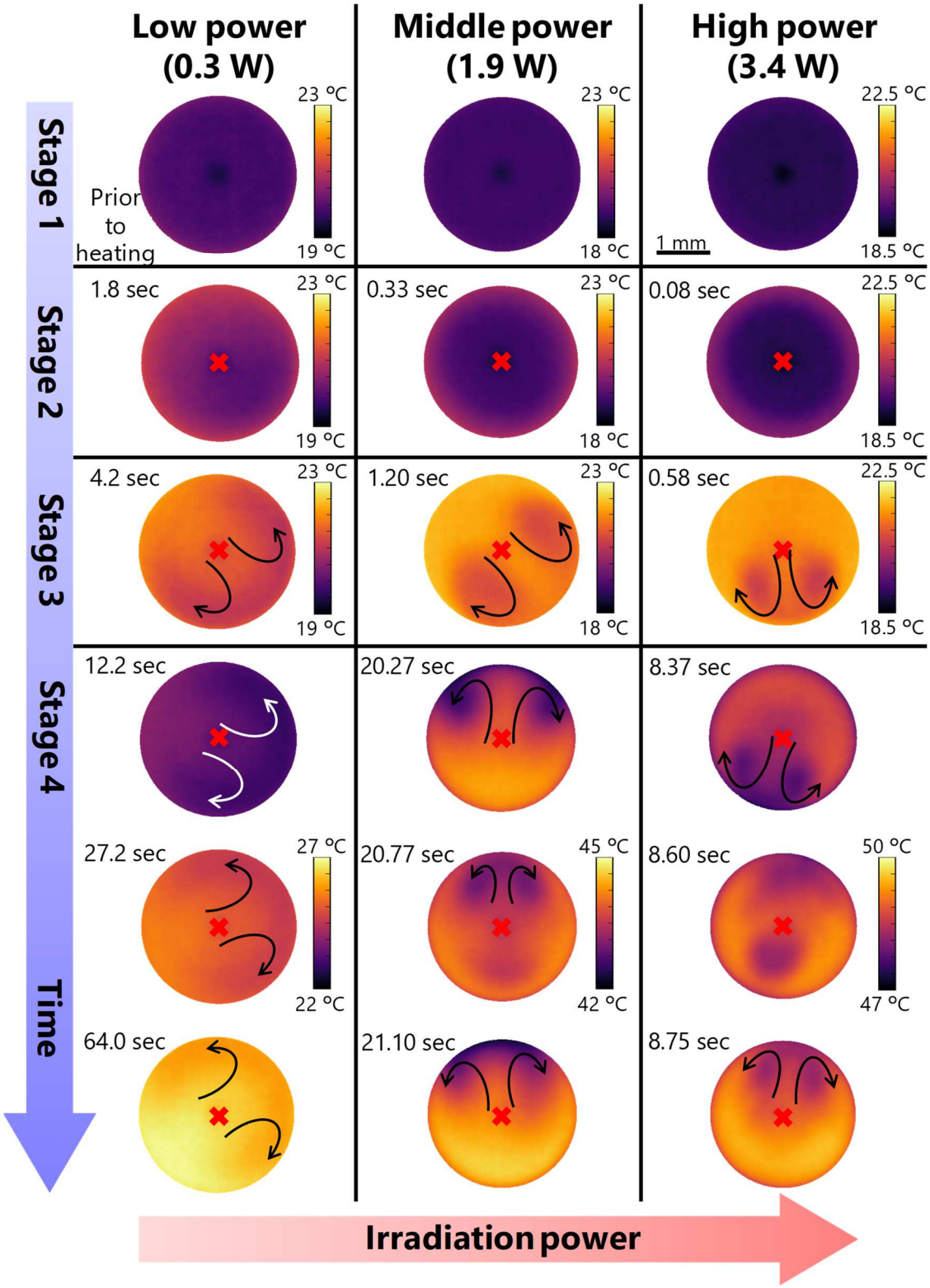

Figure 2.9 IR thermographic images of pure water drops viewed from above, showing the emergence and evolution of the thermal patterns during centre heating. Crosses denote the location of the heating spot. Arrows show the motion of the vortices.

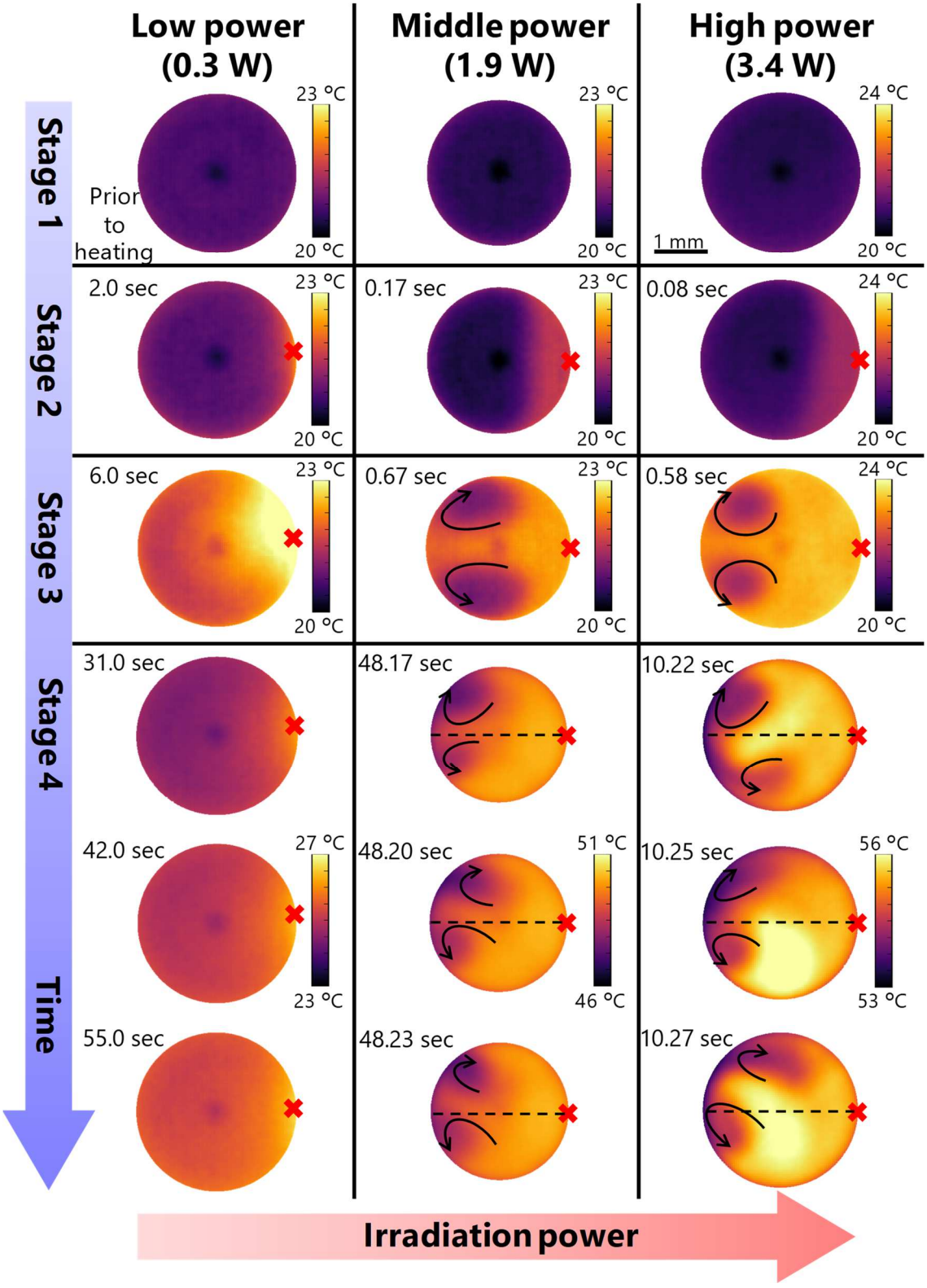

Figure 2.10 IR thermographic images of pure water drops viewed from above, showing the emergence and evolution of the thermal patterns during edge heating. Crosses denote the location of the heating spot. Arrows show the motion of the vortices. Dashed lines indicate the main heat conduction path.

2.4.2 Thermal-gradient variations within the drops

Evolution of ΔT

In a similar fashion to subsection 2.2.2, further detailed analysis of the thermal images is performed and allows to plot, in the left column of Figure 2.11, the temporal evolution of the interfacial temperature difference ΔT for 60 seconds of each drop. At the onset of low-power heating in Figure 2.11 (a), a $\Delta T \approx 1.5$ K is required to induce flows for centre heating (black line), whereas a higher $\Delta T \approx 2.5$ K appears to be insufficient for the edge-heating case (red line). Eventually both cases exhibit a similar behaviour where ΔT decreases and remains virtually constant.

On the other hand, for the middle-power case in Figure 2.11 (c), an initial increase $\Delta T \approx 2.0$ K results in the emergence of the vortices for both centre and edge heating. Eventually, the centre-heating case exhibit an oscillating behaviour of ΔT that corresponds to the observed merging and splitting of the vortices (middle column of Figure 2.9) as discussed in the previous section. On the contrary, during edge heating, ΔT appears to increase until reaching a plateau at $\Delta T \approx 2.5$ K and at approximately 40 seconds a fluctuation begins, corresponding to the periodic increase in the strength of one vortex with a decrease in the other one and oscillation of the recirculating front around the main heat path as shown in Figure 2.10.

Lastly, for the high-power case Figure 2.11 (e), both the centre- and edge-heating cases result in a slightly higher $\Delta T \approx 2.5$ K for the onset of recirculation. Eventually, ΔT begins to oscillate around a constant value of 1.9 and 2.5 K for centre and edge heating, respectively. In a similar manner to the middle-power case, the observed oscillation corresponds to the sequential shift of the vortices from one side of the drop to the other for centre heating (black line) and around the main heat flow path for edge heating (red line). Moreover, the higher ΔT when heating the edge of the drop at each irradiation power could be attributed

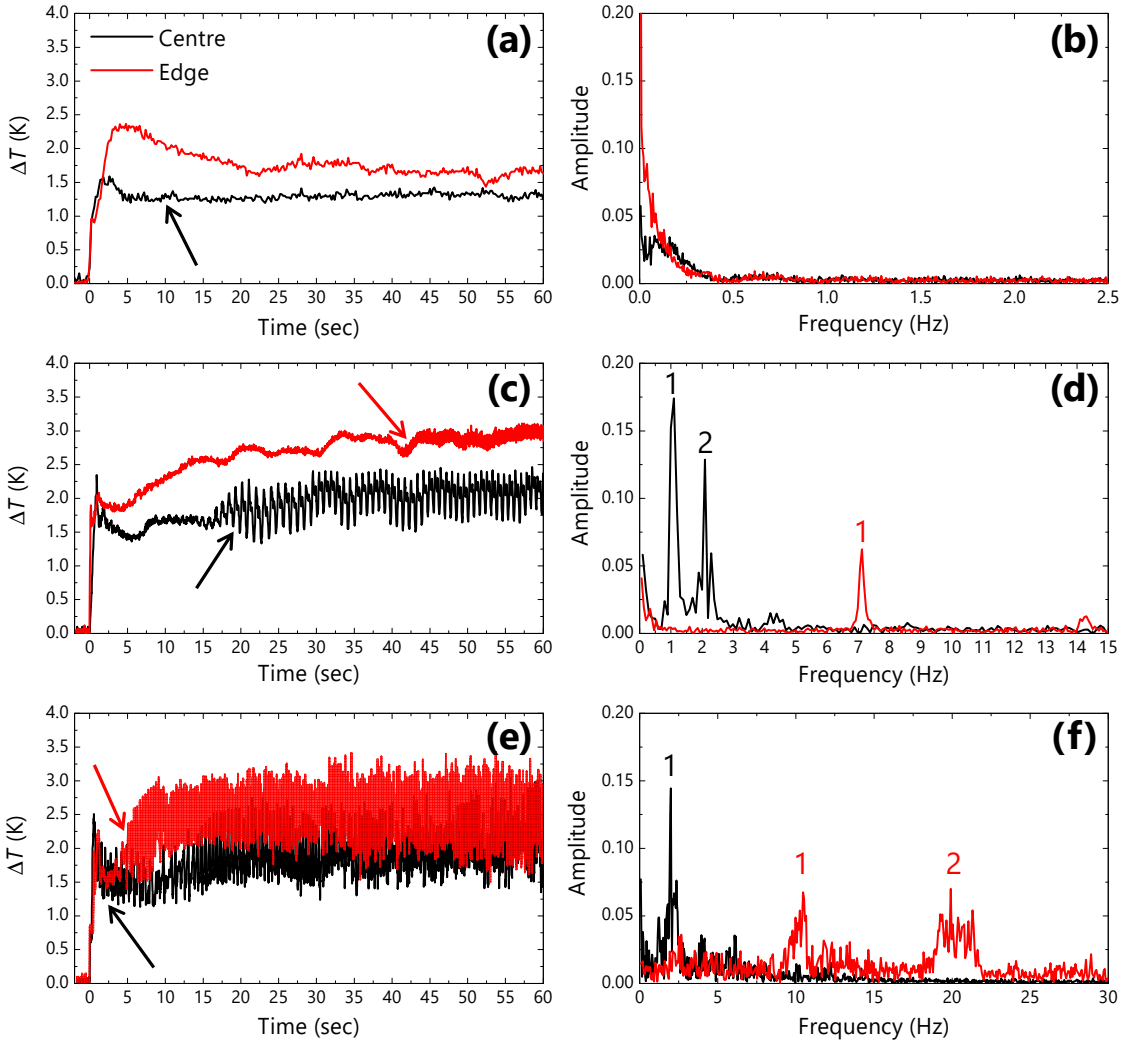

Figure 2.11 (left: (a), (c) and (e)) Evolution of temperature difference of the drop surface, ΔT as a function of time for centre (black) and edge (red) heating locations. Arrows indicate the onset of stage 4. (right: (b), (d) and (f)) Corresponding power spectrum obtained by the FFT analysis of ΔT oscillation during stage 4 for each case. In all cases, laser irradiation is initiated at 0.0 sec and power increases from top to bottom rows.

to the shorter heat conduction path from the substrate to the liquid–air interface, leading to a greater thermal gradient along the drop surface.

Characteristic frequency

Next, the corresponding power spectrums obtained by FFT of the ΔT temporal evolution during stage 4 are presented in the right column of Figure 2.11. No distinguishable peak for either centre or edge heating can be identified for the low-power case in Figure 2.11 (b). On the other hand, increasing the heating

power to the middle results in the emergence of a major peak at *ca*. 1.1 Hz and minor ones around 2 Hz for centre heating (black line), whereas edge heating (red line) exhibits a peak at 7 Hz, as shown in Figure 2.11 (d). Further increase in heating power to the high (Figure 2.11 (f)) leads to a dominant frequency around 2.5 Hz for centre heating and to two similar amplitude peaks at frequencies of *ca*. 11 and 20 Hz for edge heating.

Dimensional analysis—Marangoni, Rayleigh, frequency and velocity

According to a dimensional analysis and supplemental experiments with an inverted system presented in section 2.3, the origin of the flows for middle-power heating to the centre of the drops is identified as Marangoni- or thermocapillary-driven instabilities, and the same criterion is applied to other cases here. The values of *Ra* and *Ma* are calculated using Eq. (2.1) and (2.2), respectively, and are presented in Table 2.2 along with the average ΔT of each drop during stage 4 and *Bd* (= *Ra*/*Ma*). In all cases, *Bd* is sufficiently smaller than unity, which, combined with the fact that the *Ra* remains below the critical value of 1000 [166] for every case, allows to safely conclude that the observed flows are Marangoni in origin.

Furthermore, the frequencies of oscillatory ΔT (right column of Figure 2.11) corresponding to either merging/splitting of the vortices or sequential fluctuation of the strength of the recirculating front are comparable to the characteristic Marangoni frequencies, f_{Ma} defined in subsection 2.3.2, which are also listed in Table 2.2.

As Marangoni flows attempt to homogenise the temperature within the drop, the strength of the flows/vortices should be a function of the heating power or resulting ΔT. Hu and Larson [104] have proposed an analytical solution for velocity fluids inside sessile drops under Marangoni stress and based on this, Bhardwaj *et al*. [168] have later proposed the characteristic Marangoni velocity which scales as $v_{Ma} \sim (\partial \sigma_{LV}/\partial T)\left(\theta^2 \Delta T/32\mu\right)$, where μ denotes the dynamic viscosity (μ = 1.0 × 10^{-3} Pa·s for pure water). Using the values of ΔT given in

Table 2.2 Influence of heating location and power on ΔT, Ra, Ma, Bd and f_{Ma}.

Heating location and laser power	ΔT (K)	Ra (-)	Ma (-)	Bd (-)	f_{Ma} (Hz)
centre, low (0.3 W)	1.38	190	3700	0.046	7.19
centre, middle (1.9W)	1.63	600	7800	0.076	8.02
centre, high (3.4 W)	1.97	700	8800	0.082	9.00
edge, low (0.3 W)	1.88	180	4600	0.046	8.57
edge, middle (1.9 W)	1.94	680	10100	0.072	8.96
edge, high (3.4 W)	2.22	950	11000	0.081	9.41

Table 2.2 and θ extracted from the CCD images yields v_{Ma} varying from 24 to 38 mm/s, approximately, as a function of ΔT. It is evident in Figure 2.11 and Table 2.2 that ΔT increases with raising irradiation power regardless of heating location, thus, the heating power should accelerate the thermocapillary flows in line with the literature [73]. Moreover, heating the edge of the drops should also achieve a higher velocity for each heating power.

2.4.3 Triple-line motion

The drops in all cases presented herein exhibit stick-slip evaporation mode, which is evident in the plots of contact radius R_{SL} (Figure 2.12 (a)–(c)) and contact angle θ (Figure 2.12 (d)–(f)) as a function of time and with increasing irradiation power from left to right. In Figure 2.12, the effect of heating centre and edge is also plotted in each panel with black and red lines, respectively. As described in subsection 1.1.4, stick-slip consists of pinning of the triple-phase contact line (TL), during which R_{base} remains virtually constant with decreasing θ, interrupted by instantaneous depinning events that may be identified as a rapid drop in R_{base} and an increase in θ.

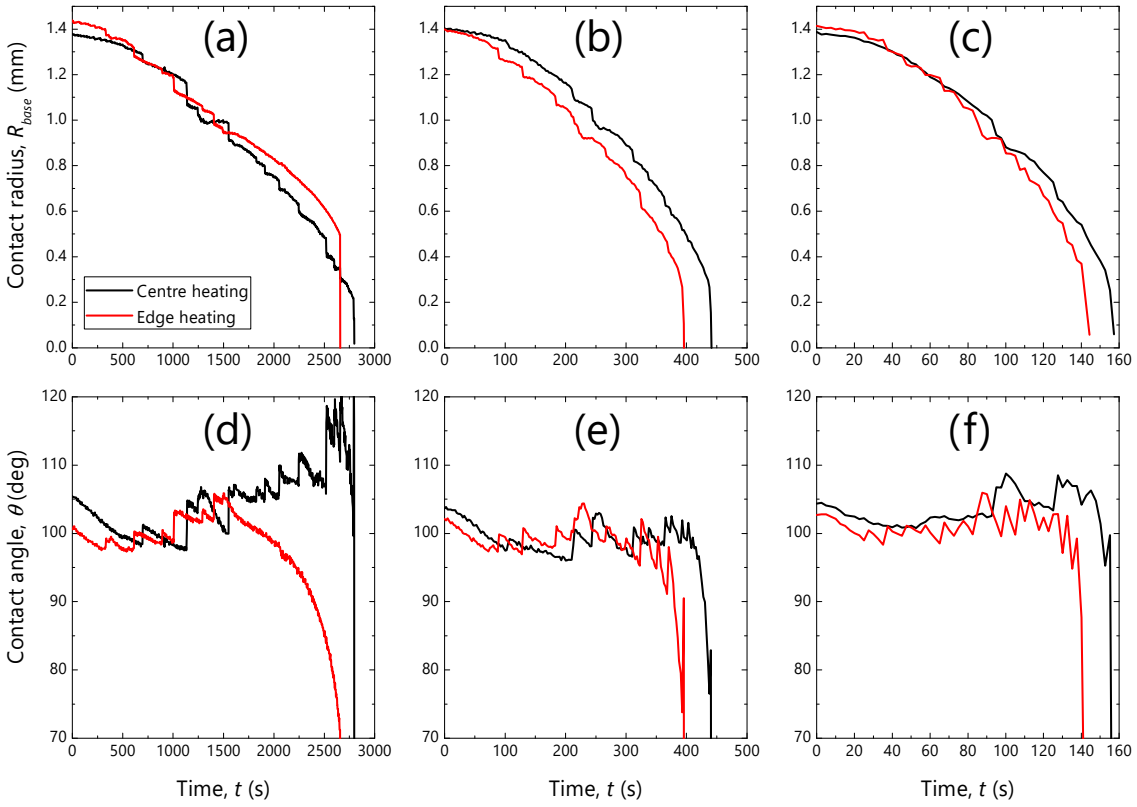

Figure 2.12 Evolution over time of (top: (a)–(c)) contact radius R_{base} and (bottom: (d)–(f)) contact angle θ for each irradiation power increasing from left to right.

The pinning/depinning events during evaporation presented in Figure 2.12 is provided only by the side-view camera. The top-view IR imaging is also helpful to observe TL motion and to alleviate this deficiency. Figure 2.13 depicts locations of TL during each pinning event obtained by tracing the periphery of the drop from the IR images. From this simple illustration, one may extract further information about the effect of, mainly, heating location on the TL motion kinetics. In more detail, at low irradiation power both centre and edge heating show a negligible effect on TL motion whereas increasing the power results in a noticeable difference. Particularly, a preferential depinning of the TL can be seen for the edge-heating case *i.e.* the drop moves away from the hot spot. This directional depinning could be thermocapillary-driven: edge heating should lead to a local, lower surface tension there compared to the cold side. In turn, higher surface tension around the heating spot should pull the lower surface tension

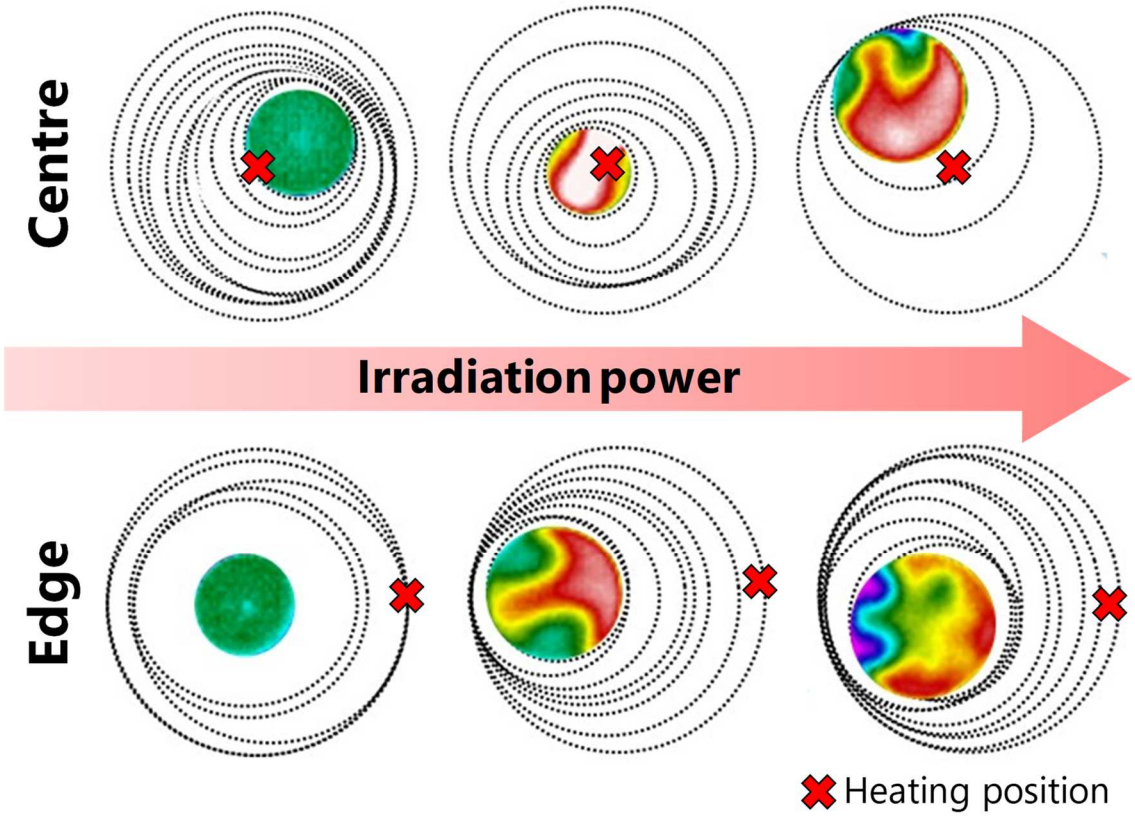

Figure 2.13 History of contact line location during each pinning event indicated with dashed lines, as extracted from the experimental IR data for all drops presented. Initial drop diameter in every case is *ca*. 3 mm. Temperature maps of the drops after the final depinning event are also presented. Red crosses denote the heating location.

part, allowing the TL to depin. A second potential and complementary depinning mechanism could be the continuous, one directional Marangoni flow, carrying the liquid from the hotter to the colder side. In addition, the local evaporative flux may be maximum at the local heating spot. In turn, the amount of the liquid on the hot side should deplete faster and lead to more depinning event at that side. Moreover, the highest power case in centre heating exhibits a similar behaviour. This could perhaps be attributed to the fact that after the first depinning event, which may not be perfectly uniform, the hot spot would no longer be at the centre and the heating regime becomes a sort of edge heating, leading to the preferential depinning.

2.4.4 Influence of local heating on evaporation rate

Figure 2.14 (a) depicts the loss of normalised volume as a function of time. Drop volume was extracted from the CCD images using the axisymmetric drop shape analysis (during initial stage of evaporation) and the circular fitting method (during later stage) as described in subsection 1.2.3. Temporal evolution of the volume is not linear with time for every case and follows the same trend as previously reported for receding TL scenario [61], [66], [126], [169]. Although clear enhancement of evaporation due to increasing heating power is obvious, the heating location effect is not evident in Figure 2.14 (a). Therefore, the average evaporation rate for each case is plotted as a function of irradiation power in Figure 2.14 (b). A clear dependence of the evaporation rate on heating location can be seen *i.e.* faster evaporation for edge heating and it becomes more prominent when increasing heating power. This heating location effect could be explained by the fact that heating the edge of the drop could create a large temperature gradient (large ΔT) along the surface, capable of driving faster recirculation as calculated in subsection 2.4.2. Strong recirculation can transfer the heat supplied by laser irradiation more efficiently and the heat will eventually be consumed for evaporation.

Let us now attempt to assess the contribution of local heating to drop evaporation by comparing the experimental evaporation rate with that predicted by the diffusion theory. From Eq. (1.10) in Chapter 1, the volume change per unit time is generally given by

$$-\frac{dV}{dt} = \frac{\pi R_{base} D_{AB}(c_s - c_\infty)}{\rho} f(\theta), \tag{2.3}$$

where

$$f(\theta) = \frac{\sin\theta}{1+\cos\theta} + 4\int_0^\infty \frac{1+\cosh 2\theta\tau}{\sinh 2\pi\tau} \tanh\{(\pi-\theta)\tau\}\, d\tau, \tag{2.4}$$

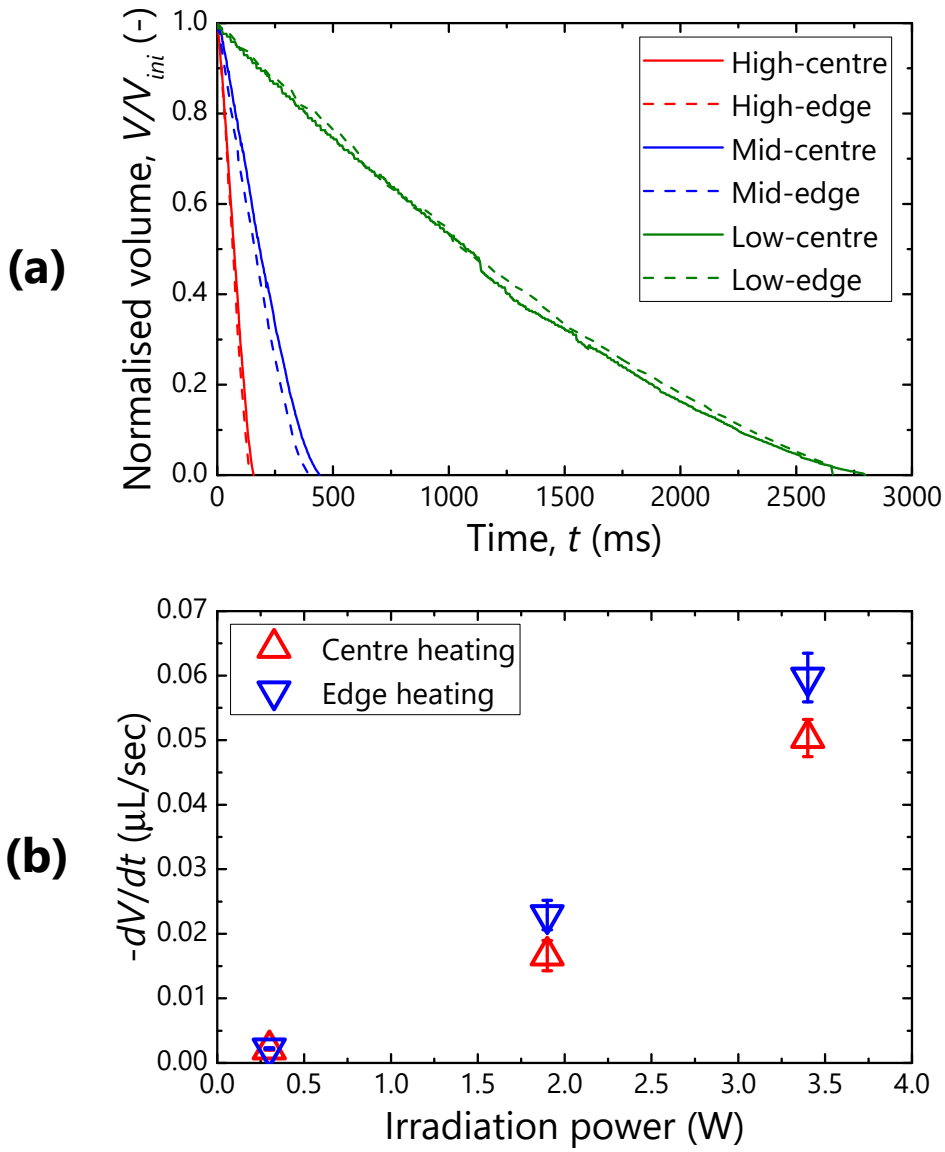

Figure 2.14 (a) Volume loss as a function of time for each drop presented in Figure 2.13. Drop volume V at each time is normalised by the initial volume V_{ini}. (b) Influence of heating power and location on the average evaporation rate $-dV/dt$ of the drops.

The diffusion coefficient D_{AB} for a binary system such as air-water environment can be expressed as [170]

$$D_{AB} = \frac{0.00266 T_{\infty}^{3/2}}{P M_{AB}^{1/2} \lambda_{AB}^{2} \Omega_{D}}, \tag{2.5}$$

where λ_{AB} is the characteristic Lennard-Jones length, Ω_D the diffusion collision integral, M_{AB} the molecular weight of gas A and B related as $M_{AB} = 2(1/M_A + 1/M_B)^{-1}$, and P the pressure. Since the experiments are carried out in atmospheric pressure, $D_{AB} \sim T_\infty^{3/2}$. The drop-temperature-dependent parameter, c_s may be treated as a linear function in the temperature range of this work:

$$c_s(T) = c_s(T_\infty) + \frac{dc_s}{dT}(T - T_\infty), \tag{2.6}$$

where $c_s(T_\infty) = 1.93 \times 10^{-2}$ kg/m^3 and $dc_s/dT = 1.11 \times 10^{-3}$ kg/(m^3·K), at ambient temperature $T_\infty = 295$ K and pressure $P = 1$ atm. Inputting the experimental data for drop temperature T and θ in Eq. (2.3)–(2.6), the evaporation rate of all drops may be estimated to vary $1.96 \times 10^{-3} < -dV/dt < 7.55 \times 10^{-3}$ μL/sec from low to high power. Comparison of these theoretical values with the experimental ones shown in Figure 2.14 (b), which varies $2.09 \times 10^{-3} < -dV/dt < 59.71 \times 10^{-3}$ μL/sec, suggests that the diffusion model clearly underpredicts the evaporation rate and should be revisited for the case of locally heated drops.

2.5 Summary

The first experimental observation and induction of very active Marangoni (or thermocapillary) convection in pure water drops have been demonstrated in this chapter. Drops are heated locally (~20% of drop contact area) using a laser, which gives rise to unique thermal gradients along the liquid-air interface. IR thermography allows to map interfacial temperatures of the drop, showing that counter-rotating vortical thermal patterns appear when a temperature gradient reaches approximately 2.5 K. As laser irradiation goes on, the thermal activity becomes more unstable; the vortices begin to merge and split in an oscillatory manner. The fluctuation can also readily be detected in the maximum temperature difference within the drop which oscillates around 1.25 K with an

amplitude of *ca*. 0.3 K and a major frequency of *ca*. 1.05 Hz as well as minor ones of 2.09 and 2.27 Hz.

A question whether these thermal patterns are buoyancy or thermocapillary driven is the major interest in this chapter as the existence of Marangoni convection in pure water has been controversial. Following analysis done in the previous reports [33], [37], [115], [117] for Marangoni-driven HTWs in organic liquids, the dimensionless Rayleigh *Ra* (for buoyancy) and Marangoni *Ma* (for thermocapillarity) have been calculated using the temperatures and the characteristics lengths extracted from the IR and CCD observations. As a consequence, *Ma* varies about 4000 whereas *Ra* is kept below 500, which is much lower than the critical *Ra* (typically in the order of 10^3) for natural convection to set in. Comparison between *Ra* and *Ma* has unveiled the dominance of Marangoni convection over buoyancy. A second set of experiment with an inverted system, which has yielded the similar thermal patterns to the normal cases, has provided further evidence that the observed thermal motion is due to the action of Marangoni/thermocapillary effect.

Additionally, particle imaging for a direct flow visualisation qualitatively has validated the analysis based on the thermal behaviour. Similar vortical flow patterns and corresponding merging/splitting behaviour have been observed, proving that the observed thermal patterns coincide with actual hydrodynamic flows recirculating within the drops.

Having established the emergence of Marangoni flows in water drops, next, a systematic analysis has been performed to investigate how local heating power and location affect the flow pattern and evaporation kinetics. The flows have been found to be directional when heating at the edge of the drops *i.e*. two hemispheres of vortices are generated such that the liquid recirculates continuously in a direction from the heating side to the other side. Oscillatory behaviour of the vortices during edge heating is also different from the case for

centre heating: a periodic increase in the strength of one vortex with a decrease in the other one. Besides the heating location, the frequency of the temperature oscillation is subject to heating power.

Furthermore, the effect of localised heating on the evaporation and triple-line motion has been probed. Interestingly, preferential depinning of the contact line has been observed when heating the drop edge. This may be attributed to thermocapillary forces acting from the hot region toward the cold one. As a result, the contact line moves away from the hot spot, which could be regarded as thermocapillary migration as can be seen on a lubricant-impregnated surface [42]. Additionally, a clear contribution by local heating to drop evaporation has been revealed and the diffusion model would no longer be sufficient to predict the evaporation rate.

These findings should contribute to shed light on hydrothermal instabilities in pure water drops which have been thought to be rather irregular compared to other liquids. Overall, these findings show the potential to induce and manipulate Marangoni flows paramount to applications such as uniform coating, drop mixing for microfluidic devices and phase-change-based heat transfer devices.

Chapter 3

Drop Motion on Surface Wettability Contrasts

In contrast to what happens in a liquid drop experiencing the surface-tension gradients imposed by temperature gradients along the drop surface (Chapter 2), here this chapter deals with the dynamics of a drop on a solid surface with heterogeneous wettability, which has recently been of great importance for drop-based microfluidic applications.

Besides various drop manipulation techniques based on chemical-gradient [38], [39], [148], [151]–[153], [155], [171], thermocapillary [38], [41], [42], [155], [156], [172]–[174], and electrowetting [154], [157], [158], [173] principles, micropillar fabrication on surfaces is another promising method that allows precise control of wettability. However, most of experimental works reported previously required additional mechanical forces *i.e.* vibration to enable drop motion on microtexture-wettability gradients [159], [160]. Due to the lack of understanding on wetting dynamics and the effect of contact angle hysteresis (CAH), the optimum design of functional surfaces capable of actuating drops has been challenging.

To address these problems, Chapter 3 considers a drop experiencing a gap of wettability, namely a wettability contrast, between its front and back and how it will behave depending on the degree of wettability contrasts. In particular, a millimetre-sized water drop is placed at the interface between two surfaces with different wettabilities imposed by fabricating microstructures that exhibit a Cassie-Baxter (CB) wetting regime (see subsection 1.2.2). As a systematic analysis,

the mobility of drops is evaluated in terms of drop velocity, as a function of differential surface area fraction which induces a directional capillary force. To elucidate the underlying mechanism of drop motion, a surface energy analysis is performed and the criterion for the onset of spontaneous drop motion is proposed.

3.1 Experimental

3.1.1 Micropillared surfaces

Surfaces used in this study comprises arrays of uniformly arranged square (cross-section 5 × 5, 10 × 10 and 20 × 20 μm^2) and circular (diameter 10 μm) pillars, with spacings between pillars ranging from 5 to 80 μm. As a consequence, the surface area fraction varies ϕ = 0.003 – 0.444. The pillars are fabricated on silicon wafers at the Scottish Microelectronics Centre using photolithography and deep reactive ion etching. In order to attain superhydrophobicity, the surfaces are then coated with a perfluorodecyltrichlorosilane (FDTS) monolayer by molecular vapour deposition using MEMSstar's ORBIS 1000 AURIX platform, which provides a contact angle of θ_E = 114° ± 6.7° on a flat surface. The surface area fractions (ϕ) and wetting characteristics (apparent (θ_{app}), advancing (θ_{adv}) and receding (θ_{rec}) contact angles) are summarised in Table 3.1 for each surface used. Here, each surface is named S-j-k where S denotes the shape (Sq stands for square and Ci circular), j the lateral dimension or diameter and k the interstructural spacing in micrometre, respectively (as illustrated in the inset). θ_{app} of each surface are close to those calculated by Eq. (1.3), hence the drops can be assumed to be following the CB or fakir wetting regime. Exemplary optical microscopic photographs of Sq-10-40 and Sq-10-20, and 3D laser scanning microscopy for the interface between Sq-10-40 and Sq-10-20 taken with an Olympus LEXT OLS4000 are presented in Figure 3.1.

Table 3.1 List of experimental surfaces with their surface area fractions (ϕ) and apparent (θ_{app}), advancing (θ_{adv}) and receding (θ_{rec}) contact angles. Contact angles of each surface are measured five times and the mean values and the standard deviations are presented. Inset describes pillar dimension, arrangement and definitions of ϕ and the normalised maximum three-phase contact line (δ), which is defined in subsection 3.2.3.

Surface name	ϕ	θ_{app} (deg)	θ_{adv} (deg)	θ_{rec} (deg)
Sq-5-5	0.250	148 ± 1.6	163 ± 0.2	116 ± 5.0
Sq-5-20	0.040	163 ± 0.5	171 ± 0.3	148 ± 0.5
Sq-5-40	0.012	167 ± 0.7	170 ± 0.6	160 ± 1.3
Sq-5-80	0.003	169 ± 0.8	169 ± 1.0	164 ± 1.8
Sq-10-5	0.444	151 ± 1.0	165 ± 2.1	118 ± 3.4
Sq-10-20	0.111	154 ± 0.8	171 ± 0.5	132 ± 2.1
Sq-10-40	0.040	164 ± 1.0	172 ± 1.6	147 ± 1.3
Sq-10-80	0.012	166 ± 0.5	170 ± 1.4	152 ± 1.2
Sq-20-20	0.250	150 ± 1.1	165 ± 2.3	123 ± 3.2
Sq-20-40	0.111	155 ± 0.9	169 ± 0.9	136 ± 1.9
Sq-20-80	0.040	163 ± 0.8	169 ± 1.0	145 ± 2.3
Ci-5-5	0.349	151 ± 1.3	168 ± 3.7	116 ± 2.8
Ci-5-20	0.087	158 ± 1.1	169 ± 0.6	138 ± 1.9
Ci-5-40	0.031	163 ± 2.5	170 ± 1.2	151 ± 1.8

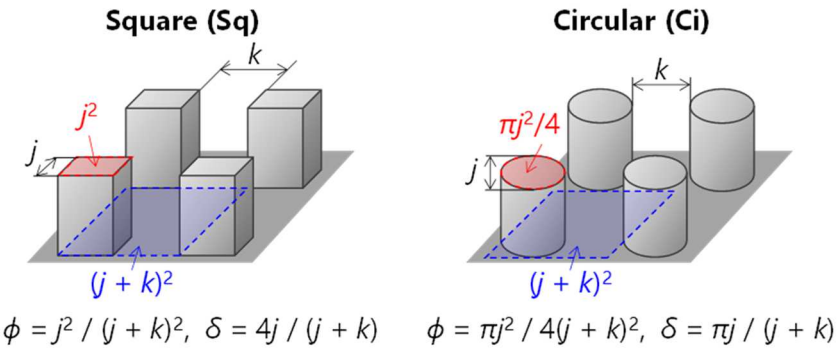

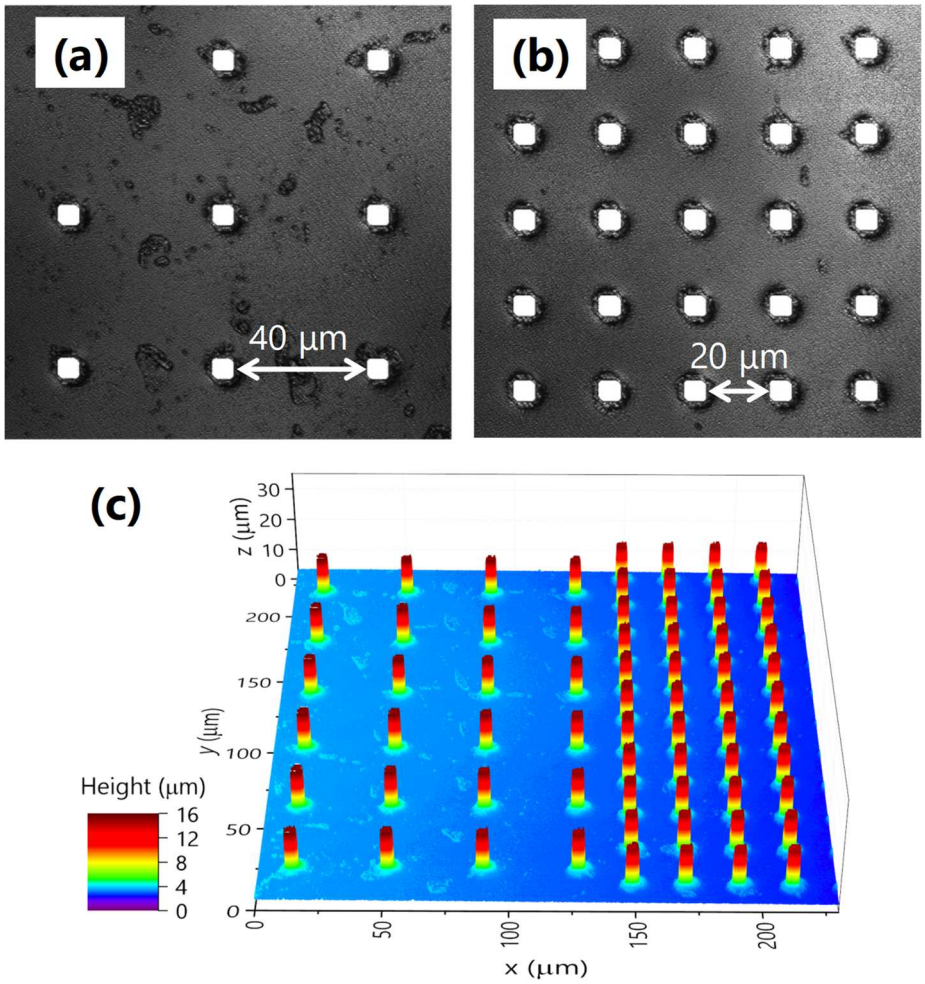

Figure 3.1 Photographs of (a) Sq-10-40 and (b) Sq-10-20, and (c) 3D scanned micro-topography of the interface between Sq-10-40 (left) and Sq-10-20 (right).

3.1.2 Experimental setup and procedures

The centre of 10 μL drops of deionised water are placed at the interface between two surfaces with different ϕ (Figure 3.2 (a)). Drop deposition is carried out using a computer controlled liquid dosing system (KRÜSS DSA100, Figure 3.2 (b)), which is connected to a syringe needle with a 0.51 mm outer diameter. Procedures are kept consistent and extra care is taken in order to deposit drops under the CB regime; water is fed into a drop from the needle at about 2.7 mm above the substrate surface. The height of deposition was set to be slightly higher than the diameter of a 10 μL sphere such that the hanging drop lands on the

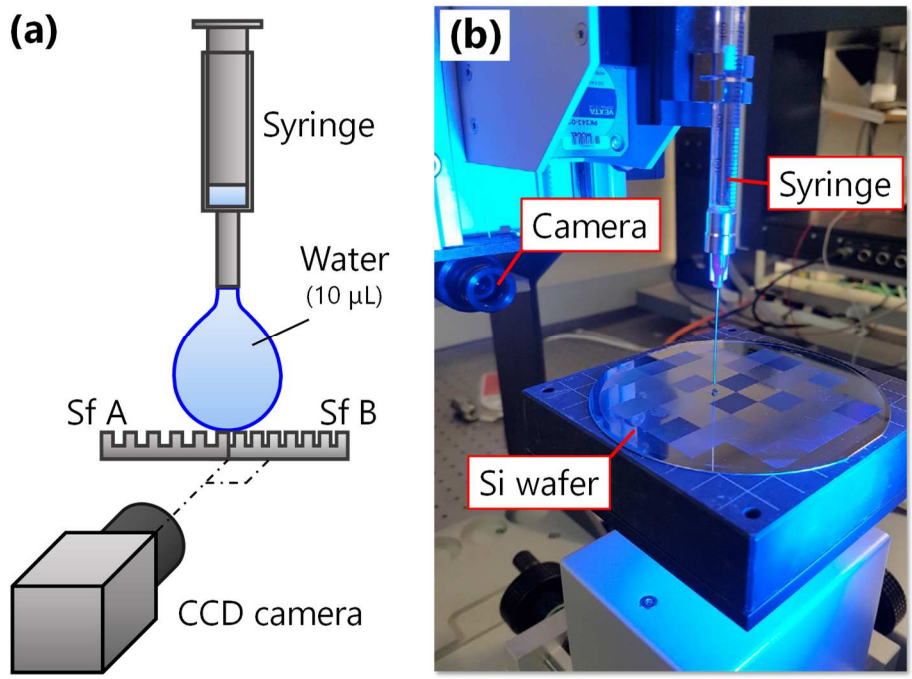

Figure 3.2 (a) Schematic illustration of the experimental system and (b) photograph of the drop dosing setup (KRÜSS DSA100).

surface without an extra pressure which may trigger the transition from the CB to the Wenzel state. The needle then retreats at 0.8 mm/s and the drop is released at approximately 3.0 mm above the surface due to the imbalance between the drop-needle and drop-surface adhesive forces and gravity. Motion of the drop is captured by a high-speed CCD camera (iDS UI-3060 CP with a SONY 2.3 MP sensor) with a resolution and frequency of 6 µm/pixel and 250 Hz, respectively. Subsequently, the videos are analysed to trace the drop motion (displacement and velocity) as well as the drop shape (contact angles, radius, volume *etc*.) using a custom-built Matlab code. Experiments are carried out under atmospheric conditions and repeated at least 10 times for each interface to establish reproducibility.

3.2 Results and Analysis

As a systematic analysis, eleven combinations of the surfaces listed in Table 3.1Table 2.2 are investigated to parameterise the differential surface area fraction $\Delta\phi$ between 0.009 and 0.441, which is directly related to the differential contact angle. In all cases, the same trend in motion is observed. Thus, this section presents the representative case of the interface between Sq-10-40 (ϕ = 0.040) and Sq-10-20 (ϕ = 0.111) to comprehend drop behaviour (see A.1 in Appendix for the other cases).

3.2.1 Drop motion

Figure 3.3 shows the motion of a drop placed at the interface (cyan dashed line). Initial time (t = 0 ms) is set to the frame at which the drop detaches from the needle. Once detached, the drop spontaneously moves toward Sq-10-20, which possesses denser pillars and hence lower θ_{app}. To follow drop displacement, the positions of the front, rear and middle contact points, depicted with red, blue and green respectively, are tracked during the motion. These points are plotted as a function of time in Figure 3.4, where the non-monotonic drop motion becomes readily apparent in contrast to the cases for chemical patterned surfaces [39], [152]. Contact point behaviour for other cases can be found in Figure A 1 in A.1.1. In fact, the drop oscillates vertically, resulting in sequential wetting and dewetting events, which are indicated with insets in Figure 3.4. During a wetting event, both sides of the drop spread forming a "pancake" shape, whereas in a dewetting event, both sides retract forming an "egg" shape. The drop is found to advance mainly during the dewetting event, due to an asymmetric retreat between the front and rear sides of the drop. In particular, the rear side of the drop retreats significantly whereas the front one is almost pinned. On the contrary, the drop spreads rather evenly during the wetting event, with imperceptible contribution to the displacement. Similar drop motion has been

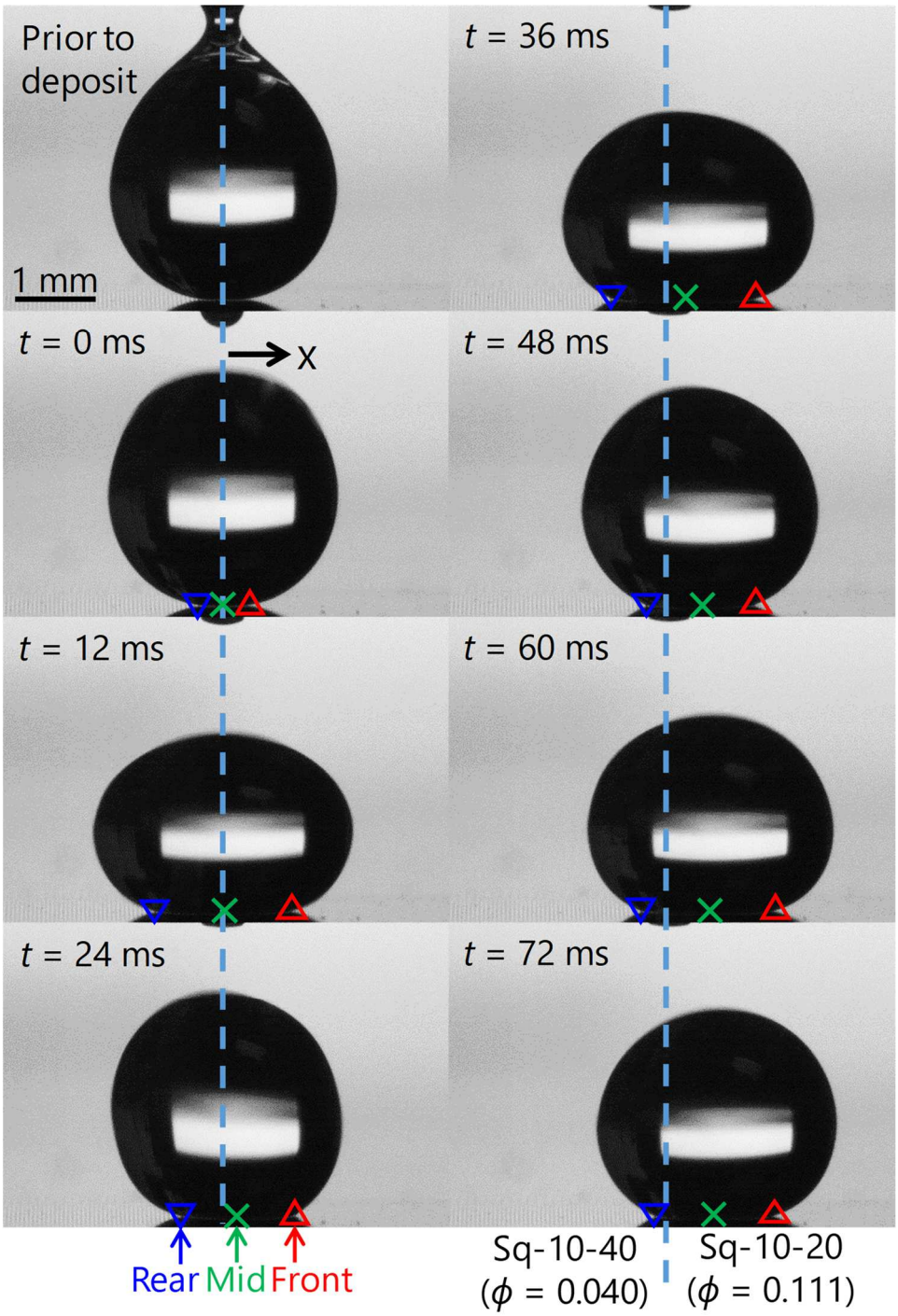

Figure 3.3 Sequential snapshots of a 10 μL water drop moving on the interface between surfaces Sq-10-40 (ϕ = 0.040, left) and Sq-10-20 (ϕ = 0.111, right). Cyan dashed lines represent the interface between the two surfaces. Red up-triangles, blue down-triangles and green crosses represent the front, rear and middle contact points, respectively.

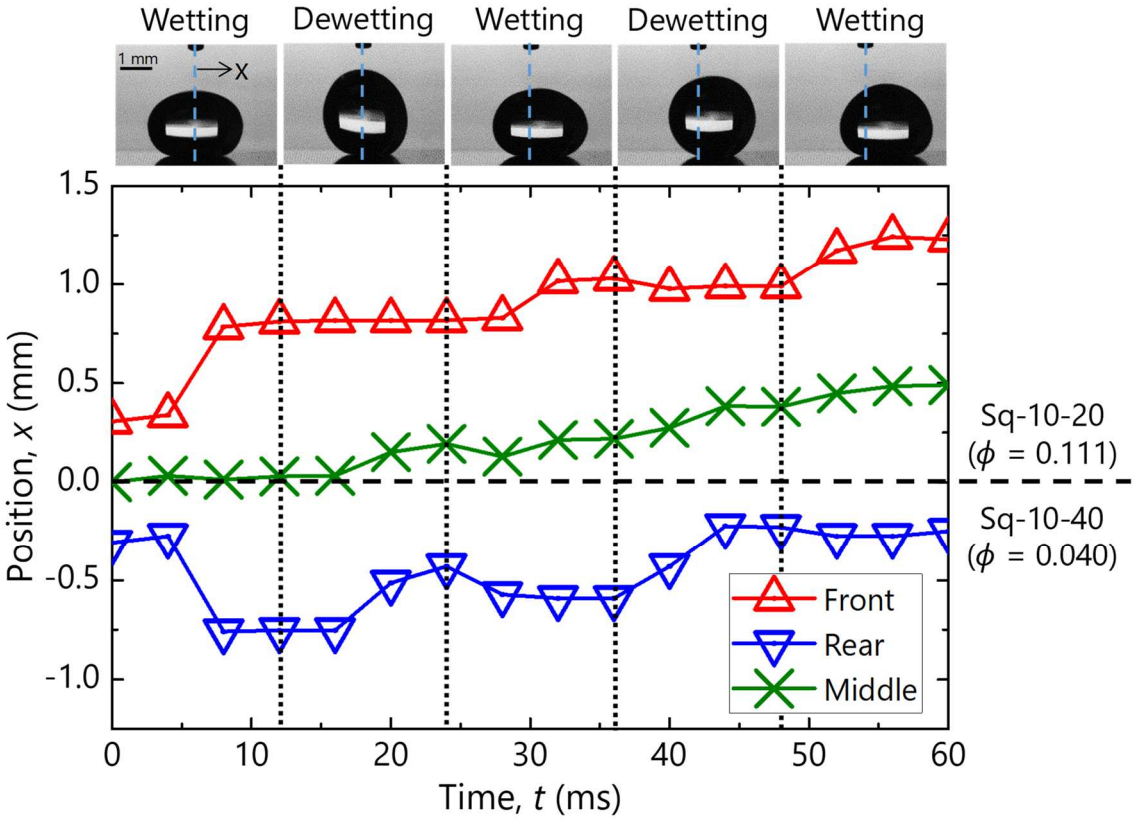

Figure 3.4 Evolution over time of each contact point (front, rear and middle). The position of the interface between Sq-10-40 (ϕ = 0.040, left) and Sq-10-20 (ϕ = 0.111, right) is set as x = 0 mm. Insets represent typical drop shape during wetting and dewetting events.

reported previously; albeit attributed to an imposed vibration to the system which provided necessary energy to initiate movement [159], [160]. In the present work however, the initial energy required for drop motion is provided from the deformation of the drop during deposition (see the first frame in Figure 3.3). This deformation leads to deviation from the equilibrium state, resulting in excessive energy accumulation. At the moment of drop release, the drop shrinks in an attempt to minimise its surface area, converting the excess surface free energy into kinetic energy. This will be further discussed later in 3.2.4.

3.2.2 Drop velocity versus $\Delta\phi$

The mean drop velocity v is calculated from the middle tracking point and is

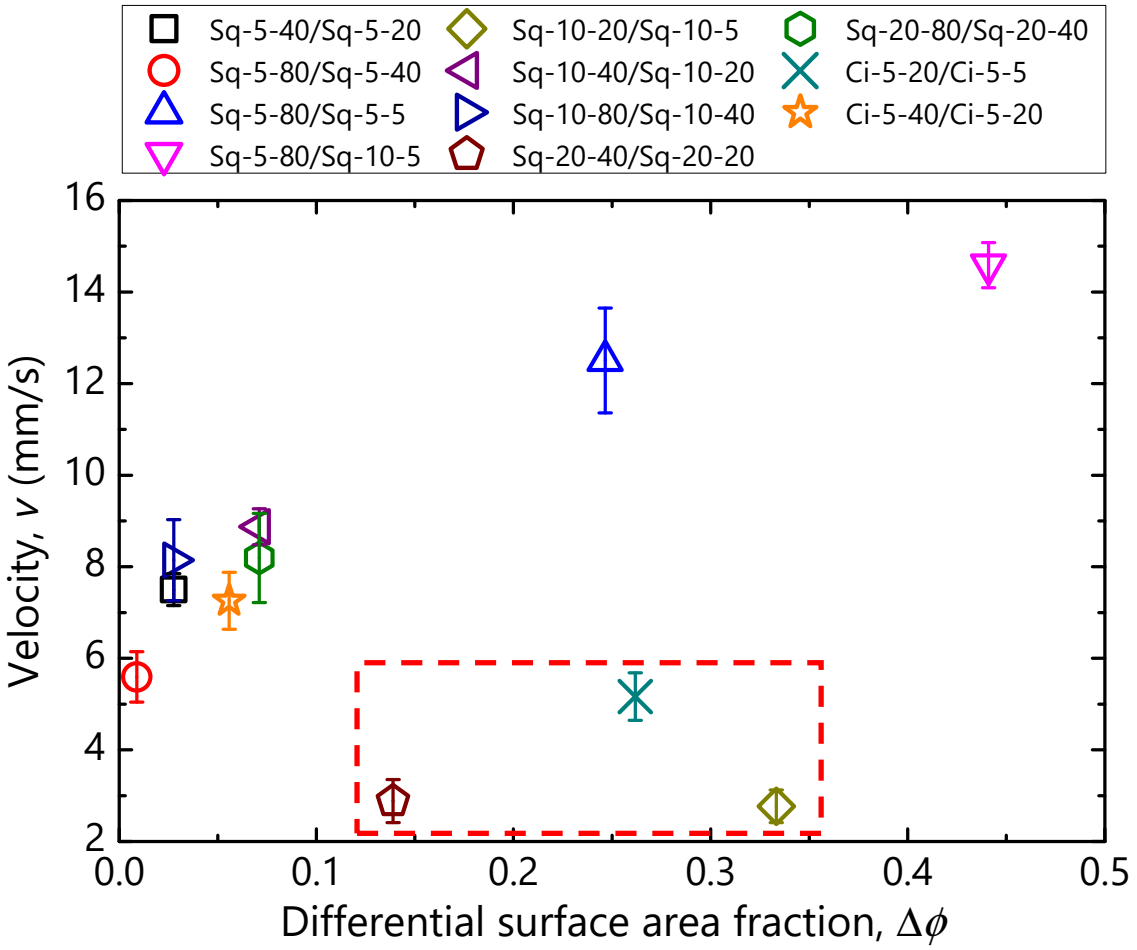

Figure 3.5 Drop velocity v as a function of differential area fraction $\Delta\phi$, for a variety of surface combinations, denoted in legend (rear/front). Red dashed box indicates the cases which show significantly slow motion of the drop compared with other cases.

plotted as a function of $\Delta\phi$ in Figure 3.5, in which fast and slow drops can be readily distinguished. The velocities of the faster drops range between 5–15 mm/s and are strongly related to $\Delta\phi$. On the other hand, the velocities of the slower drops, which are highlighted in the boxed area, are much smaller than the others and range between 3–5 mm/s in spite of relatively large $\Delta\phi$. Nonetheless, it can be deduced at present (Figure 3.5) the importance of $\Delta\phi$ on the drop velocity, which can be associated with translation of vertical vibration into horizontal motion according to the wettability gradient. The disambiguity between the faster and the slower drops will be probed in the following subsection.

3.2.3 Influence of contact angle hysteresis

Contact angle hysteresis (CAH) should be detrimental to drop motion as it results in a stronger pinning of the contact line and should be the underlying reason for the deviating cases in Figure 3.5. CAH is generally caused by chemical and physical (*e.g.* roughness) heterogeneity [28], [175]–[179]. In the present system, the pillars are most responsible for pinning the drop leading to CAH and the effect of pillars cannot be simply described in terms of ϕ [180]–[182]. Based on a microscopic observation of contact line motion, Xu and Choi [181] have proposed as the criterion for a drop to be sticky or slippery the normalised maximum three-phase contact line δ. As shown in the inset of Table 3.1, δ is basically the ratio of the pillar perimeter to the pillar pitch: δ = pillar perimeter/pillar pitch (δ = 1 for a flat surface). The pinning force per unit length is defined as $f_p = \sigma_{LV}\left(\cos\theta_{rec} - \cos\theta_{app}\right)$ [181], [183], [184], and f_p is plotted as a function of δ in Figure 3.6. Xu and Choi have reported that f_p will be larger than that of a flat surface (dashed line) if $\delta > 1$, and vice versa. Figure 3.6 shows that f_p of Sq-10-20 (δ = 1.33), Sq-20-40 (δ = 1.33) and Ci-5-20 (δ = 1.05), which are the rear sides of the boxed data in Figure 3.5, are found to be larger than the rest and than the equivalent flat surface ($f_p \approx$ 10 mN/m). It is also noteworthy that drop motion is not instantaneous in these unusual cases, attributable to the stronger f_p retarding drop motion on these surfaces. Consequently, the velocity of the drops increases as a function of $\Delta\phi$, provided that the pinning force of the rear surface is sufficiently small ($\delta < 1$).

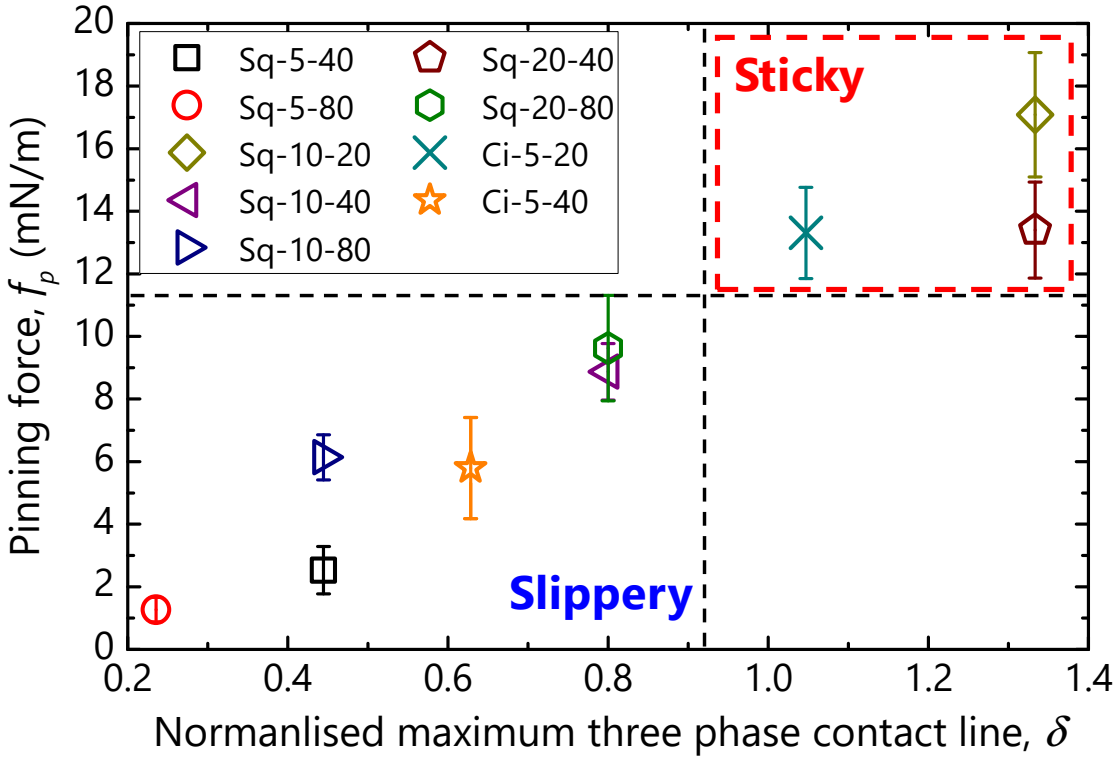

Figure 3.6 Pinning force f_p versus the normalised maximum three phase contact line δ for the rear surfaces. Vertical dashed line at $\delta = 1$ distinguishes between sticky ($\delta > 1$) and slippery ($\delta < 1$) surfaces. The data boxed with the red dashed line correspond to the slow drop cases presented in Figure 3.5.

3.2.4 Energy analysis

Let us at this point attempt to elucidate the underpinning mechanism of drop motion. An analysis of the surface free energy is performed as drop motion on wettability (or interfacial energy) gradients should be governed by the principle of minimum energy (or the second law of thermodynamics). The present study considers a system wherein a drop is placed at the interface between two surfaces, denoted as Sf A and Sf B, respectively, with different surface area fractions, *i.e.* ϕ_A and ϕ_B ($\phi_A < \phi_B$). Although the potential energy is influential to an extent as the drop oscillates in a vertical direction, it is assumed to be negligible in this analysis at present for simplicity and due to the fact that the Bond number, $Bo <$ 1 suggesting the dominance of the surface tension in the dynamics. The analysis

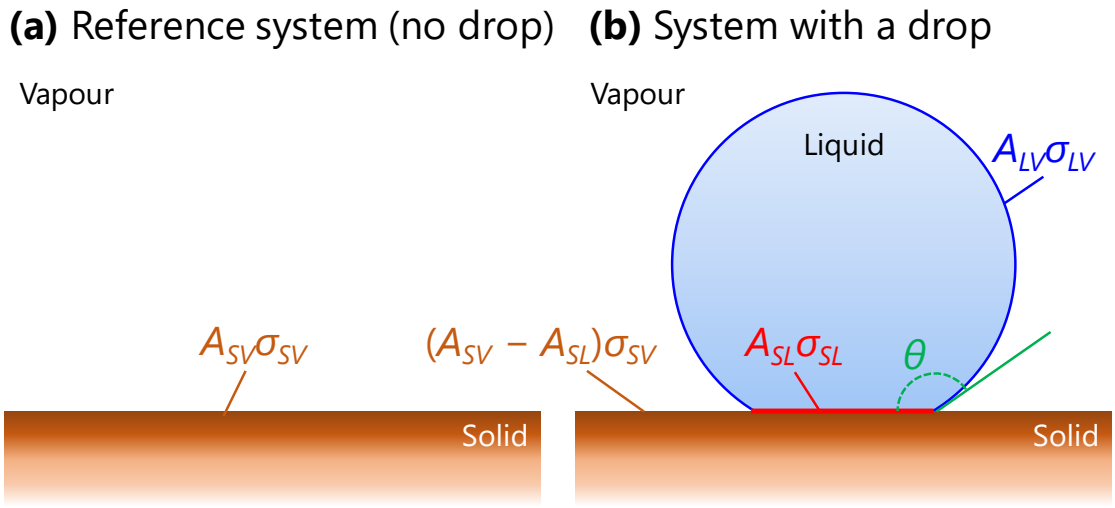

Figure 3.7 Schematic representation of (a) the reference system in the energy analysis presented in this section, where the surface is completely dry and (b) the system with a drop in contact with the surface at a contact angle of θ.

also assumes the isothermal system, and therefore, the change in the surface free energy is only treated.

Considering first here a flat solid surface with a surface tension with the vapour phase σ_{SV} (Figure 3.7 (a)), the surface energy of the reference system consisting of the dry surface with an area A_{SV} can be expressed as $A_{SV}\sigma_{SV}$. On the other hand, the energy of the system where the surface is partially wet by a drop with a contact area of A_{SL} (Figure 3.7 (b)) can be quantified as $A_{LV}\sigma_{LV} + A_{SL}\sigma_{SL} + (A_{SV} - A_{SL})\sigma_{SV}$, where A_{LV} is the liquid-vapour surface area. Ultimately, defining the surface "*free*" energy G of a drop in contact with a solid surface as the change in energy between the aforementioned states leads to [53], [185], [186]

$$G = A_{LV}\sigma_{LV} - A_{SL}(\sigma_{SV} - \sigma_{SL}). \tag{3.1}$$

Note that Eq. (3.1) is the general expression for drops in any state. In the present study, $\sigma_{SV} - \sigma_{SL}$ in Eq. (3.1) is approximated as $\sigma_{LV}\cos\theta_E$ using Young's relation expressed as Eq. (1.1), consequently:

$$G = (A_{LV} - A_{SL}\cos\theta_E)\sigma_{LV}. \tag{3.2}$$

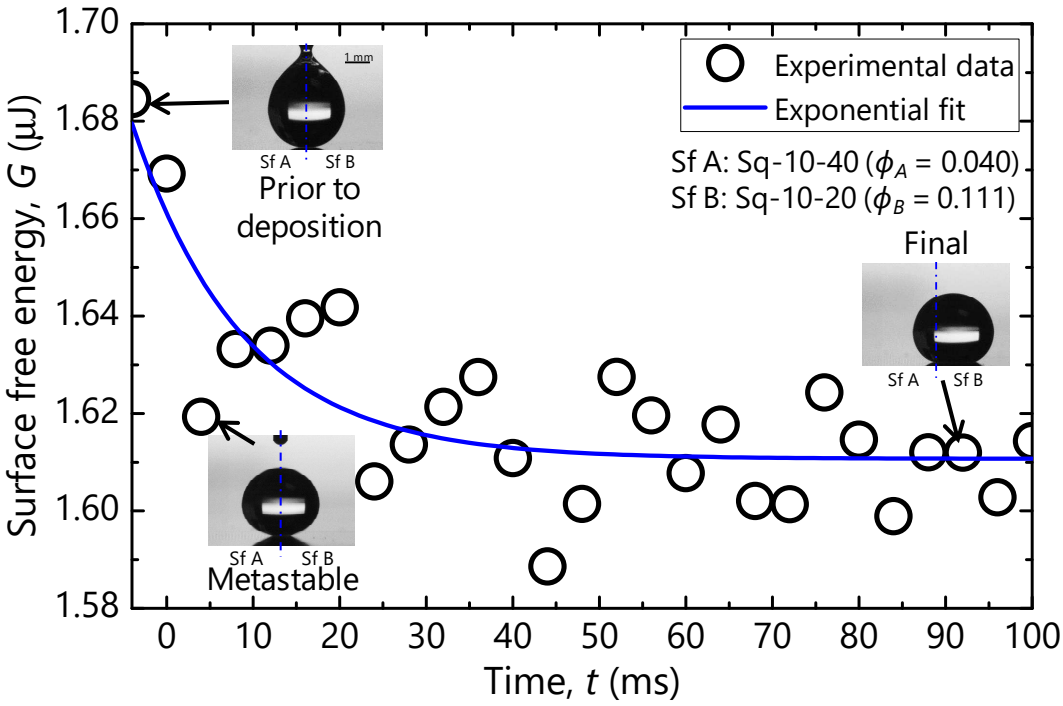

Figure 3.8 Example of the evolution over time of the surface free energy, G of a drop placed at the interface between Sq-10-40 (denoted as Sf A, ϕ_A = 0.040) and Sq-10-20 (denoted as Sf B, ϕ_B = 0.111). Insets are snapshots of the drop at each time. The experimental data points are fitted with the exponential decay function (blue line).

For the case of the Cassie-Baxter wetting state, A_{LV} and A_{SL} should be $A_{LV} = A_{cap} + (1-\phi)A_{base}$ and $A_{SL} = \phi A_{base}$, where A_{cap} and A_{base} denote the areas of the drop cap and base, respectively. Hence, Eq. (3.2) can be rewritten as $G = \{A_{cap} + (1-\phi)A_{base} - \phi A_{base}\cos\theta_E\}\sigma_{LV}$. Then, using Eq. (1.3) eventually leads to

$$G = \left(A_{cap} - A_{base}\cos\theta_{app}\right)\sigma_{LV}. \tag{3.3}$$

This may imply that Eq. (3.2) can be applied to any drop under the Cassie-Baxter wetting state by simply assuming a drop on a flat surface with an apparent CB contact angle *i.e.* $\theta_E = \theta_{app}$ [53], [186].

Figure 3.8 depicts the evolution of G as a function of time for the exemplary case of Sq-10-40/Sq-10-20 (see the left column of Figure A 2 in A.1.2 for the rest of the cases) which is calculated from the experimental observation. G is found to be maximal at the moment of drop deposition due to large surface deformation

(initial state). Immediately after release, the drop at the interface shrinks rapidly in order to minimise its surface free energy (metastable state, $G_{meta} \approx 1.62$ μJ). Subsequently, G reaches a plateau $G_{plateau}$ of *ca*. 1.61 μJ, around which it oscillates until finally settling on Sq-10-20 (final state). The motion may be explained by considering the clear dependence of G on θ_{app} in Eq. (3.3). θ_{app} depends on ϕ as shown in Table 3.1, hence, a drop on a contrast $\Delta\phi$ will move toward the surface with a larger ϕ to minimise G due to the fact the larger ϕ yields a lower θ_{app}. The oscillation may be attributed to shedding of excess free energy during motion and perhaps to the action of contact angle hysteresis (CAH). CAH is capable of pinning the drop (pinning barrier), resulting in deformation prior to or in oscillations during motion [187]. It is also worth noting that for every case studied, G is found to decay exponentially with time—$G(t) = G_{plateau} + G_{ini}e^{-\eta t}$ as indicated with a blue curve in Figure 3.8 (also in the left column of Figure A 2 for the other cases). The decay constant η could perhaps be dependent on drop size and properties as well as wetting conditions since the energy variations were apparently related to the oscillatory behaviour of the drop [188], [189].

Let us now rationalise how the drops are activated and directed by calculating energy diagrams and summarising them in four representative moments for each case studied. Figure 3.9 depicts the energy diagram calculated for the exemplary Sq-10-40/Sq-10-20 (denoted as Sf A/Sf B, respectively) system. The energy diagrams for the rest of the cases are included in the right column of Figure A 2 in A.1.2. In each diagram, the drop motion is divided into four representative energy states: initial, metastable, CAH barrier and final. G_A and G_B denote the equilibrium free energy for a drop resting entirely on Sq-10-40 (Sf A) and Sq-10-20 (Sf B), respectively. The metastable energy G_{meta} is defined as $G_{meta} = (G_A + G_B)/2$. G_{CAH} is the energy of the drop necessary to initiate motion and the calculation will be defined below. The initial energy G_{ini} is accumulated in the drop during deposition through its deformation (the first inset of Figure 3.8), and is calculated

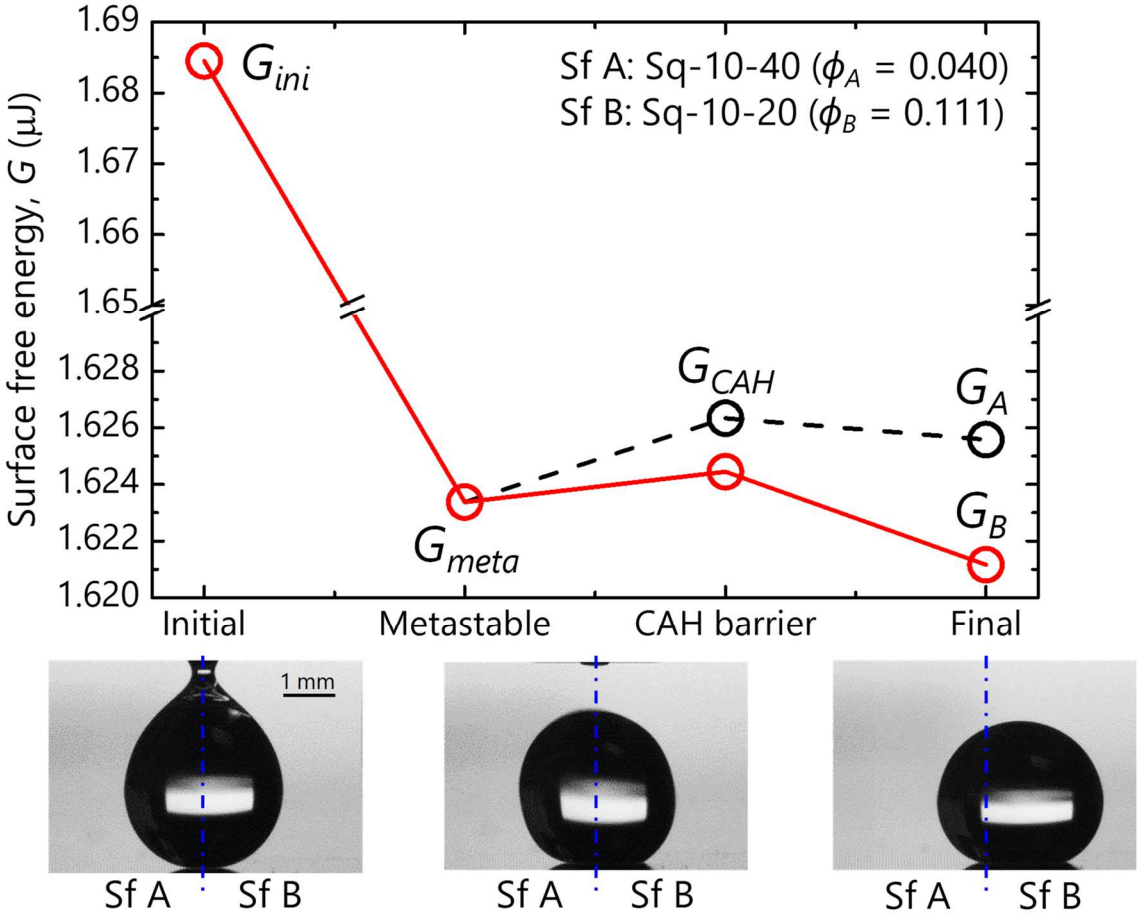

Figure 3.9 Representative energy states of the system consisting of Sq-10-40 (denoted as Sf A, ϕ_A = 0.040) and Sq-10-20 (denoted as Sf B, ϕ_B = 0.111). Insets show the drop in the initial (left), transition (middle) and final (right) states.

from the experimental image using Eq. (3.3). G_{ini} is found to be sufficiently larger than the peak of G_{CAH}, hence the drop at the wettability interface, as in the second inset of Figure 3.9, should move to the lowest energy state, G_B (red line). The third inset of Figure 3.9 shows the final position of the drop in the experiment and corroborates the present claim.

The reader should note here that the shape of the drops both at equilibrium and during deformation is complex due to gravitational and CAH effects [187], [190], [191] and cannot be extracted simply from the images. Hence, the areas for Eq. (3.3) are directly simulated using the open source finite element method solver, Surface Evolver [192], which essentially predicts the three-dimensional

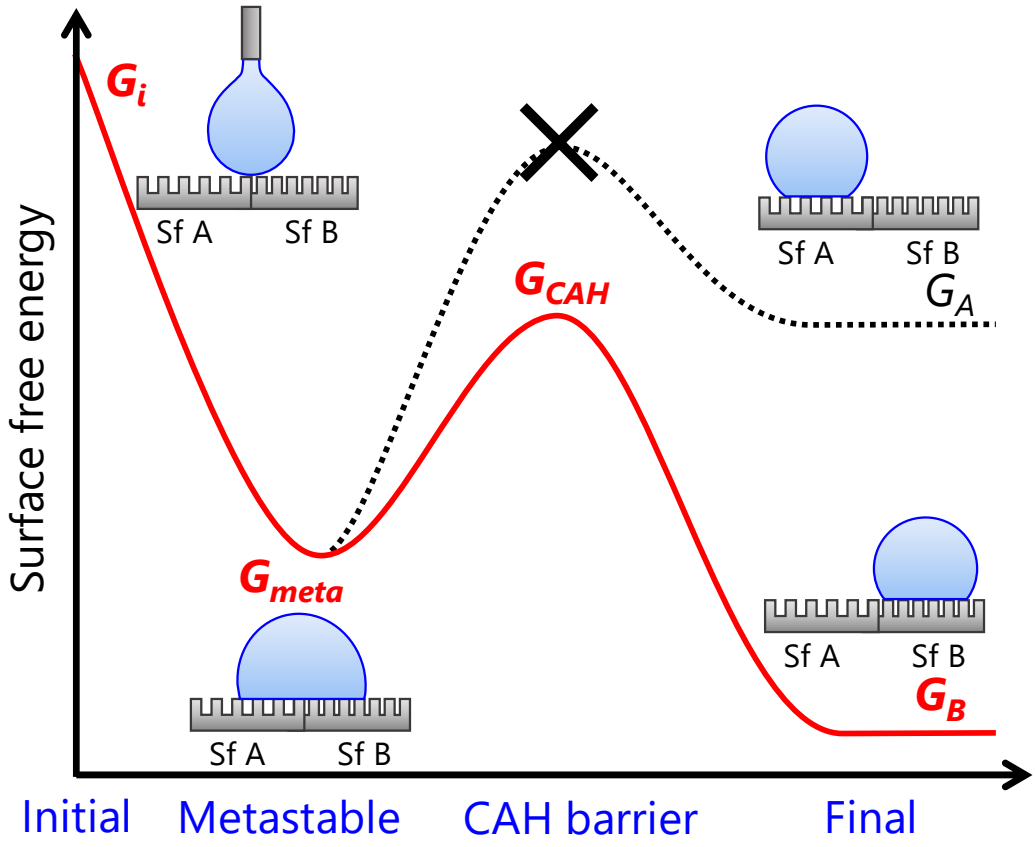

Figure 3.10 Schematic illustration of the conceptual energy diagram predicting the direction of motion for a drop at the interface between two surface, Sf A and Sf B with ϕ_A and ϕ_B ($\phi_A < \phi_B$).

shape of any drop based on the principle of energy minimisation. To account for the effect of CAH, a friction-based algorithm proposed by Santos and White [193] is incorporated, imposing the experimental contact angle values in Table 3.1.

In Figure 3.10, a schematic representation of the underlying mechanism of drop motion on wettability contrasts and the criterion for the direction. Assuming, a system that comprises Sf A and Sf B, and $\phi_A < \phi_B$, then three possible energy states arise: $G_A > G_{meta} > G_B$. Consequently, a drop placed at the interface will move in order to minimise its energy. As mentioned earlier, however, the drop must traverse the G_{CAH} peak. Therefore, $G_{ini} \geq G_{CAH}$ is required for drop motion to ensue. The direction of the motion ought to be toward the most

energetically favourable state *i.e.* G_B, which agrees with the experimental observations as presented in Figure 3.9.

3.3 Summary

In this chapter, a systematic analysis of the influence of surface wettability contrasts on drop mobility has been presented. Millimetre-sized water drops have been placed at the interface between two surfaces with different micropillar patterns (different surface area fractions ϕ) and hence different associated wettabilities. As a consequence, spontaneous motion of the drop toward the more hydrophilic (denser pillars) surfaces has been observed without any external forces. In contrast to drop motion on chemically patterned surfaces as previously reported, the drop on micropillared superhydrophobic surfaces appears to walk in an "inchworm"-like manner: it proceeds along the surface with a vertical oscillation, leading to sequential wetting and dewetting events. The displacement takes place primarily during the dewetting event in which the rear side of the drop retreats more than the front one does. The wetting event, on the other hand, contributes insensibly to the displacement since the drop spreads rather evenly.

Average drop velocity has been found to increase ($v \approx 5$–15 mm/s) as a function of differential surface area fraction ($\Delta\phi = 0.009 - 0.441$) as long as the surface on the rear side has sufficiently small contact angle hysteresis. Otherwise, the motion is retarded significantly regardless of $\Delta\phi$. It has been also noted that the pinning force that hinders any motion is not simply dependent on ϕ, but is strongly affected by the morphology and arrangement of the pillars, which should further be addressed in future.

The analysis of the surface free energy provides a universal mechanism governing drop motion on wettability contrasts based on energy minimisation.

The findings will inform the design of several future microfluidic devices used in applications such as chemical reaction and bio-sensing.

Chapter 4

Conclusions and Future Perspectives

This thesis has been entirely devoted to unveiling the long-standing question about thermocapillary effect and resultant flows in pure water drops as well as to elucidating dynamics of drops experiencing a contrast of attraction to the solid surface—wettability contrast, imposed by microtexture fabrication. For the sake of conciseness and given that comprehensive conclusions have been stated at the end of each chapter, just an overview of the fundamental findings coming out of the present study is provided in this chapter. This thesis concludes with the remaining issues left by the present study and the future outlook for further development of the field of thermocapillary phenomena, dynamic wetting and drop/surface functionalisation.

4.1 Conclusions

Controversial issues of thermocapillary or Marangoni convection in pure water has been thoroughly addressed in the first part of this thesis. While strong Marangoni flows have been observed in many liquids that are highly volatile *e.g.* organic solvents, very little experimental evidence of such flows in pure water has been previously reported. Chapter 2 has demonstrated, for the first time, visualisation of vigorous thermocapillary flows in pure water drops. The flows have been successfully induced by localised heating with a laser which produces unique and large thermal gradients across the drops. Emergence of twin vortices and their oscillatory merging/splitting behaviour have been clearly captured

using IR thermography coupled with particle visualisation. The origin of the flows has been identified as the thermocapillary or Marangoni effect by calculating the dimensionless Rayleigh and Marangoni numbers, which has been further supported by the direct experimental evidence in an inverted system.

Having proven the existence of Marangoni convection in water, a systematic analysis of the effect of local heating power and location on the flows has been conducted. The influence of heating location has been found to be paramount to the induction and evolution of thermocapillary instabilities. Heating power has clearly affected the frequency of the vortices oscillation. Moreover, local heating has been found to influence the evaporation kinetics. Top-view IR imaging has been helpful to monitor the contact line stick-slip motion. Interestingly, preferential depinning of the contact line has been observed for the edge heating cases *i.e*. the contact line moves away from the hot spot to the cold side. This contact line motion may be regarded as thermocapillary migration. Additionally, localised heating has been found to have a significant contribution to the evaporation, which has no longer been accurately predicted by the diffusion model.

These findings should contribute to understanding hydrothermal instabilities in pure water drops which have been thought to be rather unusual. Furthermore, the potential to control the internal flow of drops using the local heating technique for microfluidic mixing has been demonstrated.

The second part of this thesis has focused on drop motion induced by wettability contrasts (Chapter 3). Various wettability contrasts have been engineered using micropillar fabrication on silicon wafers, after which they were coated with a hydrophobic monolayer to attain the Cassie-Baxter wetting regime. Using such surfaces, spontaneous motion of water drops toward the surface with denser pillars has been observed without any external forces in contrast to the previous reports where mechanical vibration was required for the motion to

ensue. Drop mobility has been systematically examined and it has been found to depend on differential surface area fraction of the pillared surfaces. However, contact angle hysteresis (CAH) has been found capable of retarding the motion and CAH could be much greater than the flat surface for particular pillar patterns regardless of the Cassie-Baxter state. A thermodynamics-based surface energy analysis has revealed that the excess surface free energy in the initial state has been a source of kinetic energy, and the drop has moved toward the more hydrophilic surface for the sake of energy minimisation.

The finding will inform the design of functional drops/surfaces for several future microfluidics devices used in fields such as chemical reaction and biomedical analysis.

4.2 Future Perspectives

IR thermography has been a powerful tool for visualising thermal activities of liquid drops, which have been invaluable quantitative information to deeply understand thermally-induced fluid instabilities. The drawback of this technique may be the fact that it can only display the temperature map of an object but the fluid motion. It is important to grasp fluid dynamics in drops from both thermal and flow perspectives since they are usually linked together. Although in the present study the thermal instabilities have been corroborated by the separate optical particle imaging, the quantitative discussion both on temperature and velocity fields have not yet been made completely. Once they (thermal and flow behaviour) match, we could further approach the comprehensive understanding of fluid dynamics, stability and heat transfer and it would probably lead to significant progress in computational fluid dynamics.

As demonstrated in this thesis, use of Marangoni flows for drop mixing seems quite promising. To further develop this field, more comprehensive investigations are needed for many influential parameters such as contact angle,

chemical component and heating mode (heat flux- or temperature-controlled). As for local heating method, besides laser irradiation, microheater arrays are another candidate for practical applications, capable of switching heating power (or temperature) as well as location [194].

The interesting phenomenon of contact line depinning under local heating could be a critical issue for evaporative cooling applications. Heating-induced preferential depinning of the contact line may lead to early dry out as imposed thermocapillary forces act such that the liquid moves away from the hot spot. Such localised heating spot can be found in CPUs which must be kept under a certain temperature limit during operation. Potentially, knowing what enhances or hinders the thermocapillary-driven contact line motion, perhaps such as wettability and surface roughness could improve cooling surfaces on which phase change heat transfer takes place.

As for wetting dynamics, the present work has focused only on the induction of drop motion by a wettability contrast. In order for a drop to travel a longer distance, one may extend the surface *i.e*. step-wisely graded wettability. The longer the drop walks toward more hydrophilic surfaces, however, the more comfortable (in other words, lazier to move) the drop feels. Also the effect of contact angle hysteresis (CAH) becomes prominent. As pointed out in the present and previous study, although the Cassie-Baxter (CB) superhydrophobic surfaces are often regarded as non-sticky surfaces, it can be very sticky for specific pillar arrangements and the mechanism of CAH arising by pillars has been an intensive research topic recently [180]–[182].

In the experiments, initial surface energy required for drop motion has been accumulated during drop deposition. Such excessive surface energy can also be attained by mechanical vibration or drop coalescence. In fact, coalescence-induced droplet jumping is a very similar phenomenon with drop motion observed in this study. Daniel *et al*. [143] experimentally reported coalescing

condensate droplets moving along a wettability gradient instead of jumping. Not only that it could vastly improve dropwise condensation performance, it could also provide a clue to make use of such wettability gradients for liquid collecting applications such as water/fog/mist harvesting [195], [196]. It should be noted, however, that microtexture gradient surfaces may not be applicable particularly to this field as condensation normally occurs in the asperities and they eventually flood, exhibiting the Wenzel regime with extremely low mobility. Nevertheless, the drop motion mechanism based on surface energy minimisation as presented in this thesis should be valid for any capillary-driven drop motion on heterogeneous wettability surfaces.

Appendix

A.1. Supplemental Data for Chapter 3

A.1.1. Contact point behaviour

Herein, the data from the rest of the experiments conducted in Chapter 3 are presented. Figure A 1 shows the displacements of the contact points (front – red, middle – green and rear – blue) along representative snapshots, similar to Figure 3.4. As reported in subsection 3.2.1, sequential wetting/dewetting events of the drops are observed for every case and the drops proceed to the surfaces with larger ϕ—lower θ_{app} mainly during the dewetting events. For the wettability interfaces with relatively small $\Delta\phi$ *i.e.* Figure A 1 (a)–(c), during the dewetting events both front and rear contact points retreat significantly, although front one moves less, resulting in small displacements during each event. In contrast, the cases depicted in the panels (d)–(g) in Figure A 1, exhibit wettability interfaces with large $\Delta\phi$ and closely resemble the Sq-10-40/Sq-10-20 case shown in Figure 3.4 in Chapter 3. In particular, the front contact point is almost pinned during the dewetting events, giving rise to large velocities. If both sides of the interfaces rest on large ϕ surfaces shown in Figure A 1 (h)–(i) within the red box, motion of the contact points is weak and both sides are nearly pinned after the first wetting event, which results in a significantly slower drop velocity corresponding to the red-boxed data in Figure 3.5.

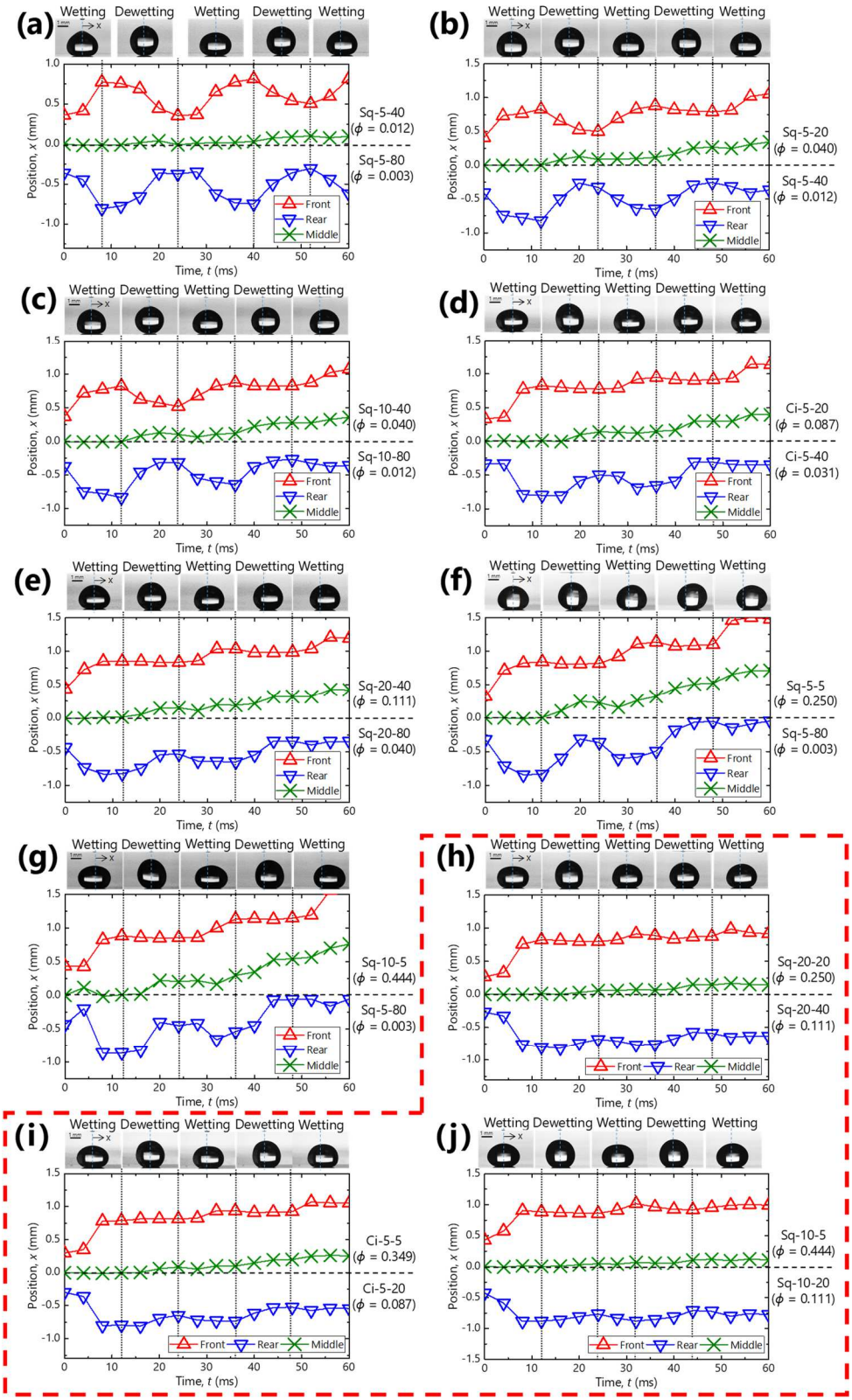

Figure A 1 Evolution of each contact point (front, rear and middle) over time for the cases of (a) Sq-5-80/Sq-5-40, (b) Sq-5-40/Sq-5-20, (c) Sq-10-80/Sq-10-40, (d) Ci-5-40/Ci-5-20, (e) Sq-20-80/Sq-20-40, (f) Sq-5-80/Sq-5-5, (g) Sq-5-80/Sq-10-5, (h) Sq-20-40/Sq-20-20, (i) Ci-5-20/Ci-5-5 and (j) Sq-10-20/Sq-10-5. The position of the interface is set as x = 0 mm. Insets represent typical drop shape during wetting and dewetting events.

A.1.2. Surface free energy and energy diagram

Figure A 2 presents the calculated free energy evolution over time in the left column and the corresponding quantification of the energy requirements for motion for each case above in the right column.

In every case, the drops minimise their energy and move toward the surfaces with lower energy as discussed in subsection 3.2.4. The cases of Figure A 2 (h)–(j) show significantly smaller drop velocities as in Figure 3.5, due to the fact that the drops at the wettability interfaces (metastable) must traverse very high peaks of G_{CAH} compared to other cases. Hence, it can be stipulated at this point that large portion of G_{ini} was consumed to overcome the CAH, retarding motion.

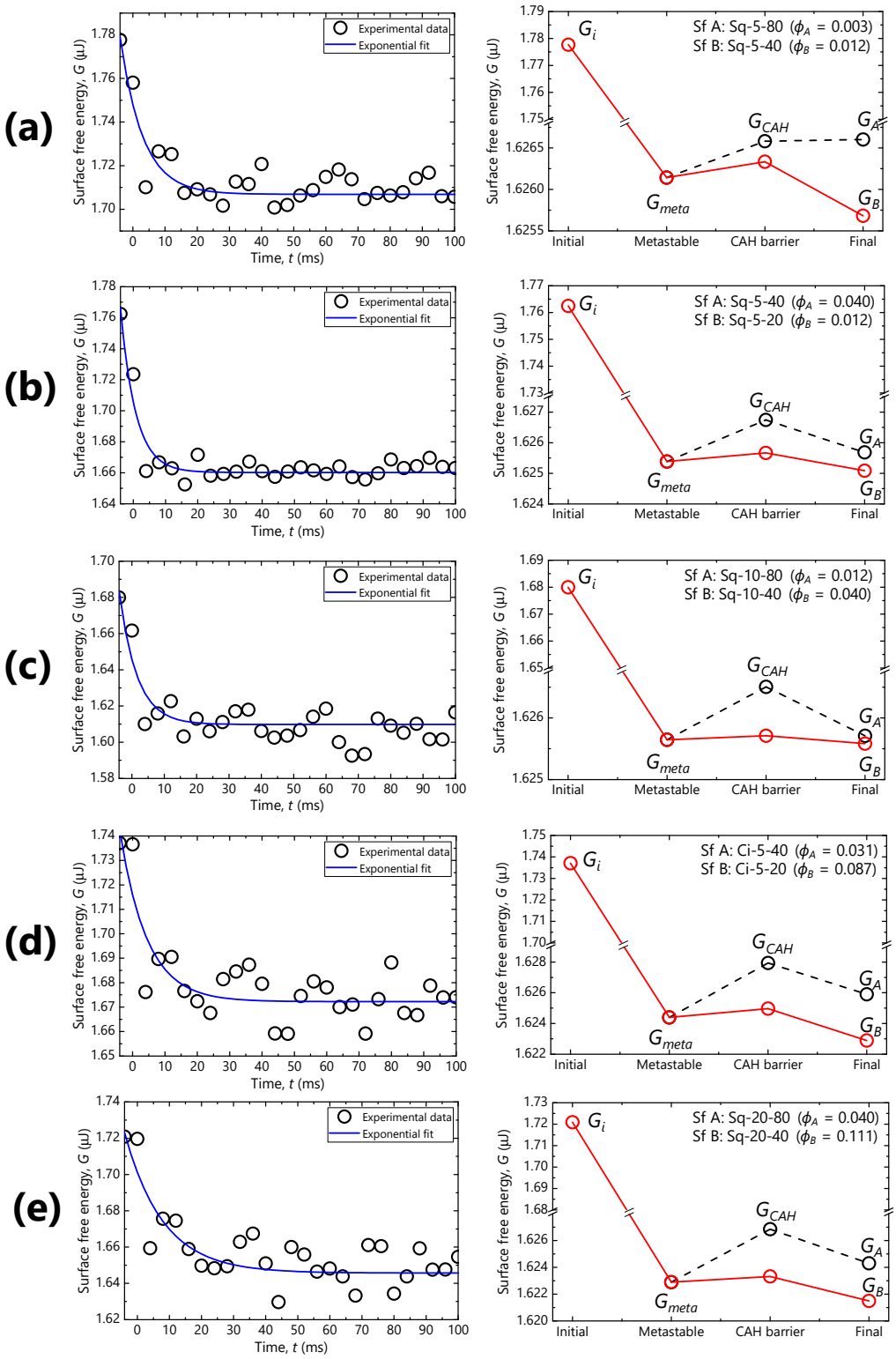

Figure A 2 Evolution over time of the surface free energy of a drop placed at the interfaces (left column) and energy diagrams (right column) for (a) Sq-5-80/Sq-5-40, (b) Sq-5-40/Sq-5-20, (c) Sq-10-80/Sq-10-40, (d) Ci-5-40/Ci-5-20, (e) Sq-20-80/Sq-20-40, (f) Sq-5-80/Sq-5-5, (g) Sq-5-80/Sq-10-5, (h) Sq-20-40/Sq-20-20, (i) Ci-5-20/Ci-5-5 and (j) Sq-10-20/Sq-10-5. The cases for slow drops corresponding to Figure 3.5 are indicated in the red box.

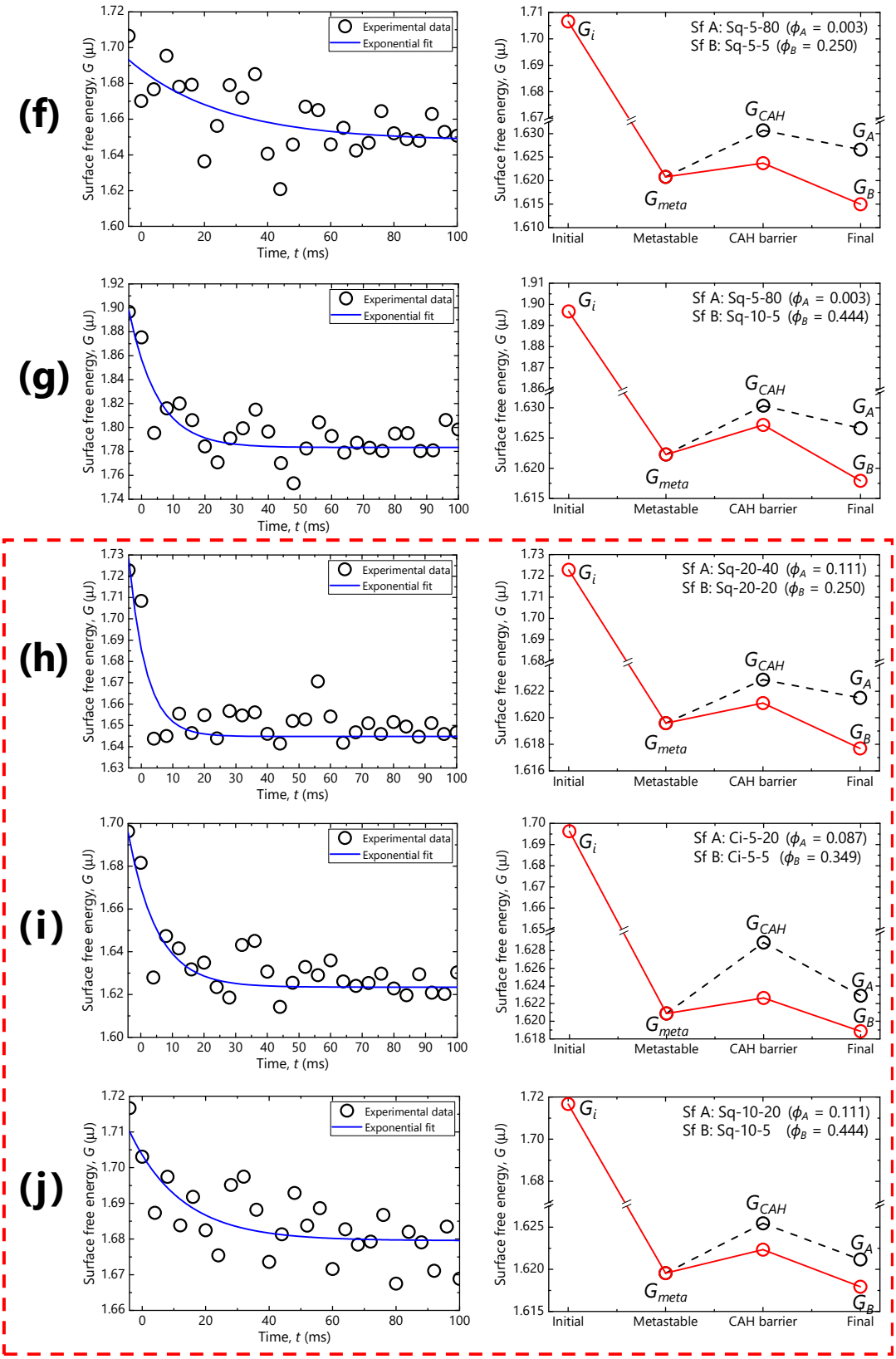

Figure A 2 Continued.

List of Publications

Journals

Drop mobility on superhydrophobic microstructured surfaces with wettability contrasts,
Yutaku Kita, Coinneach MacKenzie-Dover, Alexandros Askounis,
Yasuyuki Takata and Khellil Sefiane,
ACS Applied Materials & Interfaces, in peer review, **2018**.

Quantifying vapor transfer into evaporating ethanol drops in a humid atmosphere,
Yutaku Kita, Yuya Okauchi, Yuki Fuakatani, Daniel Orejon, Masamichi Kohno,
Yasuyuki Takata and Khellil Sefiane,
Physical Chemistry Chemical Physics, 20 (29), 19430–19440, **2018**.

Influence of local heating on Marangoni flows and evaporation kinetics of pure water drops,
Alexandros Askounis, **Yutaku Kita**, Masamichi Kohno, Yasuyuki Takata, Vasileios Koutsos and Khellil Sefiane,
Langmuir, 33 (23), 5666–5674, **2017**.

Induction of Marangoni convection in pure water drops,
Yutaku Kita, Alexandros Askounis, Masamichi Kohno, Yasuyuki Takata,
Jungho Kim and Khellil Sefiane,
Applied Physics Letters, 109 (17), 171602, **2016**.

Performance improvement of a falling-film-type heat exchanger by insertion of shafts with screw blade in a heat exchanger tube,
Hiroyuki Shiraiwa and **Yutaku Kita**
Applied Thermal Engineering, 102, 55-62, **2016**.

Effect of ambient temperature and relative humidity on interfacial temperature during early stages of drop evaporation,
Yuki Fukatani, Daniel Orejon, **Yutaku Kita**, Yasuyuki Takata, Jungho Kim, and Khellil Sefiane,
Physical Review E, 93 (4), 043103, **2016**.

Heat transfer characteristics of falling-film-type heat exchanger (in Japanese),
Hiroyuki Shiraiwa and **Yutaku Kita**,
Transactions of the Society of Heating, Air-conditioning and Sanitary Engineers of Japan, 39 (202), 23–28, **2014**.

International Conferences

Drop mobility on superhydrophobic surfaces with wettability contrasts,
Yutaku Kita, Coinneach MacKenzie-Dover, Alexandros Askounis,
Yasuyuki Takata and Khellil Sefiane,
The 16th International Heat Transfer Conference (IHTC-16), Beijing, China, 10–15th August, **2018**.

Influence of localised heating on thermocapillary convection in pure water drops,
Alexandros Askounis, Huacheng Zhang, Dejian Zhang, **Yutaku Kita**,
Gyoko Nagayama, Jungho Kim, Masamichi Kohno, Yasuyuki Takata,
and Khellil Sefiane,
The 16th International Heat Transfer Conference (IHTC-16), Beijing, China, 10–15th August, **2018**.

Drop propelled by wettability contrasts on microtextured surfaces,
Yutaku Kita, Coinneach MacKenzie-Dover, Alexandros Askounis,
Yasuyuki Takata and Khellil Sefiane,
The 10th International Conference on Boiling and Condensation Heat Transfer (ICBCHT2018), Nagasaki, Japan, 12–15th March, **2018**.

Thermal/flow visualisation of flows in water drops induced by a microheater,
Yutaku Kita, Alexandros Askounis, Yasuyuki Takata, John R. E. Christy,
Khellil Sefiane and Jungho Kim,
The 15th UK Heat Transfer Conference (UKHTC2017), London, United Kingdom, 4–5th September, **2017**.

Do Marangoni flows exist in pure water drops?
Alexandros Askounis, **Yutaku Kita**, Yasuyuki Takata, Masamichi Kohno, Jungho Kim, Vasileios Koutsos and Khellil Sefiane,
The 15th UK Heat Transfer Conference (UKHTC2017), London, United Kingdom, 4–5th September, **2017**.

Induction/manipulation of thermocapillary-driven convection in water drops,
Yutaku Kita, Alexandros Askounis, Masamichi Kohno, Yasuyuki Takata, Khellil Sefiane and Jungho Kim,
Gordon Research Conference on Micro & Nanoscale Phase Change Heat Transfer, Galveston, Texas, United States, 8–13th January, **2017**.

Influence of relative humidity and ambient temperature on hydrothermal waves (HTWs) of organic solvent volatile droplets,
Daniel Orejon, **Yutaku Kita**, Yuya Okauchi, Yuki Fukatani, Masamichi Kohno, Yasuyuki Takata, Khellil Sefiane and Jungho Kim,
The 69th Annual Meeting of the APS Division of Fluid Dynamics, Portland, Oregon, United States, 20–22nd November, **2016**.

Condensation of water vapour onto evaporating volatile droplets,
Yutaku Kita, Yuya Okauchi, Daniel Orejon, Masamichi Kohno, Yasuyuki Takata, Jungho Kim and Khellil Sefiane,
The 7th European Thermal-Science Conference (EUROTHERM 2016), Krakow, Poland, 19–23rd June, **2016**.

Thermocapillary flows in water droplets induced by laser irradiation,
Yutaku Kita, Alexandros Askounis, Masamichi Kohno, Yasuyuki Takata, Khellil Sefiane and Jungho Kim,
The First Pacific Rim Thermal Engineering Conference (PRTEC-2016), Hawaii's Big Island, United States, 13–17th March, **2016**.

Effect of ambient temperature and relative humidity on hydrothermal waves (HTWs) of volatile drops,
Yuki Fukatani, Daniel Orejon, **Yutaku Kita**, Yasuyuki Takata, Jungho Kim, and Khellil Sefiane,

The First Pacific Rim Thermal Engineering Conference (PRTEC-2016), Hawaii's Big Island, United States, 13–17th March, **2016**.

Effect of ambient temperature and relative humidity on evaporating droplets,
Yutaku Kita, Yuki Fukatani, Daniel Orejon, Masamichi Kohno, Yasuyuki Takata, Khelli Sefiane and Jungho Kim,
The 3rd International Workshop on Heat Transfer Advances for Energy Conservation and Pollution Control (IWHT 2015), Taipei, Taiwan, 16–19th October, **2015**.

Study on heat transfer characteristics of falling film type heat exchanger (Effect of tube flow condition on heat exchange performance),
Yutaku Kita and Hiroyuki Shiraiwa,
The 8th International Symposium on Advanced Science and Technology in Experimental Mechanics (8th ISEM), Sendai, Japan, 3–6th November, **2013**.

List of Figures

List of Tables

References

[1] R. D. Deegan, Pattern formation in drying drops, *Physical Review E*, 61 (1), 475–485, 2000.

[2] T. Young, An essay on the cohesion of fluids, *Philosophical Transactions of the Royal Society of London*, 95, 65–87, 1805.

[3] J. C. Maxwell, *The scientific papers of James Clerk Maxwell*. Cambridge: Cambridge University Press, 1890.

[4] K. Sefiane, Patterns from drying drops, *Advances in Colloid and Interface Science*, 206, 372–381, 2014.

[5] T. Lim, S. Han, J. Chung, J. T. Chung, S. Ko, and C. P. Grigoropoulos, Experimental study on spreading and evaporation of inkjet printed pico-liter droplet on a heated substrate, *International Journal of Heat and Mass Transfer*, 52 (1–2), 431–441, 2009.

[6] M. Singh, H. M. Haverinen, P. Dhagat, and G. E. Jabbour, Inkjet printing-Process and its applications, *Advanced Materials*, 22 (6), 673–685, 2010.

[7] A. K. Thokchom, Q. Zhou, D.-J. Kim, D. Ha, and T. Kim, Characterizing self-assembly and deposition behavior of nanoparticles in inkjet-printed evaporating droplets, *Sensors and Actuators B: Chemical*, 252, 1063–1070, 2017.

[8] M. Mikolajek, T. Reinheimer, M. Muth, P. Hohwieler, M. J. Hoffmann, and J. R. Binder, Control of the surface morphology of ceramic/polymer composite inks for inkjet printing, *Advanced Engineering Materials*, 1800318, 2018.

[9] B.-J. De Gans and U. S. Schubert, Inkjet printing of well-defined polymer dots and arrays, *Langmuir*, 20 (18), 7789–7793, 2004.

[10] B.-J. de Gans, P. C. Duineveld, and U. S. Schubert, Inkjet printing of polymers: State of the art and future developments, *Advanced Materials*, 16

(3), 203–213, 2004.

[11] O. D. Velev, A. M. Lenhoff, and E. W. Kaler, A class of microstructured particles through colloidal crystallization, *Science*, 287 (5461), 2240–2243, 2000.

[12] R. M. Michell and A. J. Müller, Confined crystallization of polymeric materials, *Progress in Polymer Science*, 54–55, 183–213, 2016.

[13] H. Y. Erbil, Evaporation of pure liquid sessile and spherical suspended drops: A review, *Advances in Colloid and Interface Science*, 170 (1–2), 67–86, 2012.

[14] M. Schena, D. Shalon, R. W. Davis, and P. O. Brown, Quantitative monitoring of gene expression patterns with a complementary DNA microarray., *Science*, 270 (5235), 467–470, 1995.

[15] K. Sefiane, On the formation of regular patterns from drying droplets and their potential use for bio-medical applications, *Journal of Bionic Engineering*, 7 (Supplement), S82–S93, 2010.

[16] D. Brutin, B. Sobac, B. Loquet, and J. Sampol, Pattern formation in drying drops of blood, *Journal of Fluid Mechanics*, 667, 85–95, 2011.

[17] F. R. Smith and D. Brutin, Wetting and spreading of human blood: Recent advances and applications, *Current Opinion in Colloid & Interface Science*, 36, 78–83, 2018.

[18] S.-Y. Teh, R. Lin, L.-H. Hung, and A. P. Lee, Droplet microfluidics, *Lab on a Chip*, 8 (2), 198–220, 2008.

[19] M. Abdelgawad and A. R. Wheeler, The digital revolution: A new paradigm for microfluidics, *Advanced Materials*, 21 (8), 920–925, 2009.

[20] B. Kintses, L. D. van Vliet, S. R. A. Devenish, and F. Hollfelder, Microfluidic droplets: New integrated workflows for biological experiments, *Current Opinion in Chemical Biology*, 14 (5), 548–555, 2010.

[21] K. Choi, A. H. C. Ng, R. Fobel, and A. R. Wheeler, Digital microfluidics,

Annual Review of Analytical Chemistry, 5 (1), 413–440, 2012.

[22] R. Seemann, M. Brinkmann, T. Pfohl, and S. Herminghaus, Droplet based microfluidics, *Reports on Progress in Physics*, 75 (1), 016601, 2012.

[23] N. A. Mousa *et al.*, Droplet-scale estrogen assays in breast tissue, blood, and serum, *Science Translational Medicine*, 1 (1), 1ra2, 2009.

[24] M. J. Jebrail and A. R. Wheeler, Let's get digital: digitizing chemical biology with microfluidics, *Current Opinion in Chemical Biology*, 14 (5), 574–581, 2010.

[25] P.-G. de Gennes, F. Brochard-Wyart, and D. Quéré, *Capillarity and wetting phenomena*. New York, NY: Springer New York, 2004.

[26] J. W. Gibbs, On the equilibrium of heterogeneous substances, *Transactions of the Connecticut Academy of Arts and Sciences*, 3, 108-248 and 343-524, 1878.

[27] A. Einstein, Folgerungen aus den Capillaritätserscheinungen, *Annalen der Physik*, 309 (3), 513–523, 1901.

[28] P. G. de Gennes, Wetting: statics and dynamics, *Reviews of Modern Physics*, 57 (3), 827–863, 1985.

[29] J. Thomson, XLII. On certain curious motions observable at the surfaces of wine and other alcoholic liquors, *The London, Edinburgh, and Dublin Philosophical Magazine and Journal of Science*, 10 (67), 330–333, 1855.

[30] C. Marangoni, Sull'espansione delle goccie d'un liquido galleggianti sulla superfice di altro liquido, Pavia, 1865.

[31] R. Savino and S. Fico, Transient Marangoni convection in hanging evaporating drops, *Physics of Fluids*, 16 (10), 3738–3754, 2004.

[32] H. Hu and R. G. Larson, Marangoni effect reverses coffee-ring depositions, *Journal of Physical Chemistry B*, 110 (14), 7090–7094, 2006.

[33] K. Sefiane, J. R. Moffat, O. K. Matar, and R. V. Craster, Self-excited hydrothermal waves in evaporating sessile drops, *Applied Physics Letters*, 93 (7), 074103, 2008.

[34] R. D. Deegan, O. Bakajin, T. F. Dupont, G. Huber, S. R. Nagel, and T. a

Witten, Capillary flow as the cause of ring stains from dried liquid drops, *Nature*, 389 (6653), 827–829, 1997.

[35] X. Xu and J. Luo, Marangoni flow in an evaporating water droplet, *Applied Physics Letters*, 91 (12), 124102, 2007.

[36] I. Thompson, F. Duan, and C. A. Ward, Absence of Marangoni convection at Marangoni numbers above 27,000 during water evaporation, *Physical Review E*, 80 (5), 056308, 2009.

[37] D. Brutin, B. Sobac, F. Rigollet, and C. Le Niliot, Infrared visualization of thermal motion inside a sessile drop deposited onto a heated surface, *Experimental Thermal and Fluid Science*, 35 (3), 521–530, 2011.

[38] F. Brochard, Motions of droplets on solid surfaces induced by chemical or thermal gradients, *Langmuir*, 5 (2), 432–438, 1989.

[39] M. K. Chaudhury and G. M. Whitesides, How to make water run uphill, *Science*, 256 (5063), 1539–1541, 1992.

[40] J. B. Brzoska, F. Brochard-Wyart, and F. Rondelez, Motions of droplets on hydrophobic model surfaces induced by thermal gradients, *Langmuir*, 9 (8), 2220–2224, 1993.

[41] R. S. Subramanian, N. Moumen, and J. B. McLaughlin, Motion of a drop on a solid surface due to a wettability gradient, *Langmuir*, 21 (25), 11844–11849, 2005.

[42] N. Bjelobrk, H.-L. Girard, S. Bengaluru Subramanyam, H.-M. Kwon, D. Quéré, and K. K. Varanasi, Thermocapillary motion on lubricant-impregnated surfaces, *Physical Review Fluids*, 1 (6), 063902, 2016.

[43] A. R. Parker and C. R. Lawrence, Water capture by a desert beetle, *Nature*, 414 (6859), 33–34, 2001.

[44] Y. Zheng *et al.*, Directional water collection on wetted spider silk, *Nature*, 463 (7281), 640–643, 2010.

[45] M. Liu, S. Wang, and L. Jiang, Nature-inspired superwettability systems,

Nature Reviews Materials, 2 (7), 17036, 2017.

[46] G. Barnes and I. Gentle, *Interfacial science: An introduction*. Oxford University Press, 2011.

[47] D. Brutin, *Droplet wetting and evaporation from pure to complex fluids*, 1st ed. Academic Press, 2015.

[48] A. Dupré and P. Dupré, *Théorie mécanique de la chaleur*. Gauthier-Villars (Paris), 1869.

[49] R. N. Wenzel, Resistance of solid surfaces to wetting by water, *Industrial & Engineering Chemistry*, 28 (8), 988–994, 1936.

[50] A. B. D. Cassie and S. Baxter, Wettability of porous surfaces, *Transactions of the Faraday Society*, 40, 546–551, 1944.

[51] L. Mahadevan, Non-stick water, *Nature*, 411 (6840), 895–896, 2001.

[52] D. Quéré, Surface chemistry: Fakir droplets, *Nature Materials*, 1 (1), 14–15, 2002.

[53] Y. Y. Yan, N. Gao, and W. Barthlott, Mimicking natural superhydrophobic surfaces and grasping the wetting process: A review on recent progress in preparing superhydrophobic surfaces, *Advances in Colloid and Interface Science*, 169 (2), 80–105, 2011.

[54] X. J. Feng and L. Jiang, Design and creation of superwetting/antiwetting surfaces, *Advanced Materials*, 18 (23), 3063–3078, 2006.

[55] Y. Kwon, N. Patankar, J. Choi, and J. Lee, Design of surface hierarchy for extreme hydrophobicity, *Langmuir*, 25 (11), 6129–6136, 2009.

[56] E. Atefi, J. A. Mann, and H. Tavana, A robust polynomial fitting approach for contact angle measurements, *Langmuir*, 29 (19), 5677–5688, 2013.

[57] S. M. I. Saad and A. W. Neumann, Axisymmetric drop shape analysis (ADSA): An outline, *Advances in Colloid and Interface Science*, 238, 62–87, 2016.

[58] A. F. Stalder, T. Melchior, M. Müller, D. Sage, T. Blu, and M. Unser, Low-

bond axisymmetric drop shape analysis for surface tension and contact angle measurements of sessile drops, *Colloids and Surfaces A: Physicochemical and Engineering Aspects*, 364 (1–3), 72–81, 2010.

[59] I. Langmuir, The evaporation of small spheres, *Physical Review*, 12 (5), 368–370, 1918.

[60] J. M. Stauber, S. K. Wilson, B. R. Duffy, and K. Sefiane, Evaporation of droplets on strongly hydrophobic substrates, *Langmuir*, 31 (12), 3653–3660, 2015.

[61] R. G. Picknett and R. Bexon, The evaporation of sessile or pendant drops in still air, *Journal of Colloid and Interface Science*, 61 (2), 336–350, 1977.

[62] H. Hu and R. G. Larson, Evaporation of a sessile droplet on a substrate, *Journal of Physical Chemistry B*, 106 (6), 1334–1344, 2002.

[63] Y. O. Popov, Evaporative deposition patterns: Spatial dimensions of the deposit, *Physical Review E*, 71 (3), 036313, 2005.

[64] C. Bourgès-Monnier and M. E. R. Shanahan, Influence of evaporation on contact angle, *Langmuir*, 11 (7), 2820–2829, 1995.

[65] S. Dash and S. V. Garimella, Droplet evaporation dynamics on a superhydrophobic surface with negligible hysteresis, *Langmuir*, 29 (34), 10785–10795, 2013.

[66] J. M. Stauber, S. K. Wilson, B. R. Duffy, and K. Sefiane, On the lifetimes of evaporating droplets with related initial and receding contact angles, *Physics of Fluids*, 27 (12), 122101, 2015.

[67] S. David, K. Sefiane, and L. Tadrist, Experimental investigation of the effect of thermal properties of the substrate in the wetting and evaporation of sessile drops, *Colloids and Surfaces A: Physicochemical and Engineering Aspects*, 298 (1–2), 108–114, 2007.

[68] G. J. Dunn, S. K. Wilson, B. R. Duffy, S. David, and K. Sefiane, The strong influence of substrate conductivity on droplet evaporation, *Journal of Fluid*

Mechanics, 623, 329, 2009.

[69] M. C. Lopes, E. Bonaccurso, T. Gambaryan-Roisman, and P. Stephan, Influence of the substrate thermal properties on sessile droplet evaporation: Effect of transient heat transport, *Colloids and Surfaces A: Physicochemical and Engineering Aspects*, 432, 64–70, 2013.

[70] B. Sobac and D. Brutin, Thermal effects of the substrate on water droplet evaporation, *Physical Review E*, 86 (2), 021602, 2012.

[71] E. F. Crafton and W. Z. Black, Heat transfer and evaporation rates of small liquid droplets on heated horizontal surfaces, *International Journal of Heat and Mass Transfer*, 47 (6–7), 1187–1200, 2004.

[72] F. Girard, M. Antoni, and K. Sefiane, On the effect of Marangoni flow on evaporation rates of heated water drops, *Langmuir*, 24 (17), 9207–9210, 2008.

[73] N. D. Patil, P. G. Bange, R. Bhardwaj, and A. Sharma, Effects of substrate heating and wettability on evaporation dynamics and deposition patterns for a sessile water droplet containing colloidal particles, *Langmuir*, 32 (45), 11958–11972, 2016.

[74] O. E. Ruiz and W. Z. Black, Evaporation of water droplets placed on a heated horizontal surface, *Journal of Heat Transfer*, 124 (5), 854–863, 2002.

[75] P. L. Kelly-Zion, C. J. Pursell, S. Vaidya, and J. Batra, Evaporation of sessile drops under combined diffusion and natural convection, *Colloids and Surfaces A: Physicochemical and Engineering Aspects*, 381 (1–3), 31–36, 2011.

[76] F. Carle, S. Semenov, M. Medale, and D. Brutin, Contribution of convective transport to evaporation of sessile droplets: Empirical model, *International Journal of Thermal Sciences*, 101, 35–47, 2016.

[77] K. Sefiane, L. Tadrist, and M. Douglas, Experimental study of evaporating water-ethanol mixture sessile drop: Influence of concentration, *International Journal of Heat and Mass Transfer*, 46 (23), 4527–4534, 2003.

[78] P. Chen, M. Toubal, J. Carlier, S. Harmand, B. Nongaillard, and M. Bigerelle,

Evaporation of binary sessile drops: Infrared and acoustic methods to track alcohol concentration at the interface and on the surface, *Langmuir*, 32 (38), 9836–9845, 2016.

[79] Y. Fukatani, D. Orejon, Y. Kita, Y. Takata, J. Kim, and K. Sefiane, Effect of ambient temperature and relative humidity on interfacial temperature during early stages of drop evaporation, *Physical Review E*, 93 (4), 043103, 2016.

[80] Y. Kita *et al.*, Quantifying vapor transfer into evaporating ethanol drops in a humid atmosphere, *Physical Chemistry Chemical Physics*, 20 (29), 19430–19440, 2018.

[81] H. Kim, F. Boulogne, E. Um, I. Jacobi, E. Button, and H. A. Stone, Controlled uniform coating from the interplay of Marangoni flows and surface-adsorbed macromolecules, *Physical Review Letters*, 116 (12), 124501, 2016.

[82] P. O. Babatunde, W. J. Hong, K. Nakaso, and J. Fukai, Effect of solute- and solvent-derived Marangoni flows on the shape of polymer films formed from drying droplets, *AIChE Journal*, 59 (3), 699–702, 2013.

[83] X. Fang *et al.*, Drying of DNA droplets, *Langmuir*, 22 (14), 6308–6312, 2006.

[84] W. Wang, J. Lin, and D. C. Schwartz, Scanning force microscopy of DNA molecules elongated by convective fluid flow in an evaporating droplet, *Biophysical Journal*, 75 (1), 513–520, 1998.

[85] E. Z. Macosko *et al.*, Highly parallel genome-wide expression profiling of individual cells using nanoliter droplets., *Cell*, 161 (5), 1202–1214, 2015.

[86] P. O. Brown and D. Botstein, Exploring the new world of the genome with DNA microarrays, *Nature Genetics*, 21 (1s), 33–37, 1999.

[87] A. Askounis, Y. Takata, K. Sefiane, V. Koutsos, and M. E. R. Shanahan, "Biodrop" evaporation and ring-stain deposits: The significance of DNA length, *Langmuir*, 32 (17), 4361–4369, 2016.

[88] A. Askounis, K. Sefiane, V. Koutsos, and M. E. R. Shanahan, Structural transitions in a ring stain created at the contact line of evaporating nanosuspension sessile drops, *Physical Review E*, 87 (1), 012301, 2013.

[89] W. Han and Z. Lin, Learning from "coffee rings": Ordered structures enabled by controlled evaporative self-assembly, *Angewandte Chemie International Edition*, 51 (7), 1534–1546, 2012.

[90] Y. Cai and B. Zhang Newby, Marangoni flow-induced self-assembly of hexagonal and stripelike nanoparticle patterns, *Journal of the American Chemical Society*, 130 (19), 6076–6077, 2008.

[91] C. N. Baroud, F. Gallaire, and R. Dangla, Dynamics of microfluidic droplets, *Lab on a Chip*, 10 (16), 2032–2045, 2010.

[92] K. T. Kotz, K. a. Noble, and G. W. Faris, Optical microfluidics, *Applied Physics Letters*, 85 (13), 2658–2660, 2004.

[93] T. M. Squires and S. R. Quake, Microfluidics: Fluid physics at the nanoliter scale, *Reviews of Modern Physics*, 77 (3), 977–1026, 2005.

[94] J. D. Tice, H. Song, A. D. Lyon, and R. F. Ismagilov, Formation of droplets and mixing in multiphase microfluidics at low values of the Reynolds and the capillary numbers, *Langmuir*, 19 (22), 9127–9133, 2003.

[95] S. Dash, A. Chandramohan, J. a. Weibel, and S. V. Garimella, Buoyancy-induced on-the-spot mixing in droplets evaporating on nonwetting surfaces, *Physical Review E*, 90 (6), 062407, 2014.

[96] J. D. Tice, A. D. Lyon, and R. F. Ismagilov, Effects of viscosity on droplet formation and mixing in microfluidic channels, *Analytica Chimica Acta*, 507 (1), 73–77, 2004.

[97] P. J. Yunker, T. Still, M. a Lohr, and a G. Yodh, Suppression of the coffee-ring effect by shape-dependent capillary interactions., *Nature*, 476 (7360), 308–311, 2011.

[98] A. Askounis, K. Sefiane, V. Koutsos, and M. E. R. Shanahan, Effect of

particle geometry on triple line motion of nano-fluid drops and deposit nano-structuring, *Advances in Colloid and Interface Science*, 222, 44–57, 2015.

[99] Y. Ooi, I. Hanasaki, D. Mizumura, and Y. Matsuda, Suppressing the coffee-ring effect of colloidal droplets by dispersed cellulose nanofibers, *Science and Technology of Advanced Materials*, 18 (1), 316–324, 2017.

[100] Y. F. Li, Y. J. Sheng, and H. K. Tsao, Evaporation stains: Suppressing the coffee-ring effect by contact angle hysteresis, *Langmuir*, 29 (25), 7802–7811, 2013.

[101] H. B. Eral, D. M. Augustine, M. H. G. Duits, and F. Mugele, Suppressing the coffee stain effect: how to control colloidal self-assembly in evaporating drops using electrowetting, *Soft Matter*, 7 (10), 4954–4958, 2011.

[102] D. Mampallil, J. Reboud, R. Wilson, D. Wylie, D. R. Klug, and J. M. Cooper, Acoustic suppression of the coffee-ring effect, *Soft Matter*, 11 (36), 7207–7213, 2015.

[103] R. Mollaret, K. Sefiane, J. R. E. Christy, and D. Veyret, Experimental and numerical investigation of the evaporation into air of a drop on a heated surface, *Chemical Engineering Research and Design*, 82 (4), 471–480, 2004.

[104] H. Hu and R. G. Larson, Analysis of the effects of marangoni stresses on the microflow in an evaporating sessile droplet, *Langmuir*, 21 (9), 3972–3980, 2005.

[105] K. Yang, F. Hong, and P. Cheng, A fully coupled numerical simulation of sessile droplet evaporation using Arbitrary Lagrangian–Eulerian formulation, *International Journal of Heat and Mass Transfer*, 70, 409–420, 2014.

[106] K. H. Kang, H. C. Lim, H. W. Lee, and S. J. Lee, Evaporation-induced saline Rayleigh convection inside a colloidal droplet, *Physics of Fluids*, 25 (4), 042001, 2013.

[107] Z. Pan, S. Dash, J. A. Weibel, and S. V. Garimella, Assessment of water

droplet evaporation mechanisms on hydrophobic and superhydrophobic substrates, *Langmuir*, 29 (51), 15831–15841, 2013.

[108] T. K. Pradhan and P. K. Panigrahi, Evaporation induced natural convection inside a droplet of aqueous solution placed on a superhydrophobic surface, *Colloids and Surfaces A: Physicochemical and Engineering Aspects*, 530, 1–12, 2017.

[109] J. R. A. Pearson, On convection cells induced by surface tension, *Journal of Fluid Mechanics*, 4 (5), 489–500, 1958.

[110] A. Chandramohan, S. Dash, J. A. Weibel, X. Chen, and S. V. Garimella, Marangoni convection in evaporating organic liquid droplets on a nonwetting substrate, *Langmuir*, 32 (19), 4729–4735, 2016.

[111] M. K. Smith and S. H. Davis, Instabilities of dynamic thermocapillary liquid layers. Part 2. Surface-wave instabilities, *Journal of Fluid Mechanics*, 132, 119–144, 1983.

[112] R. J. Riley and G. P. Neitzel, Instability of thermocapillary–buoyancy convection in shallow layers. Part 1. Characterization of steady and oscillatory instabilities, *Journal of Fluid Mechanics*, 359, 143–164, 1998.

[113] D. Schwabe, U. Möller, J. Schneider, and A. Scharmann, Instabilities of shallow dynamic thermocapillary liquid layers, *Physics of Fluids A: Fluid Dynamics*, 4 (11), 2368–2381, 1992.

[114] N. Garnier and a. Chiffaudel, Two dimensional hydrothermal waves in an extended cylindrical vessel, *European Physical Journal B*, 19 (1), 87–95, 2001.

[115] N. Garnier, A. Chiffaudel, and F. Daviaud, Hydrothermal waves in a disk of fluid, in *Dynamics of Spatio-Temporal Cellular Structures, Springer Tracts in Modern Physics*, I. Mutabazi, J. E. Wesfreid, and E. Guyon, Eds. New York, NY: Springer, New York, NY, 2006, 147–161.

[116] G. Karapetsas, O. K. Matar, P. Valluri, and K. Sefiane, Convective rolls and hydrothermal waves in evaporating sessile drops, *Langmuir*, 28 (31), 11433–

11439, 2012.

[117] F. Carle, B. Sobac, and D. Brutin, Hydrothermal waves on ethanol droplets evaporating under terrestrial and reduced gravity levels, *Journal of Fluid Mechanics*, 712, 614–623, 2012.

[118] K. Sefiane, Y. Fukatani, Y. Takata, and J. Kim, Thermal patterns and hydrothermal waves (HTWs) in volatile drops, *Langmuir*, 29 (31), 9750–9760, 2013.

[119] K. Sefiane, A. Steinchen, and R. Moffat, On hydrothermal waves observed during evaporation of sessile droplets, *Colloids and Surfaces A: Physicochemical and Engineering Aspects*, 365 (1–3), 95–108, 2010.

[120] A. H. Persad, K. Sefiane, and C. a. Ward, Source of temperature and pressure pulsations during sessile droplet evaporation into multicomponent atmospheres, *Langmuir*, 29 (43), 13239–13250, 2013.

[121] P. J. Sáenz *et al.*, Dynamics and universal scaling law in geometrically-controlled sessile drop evaporation, *Nature Communications*, 8, 14783, 2017.

[122] F. Girard, M. Antoni, S. Faure, and A. Steinchen, Evaporation and Marangoni driven convection in small heated water droplets, *Langmuir*, 22 (26), 11085–11091, 2006.

[123] S. Semenov, V. M. Starov, R. G. Rubio, and M. G. Velarde, Instantaneous distribution of fluxes in the course of evaporation of sessile liquid droplets: Computer simulations, *Colloids and Surfaces A: Physicochemical and Engineering Aspects*, 372 (1–3), 127–134, 2010.

[124] W. D. Ristenpart, P. G. Kim, C. Domingues, J. Wan, and H. A. Stone, Influence of substrate conductivity on circulation reversal in evaporating drops, *Physical Review Letters*, 99 (23), 234502, 2007.

[125] B. D. MacDonald and C. A. Ward, Onset of Marangoni convection for evaporating sessile droplets, *Journal of Colloid and Interface Science*, 383 (1), 198–207, 2012.

[126] P. J. Sáenz, K. Sefiane, J. Kim, O. K. Matar, and P. Valluri, Evaporation of sessile drops: a three-dimensional approach, *Journal of Fluid Mechanics*, 772, 705–739, 2015.

[127] M. R. Barmi and C. D. Meinhart, Convective flows in evaporating sessile droplets, *The Journal of Physical Chemistry B*, 118 (9), 2414–2421, 2014.

[128] K. Sefiane and C. A. Ward, Recent advances on thermocapillary flows and interfacial conditions during the evaporation of liquids, *Advances in Colloid and Interface Science*, 134–135, 201–223, 2007.

[129] R. Savino, D. Paterna, and N. Favaloro, Buoyancy and Marangoni effects in an evaporating drop, *Journal of Thermophysics and Heat Transfer*, 16 (4), 562–574, 2002.

[130] C. a Ward and F. Duan, Turbulent transition of thermocapillary flow induced by water evaporation, *Physical Review E*, 69 (5), 056308, 2004.

[131] R. D. Deegan, O. Bakajin, T. F. Dupont, G. Huber, S. R. Nagel, and T. a. Witten, Contact line deposits in an evaporating drop, *Physical Review E*, 62 (1), 756–765, 2000.

[132] C.-G. Yang, Z.-R. Xu, and J.-H. Wang, Manipulation of droplets in microfluidic systems, *Trends in Analytical Chemistry*, 29 (2), 141–157, 2010.

[133] J. L. Garcia-Cordero and Z. H. Fan, Sessile droplets for chemical and biological assays, *Lab Chip*, 17 (13), 2150–2166, 2017.

[134] R. Blossey, Self-cleaning surfaces — Virtual realities, *Nature Materials*, 2 (5), 301–306, 2003.

[135] Y. Lu, S. Sathasivam, J. Song, C. R. Crick, C. J. Carmalt, and I. P. Parkin, Robust self-cleaning surfaces that function when exposed to either air or oil, *Science*, 347 (6226), 1132–1135, 2015.

[136] V. A. Ganesh, H. K. Raut, A. S. Nair, and S. Ramakrishna, A review on self-cleaning coatings, *Journal of Materials Chemistry*, 21 (41), 16304–16322, 2011.

[137] S. Nishimoto and B. Bhushan, Bioinspired self-cleaning surfaces with

superhydrophobicity, superoleophobicity, and superhydrophilicity, *RSC Advances*, 3 (3), 671–690, 2013.

[138] L. Cao, A. K. Jones, V. K. Sikka, J. Wu, and D. Gao, Anti-icing superhydrophobic coatings, *Langmuir*, 25 (21), 12444–12448, 2009.

[139] L. Mishchenko, B. Hatton, V. Bahadur, J. A. Taylor, T. Krupenkin, and J. Aizenberg, Design of ice-free nanostructured surfaces based on repulsion of impacting water droplets, *ACS Nano*, 4 (12), 7699–7707, 2010.

[140] P. Guo, Y. Zheng, M. Wen, C. Song, Y. Lin, and L. Jiang, Icephobic/anti-icing properties of micro/nanostructured surfaces, *Advanced Materials*, 24 (19), 2642–2648, 2012.

[141] J. Lv, Y. Song, L. Jiang, and J. Wang, Bio-inspired strategies for anti-icing, *ACS Nano*, 8 (4), 3152–3169, 2014.

[142] M. J. Kreder, J. Alvarenga, P. Kim, and J. Aizenberg, Design of anti-icing surfaces: smooth, textured or slippery?, *Nature Reviews Materials*, 1 (1), 15003, 2016.

[143] S. Daniel, M. K. Chaudhury, and J. C. Chen, Fast drop movements resulting from the phase change on a gradient surface, *Science*, 291 (5504), 633–636, 2001.

[144] N. Miljkovic and E. N. Wang, Condensation heat transfer on superhydrophobic surfaces, *MRS Bulletin*, 38 (5), 397–406, 2013.

[145] X. Qu *et al.*, Self-propelled sweeping removal of dropwise condensate, *Applied Physics Letters*, 106 (22), 221601, 2015.

[146] D. Orejon, O. Shardt, P. R. Waghmare, N. S. Kumar Gunda, Y. Takata, and S. K. Mitra, Droplet migration during condensation on chemically patterned micropillars, *RSC Advances*, 6 (43), 36698–36704, 2016.

[147] S. Lach, S. M. Yoon, and B. A. Grzybowski, Tactic, reactive, and functional droplets outside of equilibrium, *Chemical Society Reviews*, 45 (17), 4766–4796, 2016.

[148] M. M. Hanczyc, T. Toyota, T. Ikegami, N. Packard, and T. Sugawara, Fatty acid chemistry at the oil−water interface: Self-propelled oil droplets, *Journal of the American Chemical Society*, 129 (30), 9386–9391, 2007.

[149] C. Song, J. K. Moon, K. Lee, K. Kim, and H. K. Pak, Breathing, crawling, budding, and splitting of a liquid droplet under laser heating, *Soft Matter*, 10 (15), 2679–2684, 2014.

[150] L. Florea *et al.*, Photo-chemopropulsion — Light-stimulated movement of microdroplets, *Advanced Materials*, 26 (43), 7339–7345, 2014.

[151] W. Francis, C. Fay, L. Florea, and D. Diamond, Self-propelled chemotactic ionic liquid droplets, *Chemical Communications*, 51 (12), 2342–2344, 2015.

[152] S. C. Hernández *et al.*, Chemical gradients on graphene to drive droplet motion, *ACS Nano*, 7 (6), 4746–4755, 2013.

[153] Q. Liu and B. Xu, Actuating water droplets on graphene via surface wettability gradients, *Langmuir*, 31 (33), 9070–9075, 2015.

[154] S. K. Cho, H. Moon, and C.-J. Kim, Creating, transporting, cutting, and merging liquid droplets by electrowetting-based actuation for digital microfluidic circuits, *Journal of Microelectromechanical Systems*, 12 (1), 70–80, 2003.

[155] C. Song, K. Kim, K. Lee, and H. K. Pak, Thermochemical control of oil droplet motion on a solid substrate, *Applied Physics Letters*, 93 (8), 084102, 2008.

[156] S. Mettu and M. K. Chaudhury, Motion of drops on a surface induced by thermal gradient and vibration, *Langmuir*, 24 (19), 10833–10837, 2008.

[157] M. G. Pollack, A. D. Shenderov, and R. B. Fair, Electrowetting-based actuation of droplets for integrated microfluidics, *Lab on a Chip*, 2 (2), 96–101, 2002.

[158] F. Mugele and J.-C. Baret, Electrowetting: from basics to applications, *Journal of Physics: Condensed Matter*, 17 (28), 705–774, 2005.

[159] A. Shastry, M. J. Case, and K. F. Böhringer, Directing droplets using microstructured surfaces, *Langmuir*, 22 (14), 6161–6167, 2006.

[160] M. Reyssat, F. Pardo, and D. Quéré, Drops onto gradients of texture, *Europhysics Letters*, 87 (3), 36003, 2009.

[161] N. Moradi, F. Varnik, and I. Steinbach, Roughness-gradient–induced spontaneous motion of droplets on hydrophobic surfaces: A lattice Boltzmann study, *Europhysics Letters*, 89 (2), 26006, 2010.

[162] Y. Kita, A. Askounis, M. Kohno, Y. Takata, J. Kim, and K. Sefiane, Induction of Marangoni convection in pure water drops, *Applied Physics Letters*, 109 (17), 171602, 2016.

[163] A. Askounis, Y. Kita, M. Kohno, Y. Takata, V. Koutsos, and K. Sefiane, Influence of local heating on marangoni flows and evaporation kinetics of pure water drops, *Langmuir*, 33 (23), 5666–5674, 2017.

[164] F. Girard, M. Antoni, S. Faure, and A. Steinchen, Influence of heating temperature and relative humidity in the evaporation of pinned droplets, *Colloids and Surfaces A: Physicochemical and Engineering Aspects*, 323 (1–3), 36–49, 2008.

[165] P. Colinet, J. C. Legros, and M. G. Velarde, *Nonlinear dynamics of surface-tension-driven instabilities*. Berlin: Wiley-VCH, 2001.

[166] S. Chandrasekhar, *Hydrodynamic and hydromagnetic stability*. Dover Publications, 1981.

[167] Japan Society of Mechanical Engineers, *1999 JSME steam tables*, 5th ed. Tokyo: Maruzen, 1999.

[168] R. Bhardwaj, X. Fang, P. Somasundaran, and D. Attinger, Self-assembly of colloidal particles from evaporating droplets: Role of DLVO interactions and proposition of a phase diagram, *Langmuir*, 26 (11), 7833–7842, 2010.

[169] E. Dietrich, E. S. Kooij, X. Zhang, H. J. W. Zandvliet, and D. Lohse, Stick-jump mode in surface droplet dissolution, *Langmuir*, 31 (16), 4696–4703,

2015.

[170] B. E. Poling, J. M. Prausnitz, and J. P. O'Connell, *The properties of gases and liquids*. McGraw-Hill, 2001.

[171] I. Lagzi, S. Soh, P. J. Wesson, K. P. Browne, and B. A. Grzybowski, Maze solving by chemotactic droplets, *Journal of the American Chemical Society*, 132 (4), 1198–1199, 2010.

[172] Y. Zhao, F. Liu, and C.-H. Chen, Thermocapillary actuation of binary drops on solid surfaces, *Applied Physics Letters*, 99 (10), 104101, 2011.

[173] M.-C. Liu *et al.*, Two dimensional thermoelectric platforms for thermocapillary droplet actuation, *RSC Advances*, 2 (4), 1639–1642, 2012.

[174] G. Karapetsas, K. C. Sahu, K. Sefiane, and O. K. Matar, Thermocapillary-driven motion of a sessile drop: Effect of non-monotonic dependence of surface tension on temperature, *Langmuir*, 30 (15), 4310–4321, 2014.

[175] R. E. Johnson and R. H. Dettre, Contact angle hysteresis I. Study of an ideolized rough surface, in *Contact Angle, Wettability, and Adhesion*, F. M. Fowkes, Ed. WASHINGTON, D.C.: American Chemical Society, 1964, 112–135.

[176] R. E. Johnson and R. H. Dettre, Contact angle hysteresis. III. Study of an idealized heterogeneous surface, *The Journal of Physical Chemistry*, 68 (7), 1744–1750, 1964.

[177] R. J. Good, Contact angle, wetting, and adhesion: a critical review, *Journal of Adhesion Science and Technology*, 6 (12), 1269–1302, 1992.

[178] L. Gao and T. J. McCarthy, Wetting 101°, *Langmuir*, 25 (24), 14105–14115, 2009.

[179] H. B. Eral, D. J. C. M. 't Mannetje, and J. M. Oh, Contact angle hysteresis: a review of fundamentals and applications, *Colloid and Polymer Science*, 291 (2), 247–260, 2013.

[180] M. Reyssat and D. Quéré, Contact angle hysteresis generated by strong

dilute defects, *The Journal of Physical Chemistry B*, 113 (12), 3906–3909, 2009.

[181] W. Xu and C.-H. Choi, From sticky to slippery droplets: Dynamics of contact line depinning on superhydrophobic surfaces, *Physical Review Letters*, 109 (2), 024504, 2012.

[182] R. Raj, R. Enright, Y. Zhu, S. Adera, and E. N. Wang, Unified model for contact angle hysteresis on heterogeneous and superhydrophobic surfaces, *Langmuir*, 28 (45), 15777–15788, 2012.

[183] K. Sefiane, Effect of nonionic surfactant on wetting behavior of an evaporating drop under a reduced pressure environment, *Journal of Colloid and Interface Science*, 272 (2), 411–419, 2004.

[184] J. Wu, J. Xia, W. Lei, and B. Wang, Advanced understanding of stickiness on superhydrophobic surfaces, *Scientific Reports*, 3 (1), 3268, 2013.

[185] M. E. R. Shanahan, Simple theory of "stick-slip" wetting hysteresis, *Langmuir*, 11 (3), 1041–1043, 1995.

[186] N. A. Patankar, On the modeling of hydrophobic contact angles on rough surfaces, *Langmuir*, 19 (4), 1249–1253, 2003.

[187] L. Gao and T. J. McCarthy, Contact angle hysteresis explained, *Langmuir*, 22 (14), 6234–6237, 2006.

[188] S. Chandrasekhar, The oscillations of a viscous liquid globe, *Proceedings of the London Mathematical Society*, s3-9 (1), 141–149, 1959.

[189] T.-V. Nguyen, M.-D. Nguyen, H. Takahashi, K. Matsumoto, and I. Shimoyama, Viscosity measurement based on the tapping-induced free vibration of sessile droplets using MEMS-based piezoresistive cantilevers, *Lab on a Chip*, 15 (18), 3670–3676, 2015.

[190] C. W. Extrand and S. I. Moon, Contact angles of liquid drops on super hydrophobic surfaces: Understanding the role of flattening of drops by gravity, *Langmuir*, 26 (22), 17090–17099, 2010.

[191] J. Park, J. Park, H. Lim, and H.-Y. Kim, Shape of a large drop on a rough

hydrophobic surface, *Physics of Fluids*, 25 (2), 022102, 2013.

[192] K. A. Brakke, The surface evolver, *Experimental Mathematics*, 1 (2), 141–165, 1992.

[193] M. J. Santos and J. A. White, Theory and simulation of angular hysteresis on planar surfaces, *Langmuir*, 27 (24), 14868–14875, 2011.

[194] Y. Kita, A. Askounis, Y. Takata, J. R. E. Christy, K. Sefiane, and J. Kim, Thermal/flow visualisation of flows in water drops induced by a microheater, in *Proceedings of the 15th UK Heat Transfer Conference (UKHTC2017)*, 2017, (September), 4–5.

[195] A. Lee, M.-W. Moon, H. Lim, W.-D. Kim, and H.-Y. Kim, Water harvest via dewing, *Langmuir*, 28 (27), 10183–10191, 2012.

[196] H. Kim *et al.*, Adsorption-based atmospheric water harvesting device for arid climates, *Nature Communications*, 9 (1), 1191, 2018.